ASTEROID CHARACTERIZATION THROUGH SERENDIPITOUS DETECTION BY THE MID-INFRARED INSTRUMENT ON THE JAMES WEBB SPACE TELESCOPE

Master Thesis

Lenka Husárová

Faculty of Aerospace Engineering
Delft University of Technology

October 26, 2018

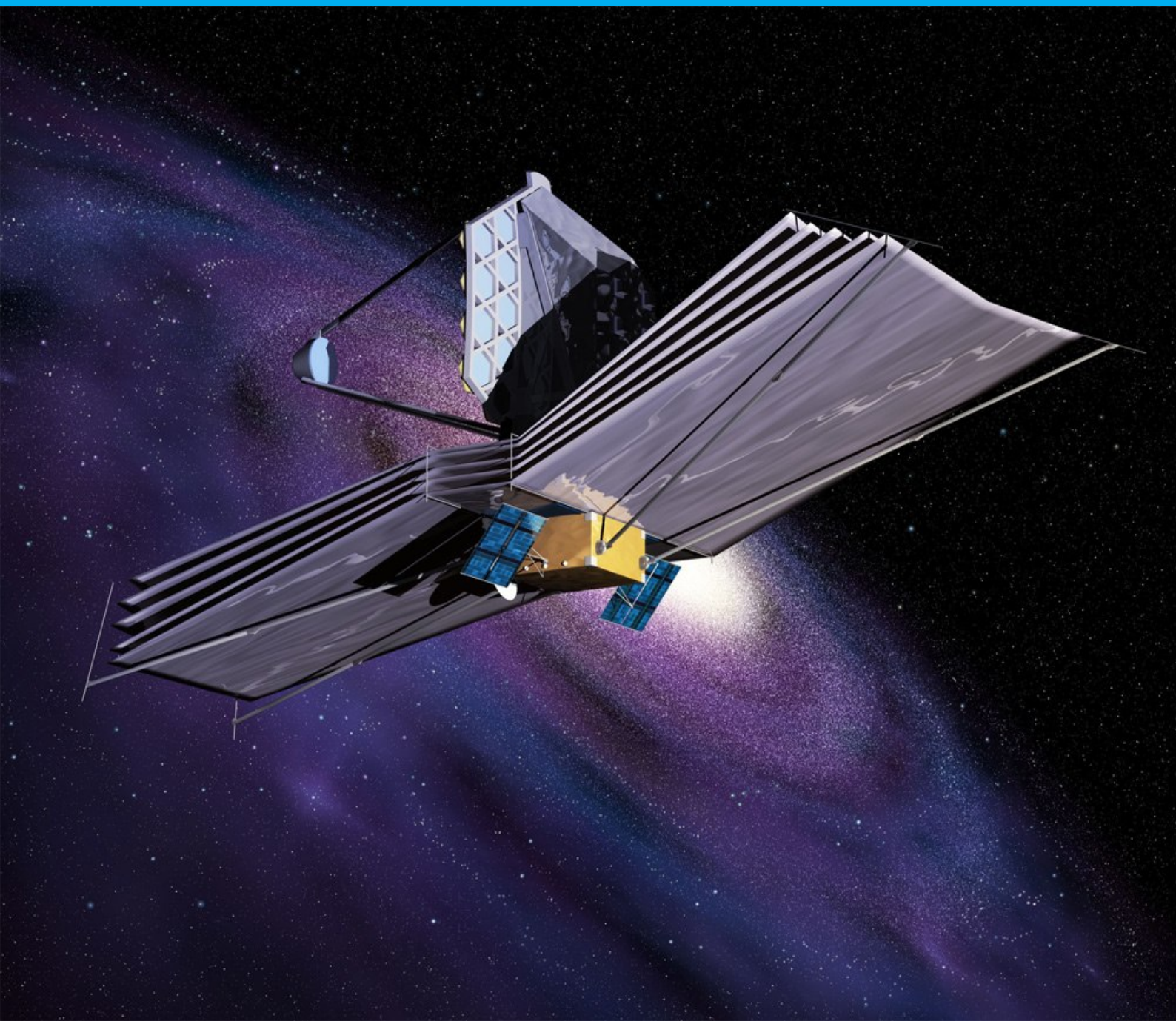

Picture Credit: ESA [1]

Master thesis report

Asteroid characterization through serendipitous detection by the Mid-Infrared Instrument on the James Webb Space Telescope

by

Lenka Husárová 4223527

to obtain the degree of Master of Science in Aerospace Engineering
at the Delft University of Technology,
to be defended publicly on Monday November 19, 2018 at 14:00.

Project duration:	March 15, 2018 – October 26, 2018	
Thesis committee:	Prof. dr. B. R. Brandl,	TU Delft, supervisor
	Dr. S. M. Cazaux,	TU Delft
	Dr. A. Menicucci,	TU Delft
	Dr. M. Mueller,	SRON

An electronic version of this thesis is available at `http://repository.tudelft.nl/`.

TU Delft

Abstract

The interest in asteroids is increasing, due to their promising clues on the origin of the Solar System, e.g. their albedos and sizes can provide insight into the protosolar nebula. The new scientific mission scheduled to launch in 2021, the James Webb Space Telescope (JWST), provides an opportunity for observation of asteroids. In this thesis, the feasibility of using the Mid-Infrared Instrument's (MIRI) imager on the JWST for serendipitous characterization of asteroids is evaluated. The imager and the medium resolution spectrometer (MRS) run simultaneously. When MRS is running, imager data could be used for detection of asteroids in infrared, where the error in size is only 10%, comparing to 100% in optical, because the thermal radiation is independent of the albedo. Combining the optical and infrared, the albedo can be determined. This prospective use is researched by simulating the sensitivity of the imager. A tool, created during this thesis, simulates realistic cases using proposal (GTO 1282) and determines the known asteroids in the field of view (FOV) of the imager. MIRISim, created by the MIRI European Consortium, simulates their signatures. The results show a 4.1% chance of an asteroid appearing in the FOV and a 96.9% detection of such an asteroid. In a typical MIRI observation, exposure time of 488.4 s, with preferred filter F1280W, the imager can detect asteroids bigger than 250 m in diameter and closer than 3 AU. This could lead to a detection of 733 256 yet undetected asteroids and 183 314 currently known asteroids in the lifetime of JWST.

Preface

This thesis report is the final deliverable of my master in Space flight, track Exploration, at the Faculty of Aerospace Engineering at the Delft University of Technology. The report shows the results of this thesis, the research into the potential use of James Webb Telescope's Mid-Infrared Instrument for serendipitous observation and characterization of asteroids.

I would like to express my gratitude to all that helped me during this challenging time.
First, I would like to thank my thesis supervisor, Professor B. Brandl. His constant advice and guidance was very much appreciated. I am grateful to him for helping me with my time management skills and overcoming my indecision. I might not have been done with the thesis otherwise.

I am also very thankful for all the valuable advice from Dr. M. Mueller. His knowledge of asteroids and his willingness to provide feedback or aid with any coding problem was a great help.

I would also like to thank the committee members Dr. S. Cazaux and Dr. A. Menicucci for taking time in their busy schedules to read my thesis and being available to help if any problem arises.

Words of thanks also go to my family and friends for their support. I would like to specifically thank my parents and grandparents for feeding me and always having a positive word for me, and to my siblings for their astonishment every time they remembered what I study. I also have to mention few others: Veronika O., for always bringing the hard truths, but just because she cares, Ivana Š., Viki T. and Zuzka F., for being my gym and food buddies, Akhil G., for always being there, Daniela H. and Radu F., for making sure I always have a place to rest my head, Hendrik V., just for being nice, Tomas M., for being a great friend, Ricard C. R. for showing me how it should not be done, Danica Z. and Michaela B., for all the gossips, Broňa K., for always bringing a breath of fresh air, Kateryna F., for making me feel welcome and not alone and Martin R. for the never-ending roller-coaster.

Lenka Husárová
Bratislava, October 2018

Summary

The small, rocky bodies, flying in space are called asteroids. They orbit around the Sun the same as planets. Some of them were even originally thought to be planets or stars. However, after they appeared to be too small for a planet or to be moving too much for a star, astronomers realized there is a new group, i.e. asteroids. Despite their smaller size (smaller than planets), they have been found to be full of interesting information. They are remnants from the beginnings of the Solar System and they could help with learning about its evolution, the protosolar nebula and the formation of planets. In the past, asteroids also collided with the Earth, and therefore they could provide more knowledge about the Earth, its shape, biosphere and maybe even life. However, asteroids could also be dangerous. Some of them orbit close to the Earth and some could even fall into the Earth's atmosphere. Most of the asteroids are small enough, that they burn up in the atmosphere, or cause only minor damage. However, there is a small possibility [2] that a bigger asteroid could hit the Earth and bring destruction. If there was more information known about them, a better probability estimation of such event happening could be made. With the new data, such events could also be prevented, for example by mining the asteroid and using the minerals for industrial purposes. Unfortunately, the current knowledge for most of the asteroids is very limited. All the asteroid knowledge has been determined from observations. Most of the asteroids have been detected and observed using optical observations. This was the most common way of observing the universe, due to the available knowledge and technology developed for electromagnetic spectrum. However, from optical observations, only the position of the asteroid can be determined accurately. The size or the composition are determined only with big errors ($> 100\%$). This is because the brightness of an asteroid in the optical spectrum is dependant on the size and surface composition, albedo, of the asteroid. Neither of these values is known and therefore only a value expressing a combination of both of them can be determined. To be able to find the size of asteroids, infrared observations could be used. In the infrared, the brightness is mostly the thermal brightness and that is dependant on the distances between the Sun, the asteroid and the instrument, and the temperature of the asteroid, which is dependant on its size. Combining this calculated size, with the data from optical, the albedo can be determined as well and this albedo can give us information about the surface composition of the asteroid. Most of the diameters currently known are estimated from infrared observations, such as the IRAS [3] and WISE [4] surveys of asteroids.

A new telescope, James Webb Space Telescope, will be launched to space in 2021. This telescope has four innovative instruments on board, which are able to see in the infrared wavelength. One of these instruments is the Mid-Infrared Instrument, MIRI for short, with a special setting, where its medium resolution spectrometer (MRS) and imager run simultaneously. This could be used for observation of asteroids, such that when a user is observing with the MRS, the imager is obtaining data of the sky as well. However, the user might not be interested in the data from the imager. Nevertheless, as asteroids orbit around the Sun, they might appear in the field of view of the imager and get detected. This is the focus of this thesis, to determine whether it would be feasible to use the imager for serendipitous observation of asteroids. To determine whether the imager is sensitive enough to detect the asteroids passing in its field of view a simulation tool is developed. This tool consists of multiple steps. First, the astronomers proposal tool is used to simulate realistic cases for the imager, with the help of GTO 1282 proposal. These are actual proposals from scientists for the MRS to look at specific directions in the sky at specific times. Second, a database with these proposed times and pointings in the sky is created. Third, this database is used in the Serendipitous asteroid detection tool, more details can be seen in Appendix A [5]. This tool will determine the asteroids in the field of view of the imager at the specified times and direction as well as how much they move during the observation time of the imager. This is done with the help of the Horizons database of asteroids [6] as well as the Asteroid & Comet Field-of-View Search Request [7]. This tool also uses a Near Earth Thermal model (NEATM) to determine the brightness received by the instrument according to its estimated characteristics. Fourth, the temperature of the asteroid is determined. Fifth, data about the asteroids in the field of view, such as their temperature, position and brightness, are used in the MIRISim. MIRISim is a simulator of the MIRI instrument, still under development, created by the MIRI European Consortium, with significant

contributors from other scientific institutes [8][9]. The outputs from this simulator are then evaluated and signal to noise ratio for each asteroid is calculated to determine the visibility of asteroids by the imager.

It has been concluded from the simulation, that the probability of a currently known asteroid being in a field of view of the imager is not so big, only 4.1%. However, once the asteroid is in the field of view, it will be detected 96.9% of the time. For a typical MIRI mission, exposure time of 488.4 s, the filter of F1280W, and the distances between the Sun, the asteroid and the instrument smaller than 3 AU, only asteroids smaller than 250 m in diameter are too dark to be detected. Over the course of the 5-year mission, 183 314 of the known asteroids can be detected and their sizes can be measured, assuming the imager is working 25% of the science time. Overall, the signal to noise ratio for most of the asteroids is higher than 150, which is exceptional detectability and therefore it stands to reason that also many yet undetected asteroids could be detected by the instrument and help with estimating the sizes and albedos of currently known as well as yet undetected asteroids. The "free" use of imager, simultaneously with the MRS, could bring knowledge of more than 916 570 asteroids bigger than 300 m in diameter. This would lead to a potential detection of 733 256 yet unknown asteroids.

Contents

List of Tables

List of Figures

List of Abbreviations

The following is list of abbreviations used in the text in alphabetical order.

Abbreviation	Meaning	Abbreviation	Meaning
APT	Astronomer's Proposal Tool	**MIRI**	Mid-infrared Instrument
arcmin	Arcminute	**MIRIM**	Mid-infrared Instrument's Imager
arcsec	Arcsecond		
DEC	Declination	**MIRISim**	Mid-infrared Instrument Simulator
deg	Degree		
Dr.	Doctor	**MRS**	Medium resolution spectrometer
e.g.	For example	**NASA**	National Aeronautics and Space Administration
ESA	European Space Agency		
ETC	Exposure Time Calculator	**NIRCam**	Near-Infrared Camera
GO	General Observer	**NIRSpec**	Near-Infrared Spectrograph
GTO	Guaranteed Time Observation	**NIRISS**	Near InfraRed Imager and Slitless Spectrograph
FGS	Fine Guidance Sensor		
FITS	Flexible Image Transport System	**NEATM**	Near Earth Asteroid Thermal Model
FOV	Field of view	**NEO**	Near Earth Object
FWHM	Full width at half maximum	**Prof.**	Professor
F0000W	Imager filter starting at 00.00 wavelength	**RA**	Right ascension
		SN	Signal to Noise ratio
Hz	Hertz	**SMASS**	Small Main-Belt Asteroid Spectroscopic Survey
i.e.	That is		
IRAS	Infrared Astronomical Satellite	**STM**	Standard Thermal Model
JPL	Jet Propulsion Laboratory	**STScI**	Space Telescope Science Institute
JWST	James Webb Space Telescope		
Jy	Jansky unit for spectral flux density	**TNT**	Trinitrotoluene
		TU Delft	Delft University of Technology
mJy	milli Jansky	**UTC**	Coordinated Universal Time
KBO	Kuiper Belt Objects	**WISE**	Wide-field Infrared Survey Explorer
kg	Kilogram		
kg/m^2	Kilogram per meter squared	**w.r.t**	With respect to
km	Kilometer	**μm**	Micro meter
km/s^2	Kilometer per second squared	**μm/λ^2**	Micro meter per cubic millimeter
L2	2nd Lagrange point	**μJy**	Micro Jansky
LRS	Low-resolution spectroscopy		

List of Symbols

Symbol	Meaning	Unit
a	Semi-major axis	[AU]
A	Bond albedo	[-]
AU	Astronomical unit	[-]
$\mathbf{B_v}$	Spectral radiance of the body	[W/m^2srnmm]
c	Speed of light	[km/s]
°C	Degrees Celsius	[-]
D	Diameter	[km]
d	Telescope-asteroid distance	[AU]
G	Slope parameter	[-]
H	Absolute magnitude	[-]
h	Planck's constant	[Js]
N	Number	[-]
$\mathbf{n_{group}}$	Number of frames	[-]
$\mathbf{n_{int}}$	Number of integrations during an exposure	[-]
K	Kelvin	[-]
$\mathbf{k_B}$	Boltzmann constant	[J/K]
pv	Geometric albedo	[-]
q	Phase integral	[deg]
r	Radial distance	[km]
$\mathbf{r_{AU}}$	Asteroid's heliocentric distance	[AU]
$\mathbf{S_0}$	Solar constant	[W/m^2]
s	Second	[-]
sr	Steradian	[-]
T	Temperature	[K]
$\mathbf{t_1}$	Time between frames	[s]
$\mathbf{t_{int}}$	Integration time	[s]
$\mathbf{t_{exp}}$	Exposure time	[s]
V	Orbital velocity	[km/s]
v	Frequency	[Hz]
V1	Axis in JWST coordinate system pointing forward from the primary mirror	[arcmin]
V2	Axis in JWST coordinate system pointing away from the spacecraft bus	[arcmin]
V1	Axis in JWST coordinate system pointing in the anti space direction	[arcmin]
W	Watt	[-]
$\mathbf{\Delta\lambda}$	Change in wavelength	[-]
$\boldsymbol{\epsilon}$	Emissivity	[-]
$\boldsymbol{\eta}$	Beaming parameter	[-]
$\boldsymbol{\theta_i}$	Solar incidence angle	[°]
$\boldsymbol{\lambda}$	Wavelength	[μm]
$\boldsymbol{\mu}$	Standard gravitational parameter	[km^3s^{-2}]
$\boldsymbol{\sigma}$	Standard deviation	[-]
$\sim$	Approximately	[-]
$^\circ$	Degree	[-]
$'$	Arcminute	[-]
$''$	Arcsecond	[-]

1. Introduction

"On 15 February 2013, a large fireball was reported over Chelyabinsk, Russia" [25]. These reports have circulated over the whole world in the spring of 2013. An asteroid approached the Earth and exploded around 15-20 km above the ground. The force of this explosion was equivalent to almost 500 kilotons of TNT [25], which could be compared to approximately 30 times the energy released by the atomic bomb dropped on Hiroshima. Luckily, the damage was minor. Nevertheless, it reminded everyone of the possible danger from the asteroids. It has not been so long ago when the Earth was populated by dinosaurs, and it is argued that an asteroid hit the Earth and aided towards their extinction. Thankfully, such events happen rarely, and mostly only smaller asteroids infiltrate the Earth's atmosphere [26]. It has been reasoned that the Jupiter shields the Earth from many bigger asteroids with its higher gravitational pull and that the Moon has saved the humanity from many unpleasant encounters with asteroids as well. However, this does not mean that asteroids are only the bringers of destruction. Asteroids also carry a lot of valuable information about the universe and mainly the Solar System. There are over 790 150 known at the moment [6] and each day more and more are found. Around 18 900 of them are Near-Earth Objects (NEOs), orbiting in close proximity to the Earth, less than 0.3 AU. Observing asteroids and detecting new ones can help with understanding the origin and the evolution of the Solar System. Asteroids are planetesimals, bodies that have been part of the forming of the planets and they have significantly altered the Earth's shape and biosphere by their yearly collisions with this blue planet [27]. Their distribution in space can help with simulating the formation of planets and reconstruction of the Solar System evolution. Additionally, they are a source of volatiles and other minerals, which could be exploited for the exploration and colonization of the Solar System in the future. They could also become an economic commodity, a place for in-situ mining of the asteroid's materials.

Optical observations have been the most used way for detection and observation of asteroids in the past, as the most common and available technology. They can lead to accurate position determination, but in the estimation of the diameter of asteroids they have an order of magnitude uncertainty. Optical spectrum can detect the reflected brightness of the asteroid, and this is dependant on the size, the distance between the asteroid, Sun and the observer and the albedo, where albedo is the value representing the amount of solar radiation reflected by the asteroid depending on the composition of the surface. The big error in the size estimation is due to the inaccuracy in the albedo values of different asteroids [4], where for most asteroids the albedo value is not known at all. If the diameter is known, the albedo can be estimated from the optical observations. Diameters and albedos are important values for researching the history of the universe, as knowing these values for different asteroid families could be used to study their age according to their orbital evolution. The size-frequency distribution of the asteroids, and their composition, estimated from albedo values, can put constraints on the collisional and orbital evolution of the Solar System. Therefore, a large survey estimation of albedo and size would be advantageous for determining the distribution and migration of planets and other bodies throughout the history of the Solar System. This can be done in the infrared wavelength with a much lower uncertainty (less than 10%) [4], as the brightness in the infrared is mostly the thermal radiation, which is not dependant on albedo. The thermal radiation is dependant on the size of the asteroid, the distance between the asteroid and the instrument, and the temperature, which depends on the distance between the Sun and the asteroid. Therefore, the size of an asteroid can be measured from infrared observations, as the distances between the objects can be calculated from the observation. Then, combining with the data from optical, the albedo can be determined as well. Most of the diameters known are actually estimated from infrared observations, IRAS [3] and WISE [4] surveys of asteroids.

In 2021, a new telescope, James Webb Space Telescope, with four scientific instruments will be launched into space. One of these instruments is the Mid-Infrared Instrument (MIRI), which can observe at infrared wavelengths and its medium resolution spectrometer (MRS) and imager run simultaneously. This means that when the MRS is being used for observations, the imager records data as well. However, this data might not be of interest to the user of MRS and therefore could be free to be used for other science. Why not use this opportunity to learn more about asteroids?

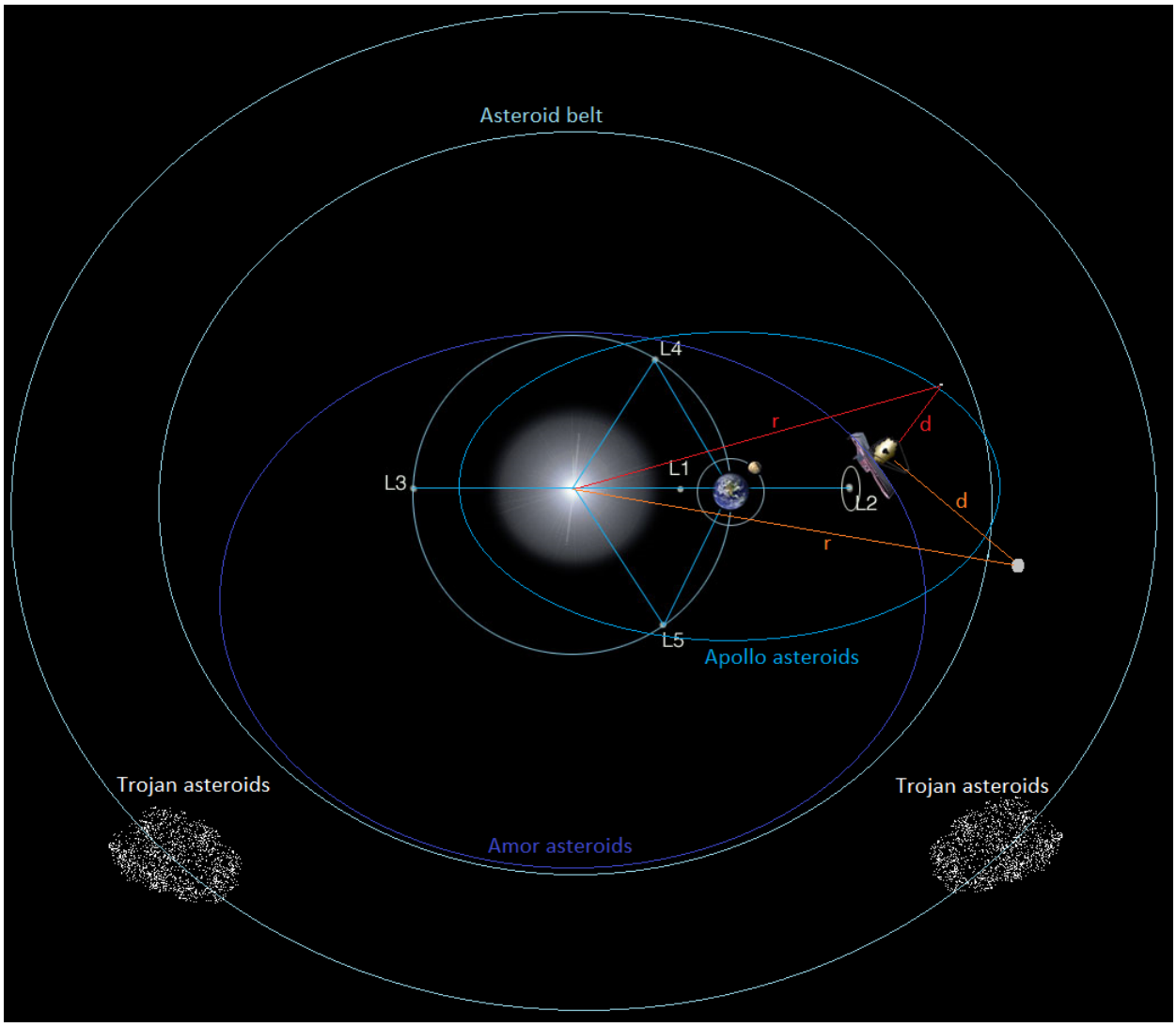

Figure 1.1: Location of the JWST w.r.t the Sun and the orbit of the Earth. Different asteroid orbits are shown as well, e.g. the Main asteroid belt, Trojan asteroids and the Apollo and Amor asteroid group. Two asteroids are depicted and the Sun-asteroid (r) and instrument-asteroid (d) distances are shown as well. These distances change depending on where in the orbit the JWST is as well as where the asteroids are. Picture credit: STScI (JWST).

The data from imager could be used to detect and observe asteroids and measure their sizes from their emitted brightness as can be seen in Figure 1.1. Figure 1.1 shows a geometric view of orbits of the Earth, JWST and different asteroid groups. Depending on where the JWST is pointing, and where the JWST is in its orbit, the asteroids might be closer or further, as shown by the two depicted asteroids and their distances to the Sun (r) and the instrument (d). This thesis will determine the possibility of using this instrument for detection and observation of asteroids at infrared wavelengths, by simulating the sensitivity of the Mid-Infrared Instrument's imager and evaluating the resulting images for the visibility of the asteroids. The research is done using the MIRISim, MIRI's simulator created by MIRI European Consortium and a simulation tool developed during this thesis. This tool basically determines the currently known asteroids, in the field of view of MIRI at a specified time, and how much they move through the field of view during the observation time. This depends on how fast the asteroid is orbiting, the closer an asteroid is to the Sun, the faster it moves, from which the apparent motion can be determined, which is how much the asteroid moves w.r.t. the instrument. Typical values are less than 0.01 arc/s. Then with some of their estimated or assumed physical characteristics, their signature in the imager is simulated with MIRISim. The output from MIRISim is analysed and the signal to noise ratio

for each of the asteroids is calculated. This quantifies how 'visible' the asteroids are in the data from the MIRI's imager. With the help of a proposal (GTO 1282) [13] to make the simulations more realistic, this will ultimately answer the main thesis question: "Is asteroid characterization through serendipitous detection by the Mid-Infrared Instrument's imager on board of James Webb Space Telescope feasible?"

The structure of this report is as follows. In Chapter 2, the asteroids and their characteristics are discussed and their orbits and locations are presented. The advantages of detection and observation of asteroids in the optical and infrared spectrum are compared in Chapter 3. James Webb Space Telescope and its specifications and scientific instruments are presented in Chapter 4, where the Mid-Infrared Instrument's and its imager's capabilities are closely assessed. Chapter 5 explains the simulation tool created to determine whether the Mid-Infrared Instrument's imager's infrared sensitivity is suitable to bring progress in learning more about asteroids. The last Chapter 6, shows and discusses the results from the simulation tool and determines the answer to the thesis question, whether asteroid characterization through serendipitous detection by the Mid-Infrared Instrument's imager on the James Webb Space Telescope is feasible.

2. Current Estimates of Asteroid Properties

Asteroids are inactive, relatively small, rocky bodies flying in space. Many asteroids fly close by the Earth every day and some even collide or burn up in the atmosphere. Asteroid means "star-like" in the ancient Greek. This name was coined by astronomer William Herschel in 1802, a year after the first discovered asteroid Ceres. Ceres was first thought to be a star, however, after observing it for a while, it was found to be moving much more than a distant star would [28].

Asteroids are planetesimals, remnants from the beginning of our solar system and they could provide key information about the Solar system's origins. Their distribution in space, discussed more in Section 2.1, could provide information about temperatures, pressures and chemistry of the solar nebula [27]. As of now, more than 790 150 asteroids have been detected and registered, together with their positional uncertainty, in the NASA's Horizons asteroid database [6]. New data about asteroids are received daily and with each new information, the estimation of their properties can improve. The currently estimated properties are given in Section 2.2. However, for most of the asteroids, only their position is properly known. Therefore, more information about their composition, determined from albedo, and the size would be very valuable.

2.1 Orbit Location of Asteroids

According to the similarity of orbits of asteroids, they can be divided into groups. There are many groups and in this report, only some of the biggest ones will be mentioned.

- Most asteroids are in a group orbiting in relatively stable regions between the orbits of Mars and Jupiter (2-3.5 AU from the Sun), called **the Main asteroid belt**, as can be seen in Figure 2.1.
- Orbiting exterior to Neptune's orbit is **the Kuiper belt group** (30-50 AU from the Sun).
- **The Oort cloud**, which is a theoretical cloud of icy planetesimals, orbits between 50 000-200 000 AU from the Sun.
- Near the triangular Lagrangian points of Jupiter is **the Trojan asteroids group**, also in Figure 2.1.
- Those asteroids that come close to the Earth are known as **Near Earth objects (NEOs)**, with orbit location partially between 0.983 and 1.3 AU.
- Asteroids that orbit with the giant planets in unstable orbits, between Jupiter and Neptune, are called **Centaurs**.

Trojans, Centaurs and trans-Neptunian objects are mentioned and considered asteroids in this report, however, it could be argued that they are "minor planets", as many of them are much bigger (more than 2000 km in diameter) than the biggest main belt asteroid, or comets. However, the distinction between comet and asteroid is becoming difficult to characterize. It is also important to mention that the main focus of the report will be the asteroids orbiting closer to the Earth, such as the Main belt or NEOs, as these asteroids are more likely to be observed by the James Webb Space Telescope, as discussed in Chapter 4.

Due to the interaction of asteroids with planets or other asteroids, some asteroids have highly elongated orbits, which can pass close by other bodies. It has been also observed that all (known) asteroids orbit the Sun in the same direction as the planets. Most asteroids orbit near the ecliptic plane, with the mean inclination to the ecliptic of 15° [27].

In Figure 2.2, the orbital distribution of 69 500 known asteroids with respect to the mean Sun distance is shown. These specific regions can be explained by orbital resonances between asteroids and Jupiter [27]. Orbital resonance is a gravitational phenomenon where two bodies are orbiting the same body. They have regular, periodic gravitational influence on each other, mostly because their orbital periods

are related by a ratio of small integers. Similarly, as the main asteroid belt influenced due to resonances with Jupiter, the Kuiper belt was formed by the influence of Neptune.

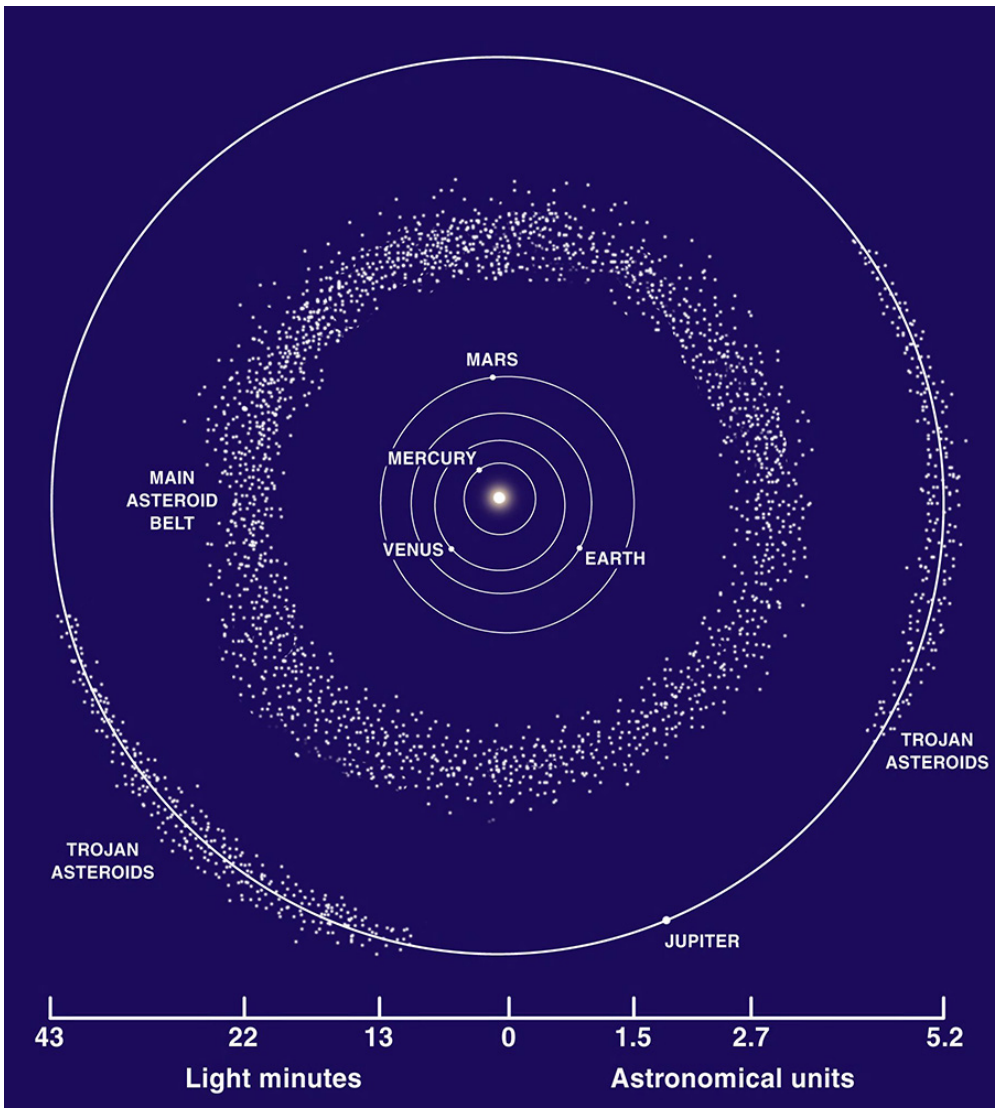

Figure 2.1: Location of the main asteroid belt in relation to other objects in our solar system [14]. More asteroids are located further than shown here, such as the Kuiper belt group (30-50 AU) or the Oort cloud (50 000-200 000 AU). However, it is expected that mostly the Main asteroid belt and NEOs will be targeted in this thesis.

Their resonances with Jupiter are given in Figure 2.2 as well, such as 3:1, which means that Jupiter makes one orbit around the Sun, while the asteroids make 3. It can be seen that at some resonances, gaps in orange, Jupiter has cleared out the asteroids. It forced them out of their orbit, to either crash into another body or leave the solar system. The asteroids with unusual orbits are also a result of Jupiter's gravity, they are being pushed out of their orbit into a new one. On the other hand, concentrations in yellow represent the favourable positions for asteroids. It should also be mentioned, that the values in Figure 2.2 might not be the real distribution, as the nearer and brighter asteroids are easier to discover [29].

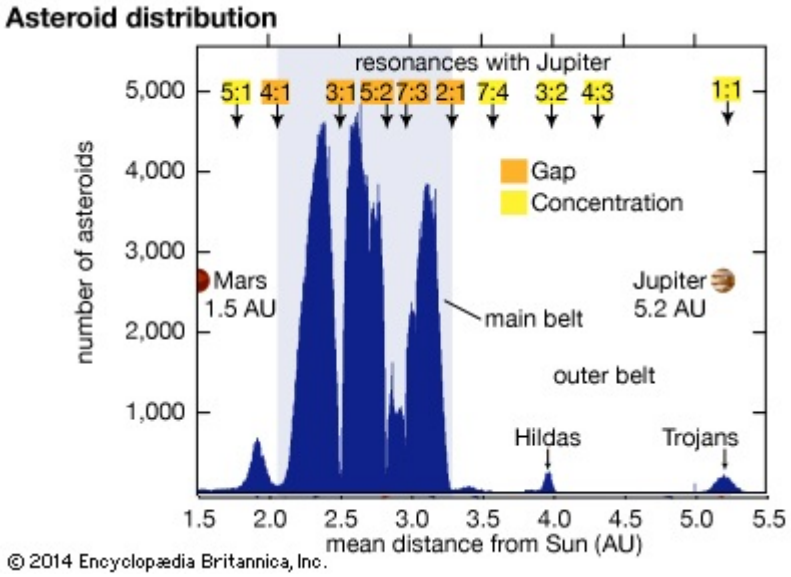

Figure 2.2: Asteroid distribution according to the number of asteroids w.r.t. the mean distance to the Sun until 5.5 AU, as most of the asteroids known, are in this region [11]. The concentrations in yellow represent the favourable orbits for asteroids. However, there is a possible sample bias in detecting the closer orbiting and bigger asteroids.

2.2 Asteroid Characteristics

Asteroids with similar physical characteristics can be grouped in asteroid families [27]. The families are based on similar orbital elements, such as eccentricity, semi-major axis or orbital inclination. Due to the similarities of asteroids in these families, the asteroids could be remnants of past asteroid collisions or even fragments of a single asteroid.

Depending on asteroid characteristics, it can be easier or harder to detect them. Asteroids which are closer, brighter and bigger are easier to detect and that is why most known asteroids are Near-Earth objects or from the Main asteroid belt. Unfortunately, their characteristics are not well known and many of the estimations might not be correct. For example, for most of the Kuiper Belt Objects (KBOs) the only physical property known is the object's visible colour [27], nevertheless, for some of them, the size has been measured as well. The Horizons asteroid database [6] provides the uncertainty in the position of the asteroids as well as some of their estimated characteristics. Nonetheless, to get the latest data, scientific papers, should be reviewed.

2.2.1 Size and Shape

The detected asteroids have a measured diameter between a few meters to a few hundred kilometres, however, it is expected that smaller asteroids exist, they are just too small to be detected yet. The bigger asteroids are usually easier to detect, however, it also depends on the distance or reflectance of their surface. In Figure 2.3, the size of asteroids is plotted against the number of them. Even though most of the asteroids are smaller in size, as can be seen in Table 2.1, the bigger asteroids still account for most of the volume in space. Due to the small size (less than 100 m in diameter) of the estimated 25 million asteroids, their detection is highly unlikely. The approximation of the number of asteroids and their sizes generally follows a power law, shown in Equation 2.1, which is a cumulative diameter distribution from [30].

$$N(>D) = KD^{-b} \tag{2.1}$$

where K is a scaling factor and b is the cumulative diameter population index and N is the number of asteroids larger than diameter D. According to [30], for a frequency size distribution of asteroids, the exponent of the power law is generally between values -4, for large sizes, to -1 at smaller ones. The index can also change according to the location of the asteroids.

Most of the measured diameters are from infrared surveys of asteroids, such as IRAS [3] and WISE [4]. The rest of the estimated sizes of asteroids is estimated using an assumed value for the albedo of the asteroid, which leads to errors higher than 100%, as is discussed in more detail in Chapter 3.1.2.

D	100 m	300 m	500 m	1 km	3 km	5 km	10 km	30 km	50 km	100 km	200 km	300 km	500 km	900 km
N	~25 000 000	4 000 000	2 000 000	750 000	200 000	90 000	10 000	1100	600	200	30	5	3	1

Table 2.1: Approximate number (N) of asteroids bigger than a certain diameter (D) [10]. This approximation is done using the power law, expecting many more smaller undetected asteroids than the detected ones.

From Figure 2.3, and also according to the observed asteroids, the smaller asteroids are mostly irregular in shape. This is due to their small size, which means that the asteroid cannot exert enough gravitational pull to be spherical in shape. For example, asteroid 216 Kleopatra resembles a dog bone. Only the biggest asteroids have gravity strong enough to resemble spheres. It is interesting to mention that many asteroids are not one solid object either, but piles of rubble held together by gravity. They were most likely formed in collisions [27].

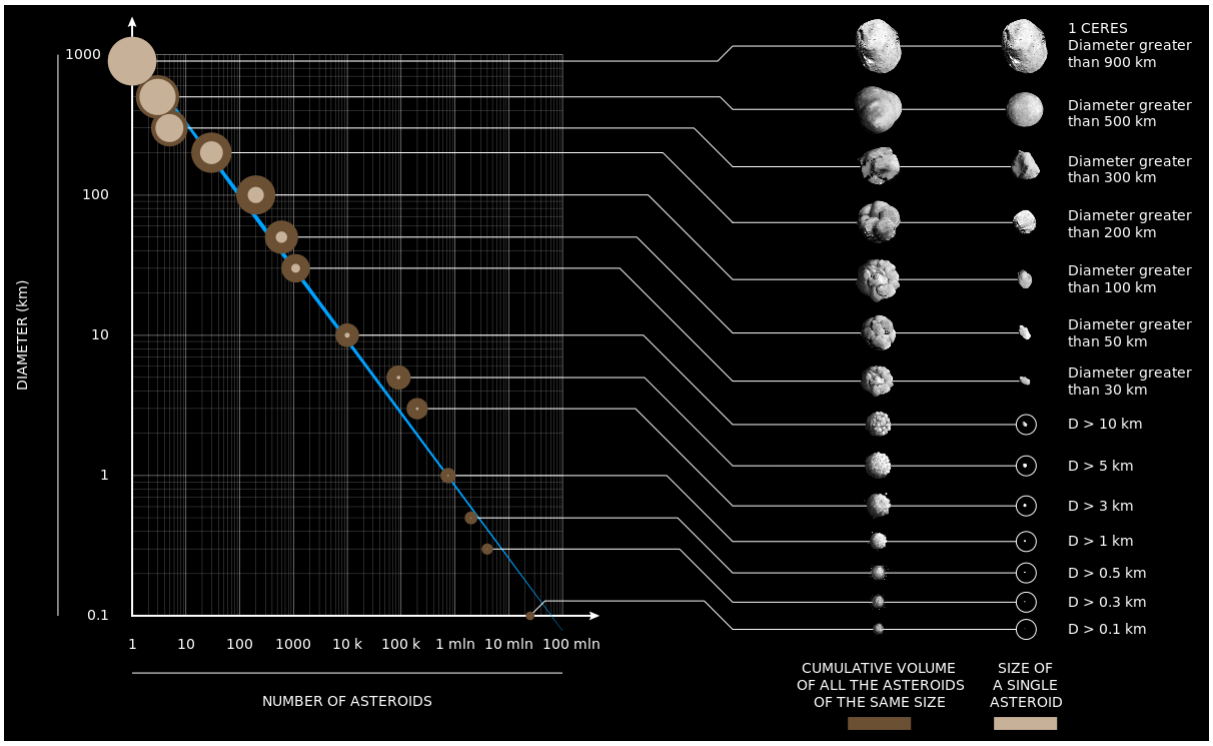

Figure 2.3: Size and number of asteroids in the solar system, not taking into account Trojans, Centaurs or other asteroids, which could be considered minor planets [10]. As in Table 2.1, there are few big asteroids, but many small ones. The shape of the asteroid can be also be seen to be less round and spherical as the size of the asteroid decreases.

Asteroids cluster in families and these have very similar characteristics, such as similar shapes. The younger asteroid families have more variety in shapes than the older ones, which tend to be rounder as the shape changes with time. The change into a smoother sphere is caused by small impacts as the asteroids collide with each other and the prominent features get softened. This change has been determined to take one or two billion years [31].

2.2.2 Velocity

The orbit of an asteroid can be determined from the observations of this asteroid. An elliptical path about the Sun can be fitted with the gained data. Observing the object at different positions in the sky can lead to better orbit predictions as the estimation of the orbit is adjusted with every new data. At least three observations on the sky are needed to approximate an orbit [26]. Due to the fact that the asteroid can change its brightness, because of its rotation or a difference in the angle at which the Sun hits the body, it is easy to lose the object after the first viewing. Consequently, the Horizons asteroid database [6] has also uncertainty in the orbit for each asteroid.

The orbital velocity can be calculated by assuming mostly elliptical orbits for the asteroids. The equation which can be used to calculate the orbital velocity is dependent on distance, Equation 2.2:

$$V = \sqrt{\mu(\frac{2}{r} - \frac{1}{a})} \tag{2.2}$$

where V is the velocity, μ is the standard gravitational parameter, r is the distance at which the speed is calculated and a is the semi-major axis of the elliptical orbit.

The average orbital speed in the main asteroid belt can be calculated to be between 15.7-21 km/s, where the closer the asteroid orbits to the Sun, the faster its velocity. The speed of the asteroid influences the detectability of an asteroid as well. The faster the asteroid orbits, the faster it can pass a field of a view of an instrument. However, this depends also on the apparent motion, the difference between the asteroid's and instrument's orbital speed. Depending on the brightness of an asteroid and sensitivity of the instrument, the asteroid might or might not be observed, if the apparent motion is very high.

2.2.3 Albedo

Albedo measures the reflectance or optical brightness of a surface and can be used to determine the composition of asteroid surfaces. In astronomy, two values are referred to as albedo. One is the Bond albedo, and the other is the geometric albedo, which will be referred to as albedo throughout this report.

The Bond albedo is the fraction of power from the total energy received from the Sun that is scattered back to space in all the directions and wavelengths. It helps to determine how much energy body absorbs and can be between 0 (black body-absorbs all the radiation) to 1 (white body-reflects all the radiation). Bond albedo (A) can be related to the geometric albedo (pv) with the following equation:

$$A = p_v q \tag{2.3}$$

where q is the phase integral in terms of the directional scattered flux and phase angle, where the phase angle refers to the direction of the light paths.

The geometric albedo refers to sunlight in the optical region only and is the ratio of actual brightness reflected back towards the source from an idealized diffusively scattering (Lambertian) disk with the same cross-section. The Lambertian object reflects the brightness independently of the observer's angle of view. This geometric albedo can be bigger or smaller than the Bond albedo and depends on the surface of the body. It can be also higher than 1.

In Figure 2.4, geometric albedo as a function of semi-major axis (AU) is plotted. The very distant asteroids seem to have low albedos, thus absorbing almost all the received sunlight. It would be expected that the asteroids detected would be the bright ones (high albedo), as this aids in the detection. Therefore, this data seems to suggest that there is a trend in low albedos at distances further away from the Sun. Albedo ranges from 1 to 0, with most of the asteroids between 0.02 and 0.6. These estimates are taken mostly from infrared observations, WISE [4]. Figure 2.5 shows that most asteroids have albedo values around 0.2 (brighter asteroids) and 0.06 (darker asteroids). The data used for Figure 2.5 have been calculated using the WISE [4] observations. As seen in the next Section, class C, with mean albedo value of 0.05 is the most common asteroid type and class S, mean albedo of 0.18 is the second most common. A lot of other classes have albedo values around these values (0.06 and 0.2) and this would explain the peaks in Figure 2.5. As will be explained later, 3.1.2, the size and albedo values are codependent in optical observations, and therefore mid-infrared is needed to determine precise values.

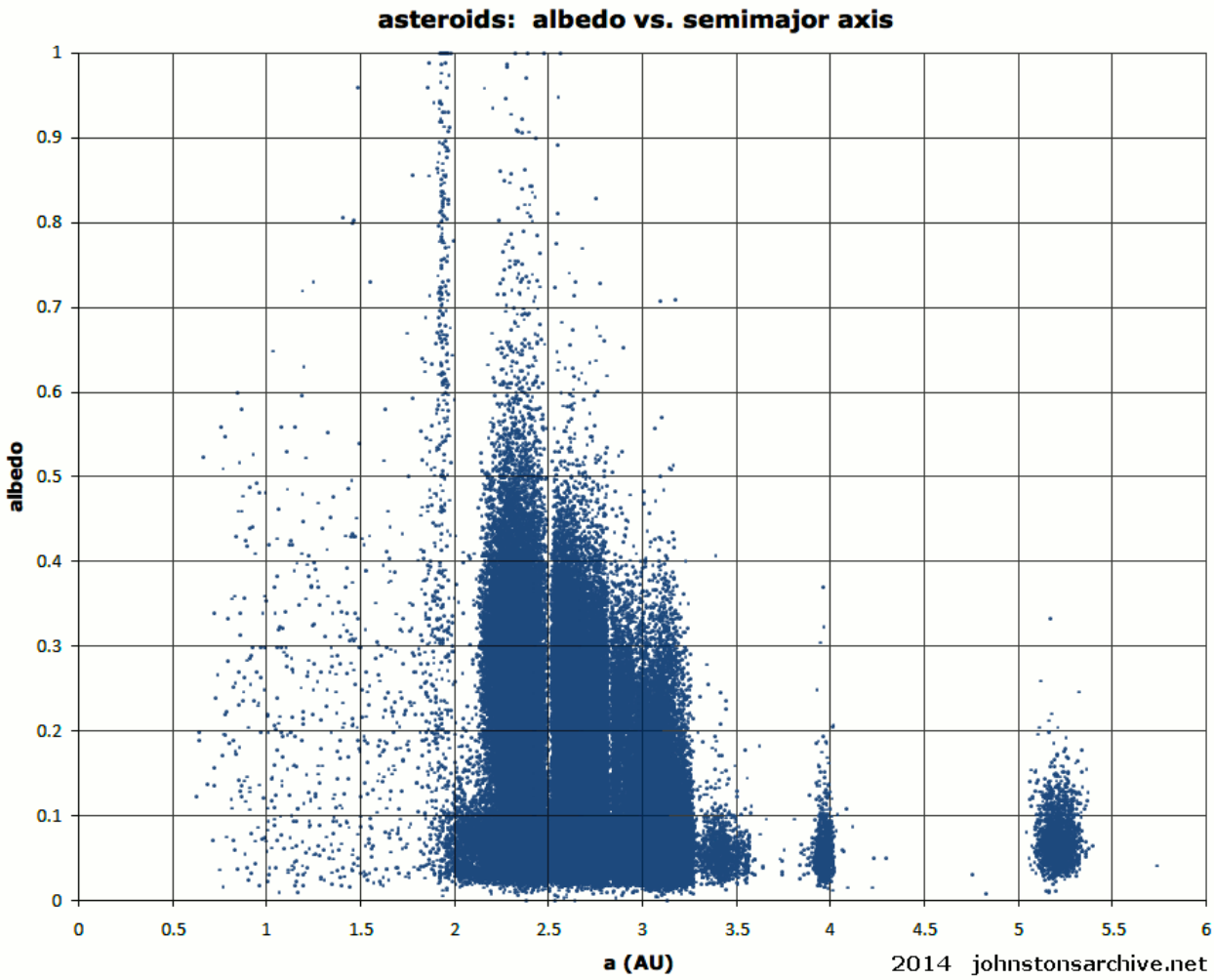

Figure 2.4: Estimated geometric albedo of asteroids w.r.t. distance to the Sun (AU), using data from 139 727 asteroids [15]. The most asteroids seem to be in 0.02-0.6 region, which is the brighter region, favourable for detection. Also less asteroids are detected at further distances, and as could be expected, mostly bright ones.

Knowing the albedo, emissivity, size and the distance to the Sun, the temperature of the asteroid can be estimated. An approximation for the surface temperature of an asteroid as a function of distance to the Sun (AU) is shown in Figure 2.6. This is calculated using asteroid thermophysical models, with thermal properties of carbonaceous chondrite and ordinary chondrite, which are meteorite classifications. The asteroid rotation is assumed to be 6 hours and albedo is 0.02 and 0.1 respectively [16]. In general, the average temperature of an asteroid can be estimated to be 200 K at the inner edge of the asteroid belt, decreasing to 150 K at the outer edge of asteroid belt [32] +- 50 K depending on the albedo, emissivity and size.

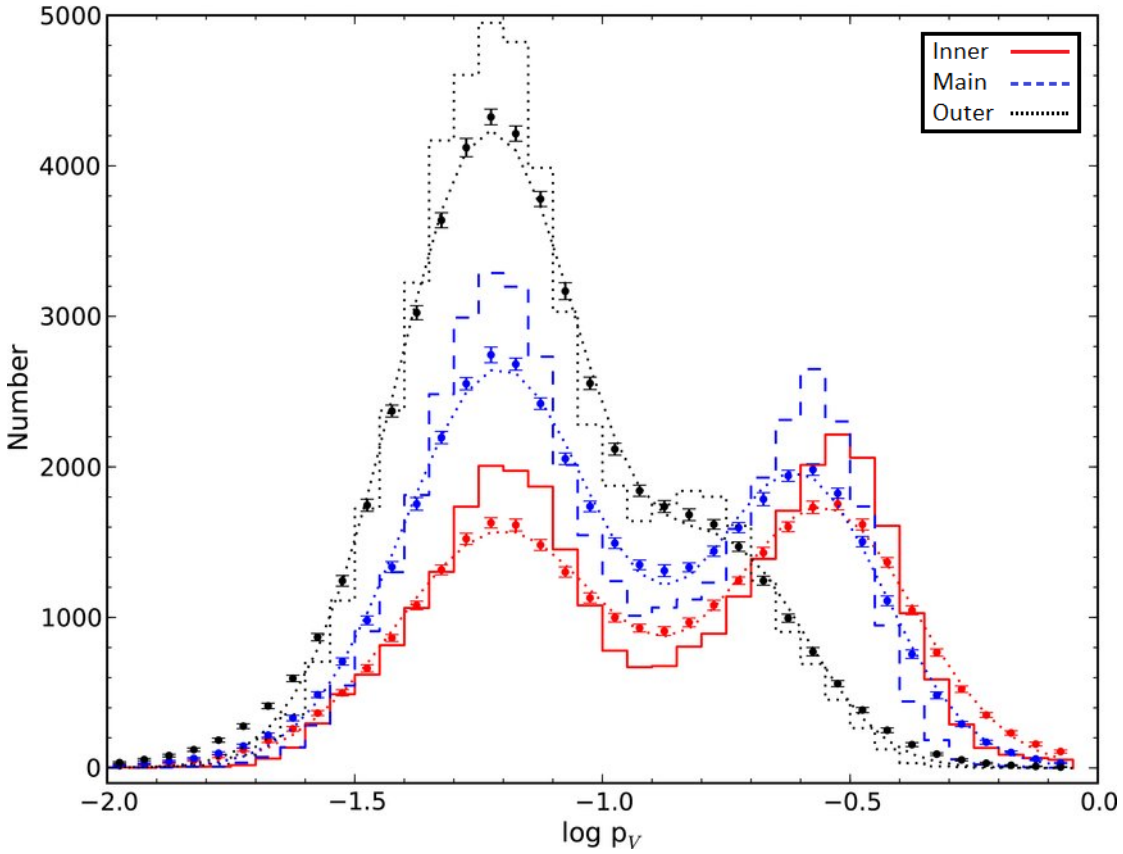

Figure 2.5: Preliminary albedo distributions for 112 265 Main Belt asteroids. Red solid, blue dashed, and black dotted histograms show the inner middle and outer part of the belt respectively. Monte Carlo simulations of the albedos and their error bars are shown as points and the smooth curves show the best-fitting double-Gaussian distributions. [4].

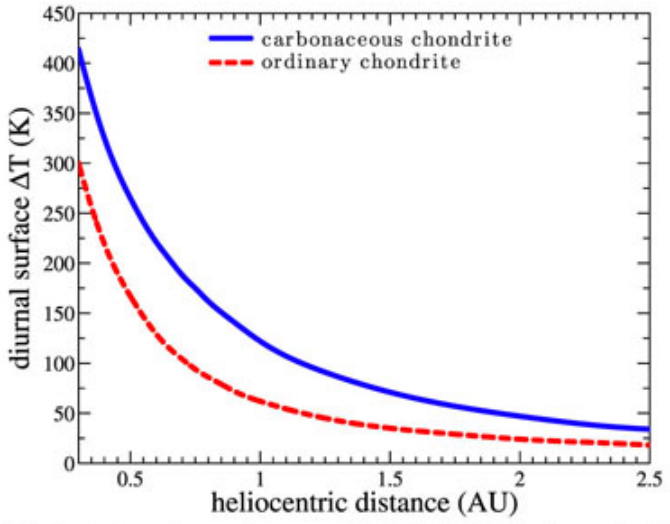

Figure 2.6: Diurnal surface temperature on asteroids as a function of distance to the Sun (AU) [16]. The blue line is approximation for carbonaceous chondrite and red dotted line is the ordinary chondrite. The asteroid rotation is assumed to be 6 h and albedo is 0.02 and 0.1 respectively.

2.2.4 Relative Reflectance

Relative reflectance is a value expressing the ability of the surface of an object, in this thesis an asteroid, to reflect radiant energy. Relative reflectance is dependant on albedo and slope parameter G, which are both dependants on the wavelength. It has been observed that the relative reflectance is higher for longer wavelengths [4]. In Figure 2.7, the estimation of the relative reflectance for the Main belt asteroids is shown [4]. Relative reflectance can be used for calculating the reflected brightness of an asteroid as shown in the next Chapter.

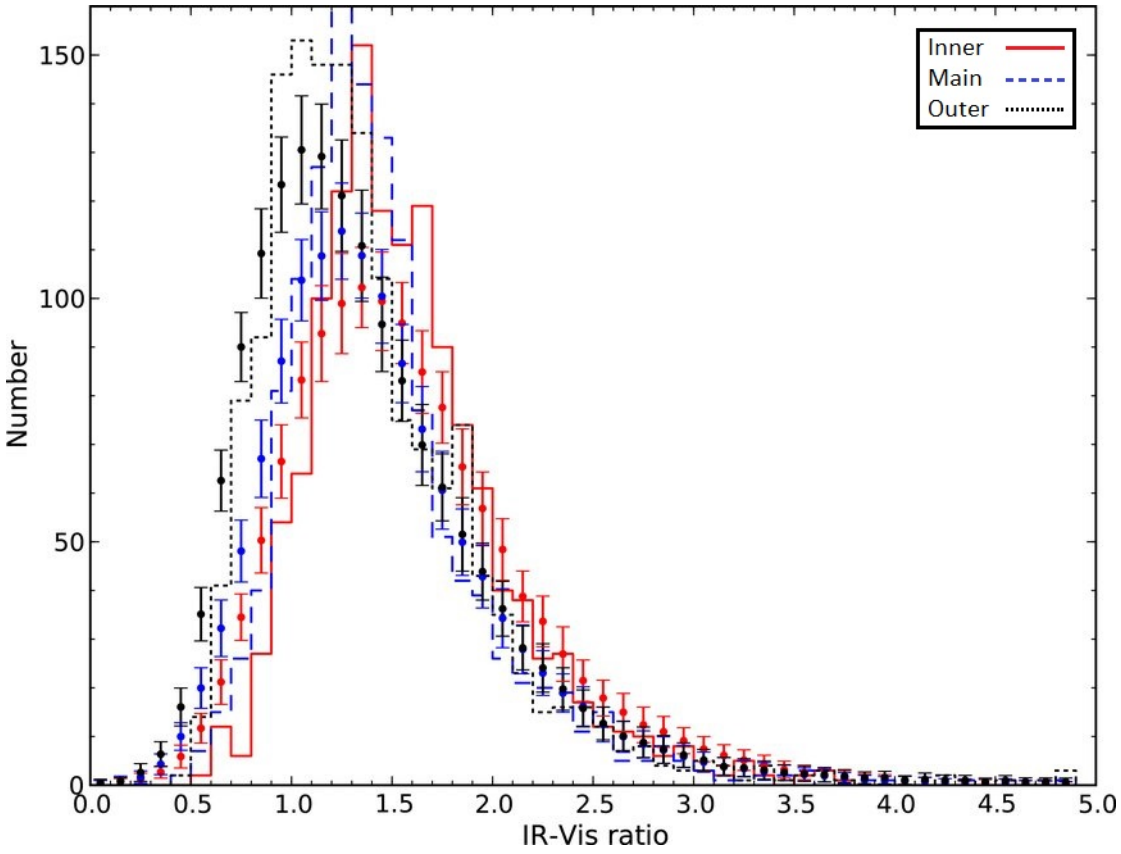

Figure 2.7: Relative reflectance for inner, middle and outer belt asteroids for near-infrared wavelengths shown in solid red, blue dashed and black dotted lines respectively. The points show the mean distribution and errors from Monte Carlo simulations using the infrared WISE observations [4].

2.2.5 Composition

When the size, albedo and mass are known, the density and the material of the asteroid can be estimated. Small asteroids are usually not internally differentiated, therefore the internal and surface composition are assumed similar. However, the bigger ones, such as Ceres, are known to have internal structure.

Spectral Classification

Based on the colour, albedo and spectral shape of the asteroid (emission spectrum), which are properties corresponding to the surface composition of the body, the asteroids are divided according to their spectral classification. There is more than one system of such classification. The two most used are Tholen and Small Main-Belt Asteroid Spectroscopic Survey (SMASS) classification, where the SMASS is a modified version of Tholen. The Tholen classification is explained in more detail in Table 2.2 [33][17]:

Asteroid taxonomic classes		
class	**mean albedo**	**spectral reflectivity (at wavelengths of 0.3–1.1 micrometres [μm])**
C	0.05	neutral, slight absorption at wavelengths of 0.4 μm or shorter
D	0.04	very red at wavelengths of 0.7 μm or longer
F	0.05	flat
P	0.04	featureless, sloping up into red*
G	0.09	similar to C class but with a deeper absorption at wavelengths of 0.4 μm or shorter
K	0.12	similar to S class but with lower slopes
T	0.08	moderately sloped with weak ultraviolet and infrared absorption bands
B	0.14	similar to C class but with shallower slope toward longer wavelengths
M	0.14	featureless, sloping up into red*
Q	0.21	strong absorption features shortward and longward of 0.7 μm
S	0.18	very red at wavelengths of less than 0.7 μm, typically with an absorption band between 0.9 and 1.0 μm
A	0.42	extremely red at wavelengths shorter than 0.7 μm and a deep absorption longward of 0.7 μm
E	0.44	featureless, sloping up into red*
R	0.35	similar to A class but with slightly weaker absorption bands
V	0.34	very red at wavelengths of less than 0.7 μm and a deep absorption band centred near 0.95 μm
other	any	any object not falling into one of the above classes

*Classes E, M, and P are spectrally indistinguishable at these wavelengths and require an independent albedo measurement for unambiguous classification.

Table 2.2: Mean albedos and spectral reflectivity characteristics for asteroid taxonomic classes [11]. C, B, F, G classes form group C, which accounts for 75% of asteroids and stands for carbonaceous (rich in carbon) bodies. S class is the second most common group, made of silicaceous (stony) objects. M, E and P class are from an X group, which is the third most common.

The letter I is used for inconsistent spectral data and for some objects, with properties which are a combination of more than one type, a combined type such as CG-type can be assigned.

The mean reflectance spectra for each of these types is shown in Figure 2.8. Different minerals absorb and reflect light at different wavelengths, and this produces characteristic spectra for different materials. The possible composition can be determined by comparing these spectra to features observed from minerals and meteorites. Unfortunately, the surfaces of asteroids are composed of a mixture of minerals and this might hide the distinct features. Also, the chemical alterations in the surface due to the interaction of solar radiation, solar wind particles and cosmic rays with other bodies can conceal the real composition [27][34]. That is why the comparison to meteorites is important, as they might have similar composition as their parent asteroids. It can be seen, in Figure 2.8, that some spectra are very similar, such as the one for E, M, P-type, which suggests that they are composed of similar minerals.

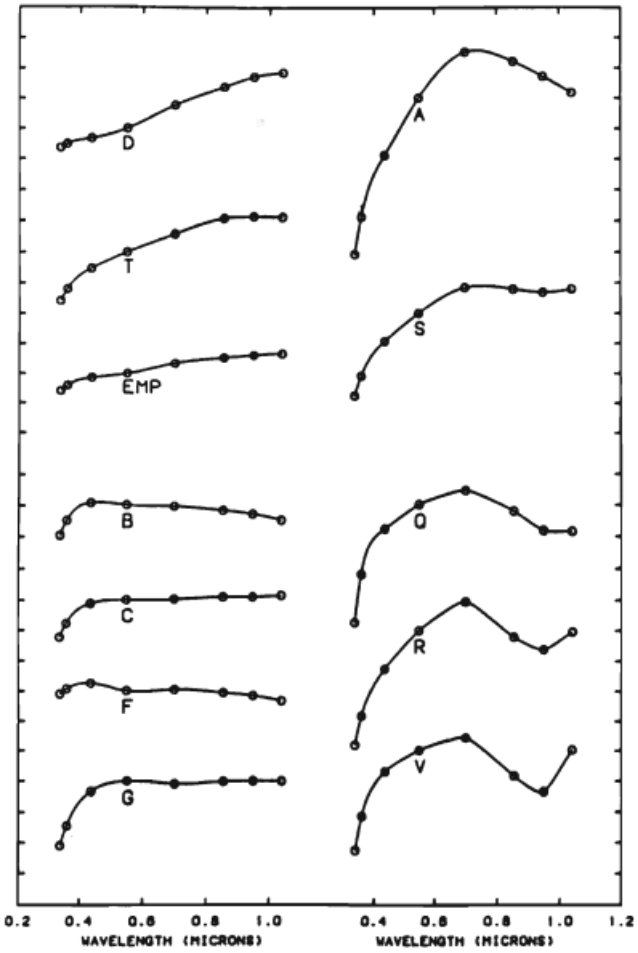

Figure 2.8: Mean reflectance spectra for the 14 types (1989) [17]. E, M, P asteroids (group X), have similar spectra, but different composition. B, C, F, G have similar spectra as well, as they have a similar composition. F is very similar to B class but differs in low wavelength and "water" absorption feature. G is very similar to C class but differs in low wavelength and absorption feature. The most prominent features have A, S, Q, R and V class, due to their composition (olivine and pyroxene).

3. Observationally derived Properties of Asteroids

To improve the current estimations of the asteroid properties, asteroid observations are needed. Most data are acquired from optical telescopes, as this is the oldest method and was the only possible with the technology for many years. Only in the past century the advantages of observations in other wavelengths have been realized and technology advanced enough to observe the space in them. In Figure 3.1, properties across the range of wavelengths and frequencies are shown. In this chapter, the optical observation and its shortcomings, as well as mid-infrared and its advantages are discussed.

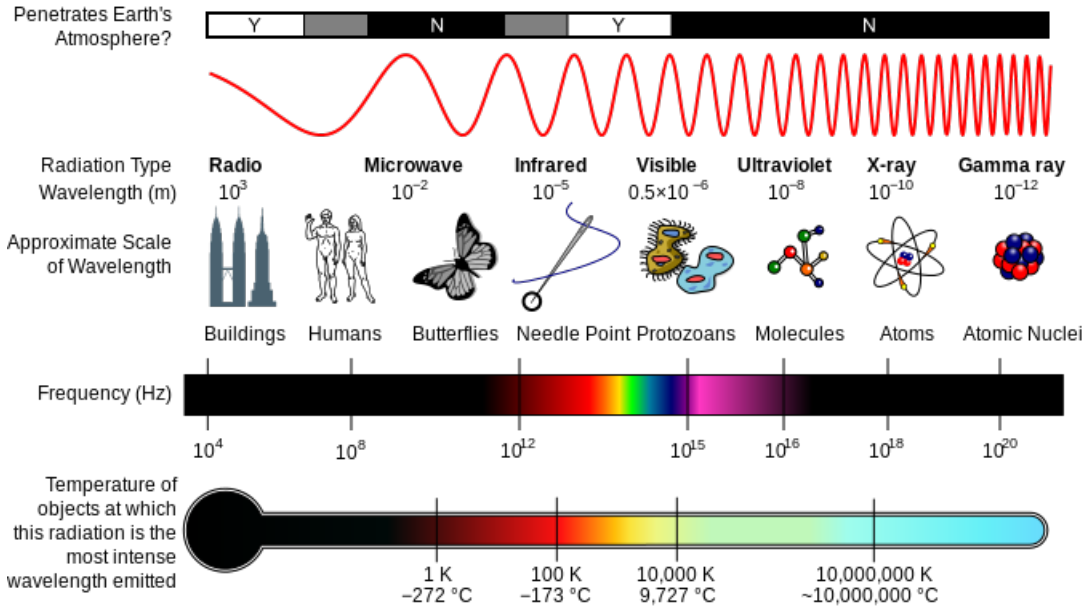

Figure 3.1: The electromagnetic spectrum, showing various properties across the range of frequencies and wavelengths. Infrared has a longer wavelength than visible, seen by human eye, and cannot penetrate the Earth's atmosphere very well (on the top white Y=yes, black N=no, gray=some radiation can pass). Optical spectrum has a bit bigger range than optical, it also includes the near infrared. [18]

3.1 The Advantages and Disadvantages of optical Observations

Observations in the optical spectrum have been very useful when learning about the universe. As mentioned before, most of the data about asteroids are obtained in the optical spectrum. The optical observations have its advantages, but also disadvantages, which will be elaborated on in this Section. Optical observations can estimate very accurate positions for the asteroids, however, the approximation of albedo and size of the asteroid is more problematic.

Optical observations include imaging, photometry and spectroscopy. Detecting asteroids with imaging is nowadays done with the help of a computer program, but the method stays the same. Images, usually more than two, are compared with each other, where a body is followed to determine whether it moves and whether it is an asteroid. From these images, the orbit of the asteroid can be determined. The accuracy of this depends on the number of observations of the object.

Spectroscopy is a more detailed study of the light from an object. In spectroscopy, the light gets spread out in wavelengths which creates spectra, as mentioned in Subsection 2.2.5 and can provide more insight on the object. The composition can be estimated from the emission and absorption lines, which are specific for different materials [34].

Photometry quantifies the flux density from an object. This is usually done by evaluating images at different wavelengths, as the flux density is different for each wavelength. By following the object in time, as it rotates, the amount of reflected sunlight changes. This can be plotted in the so-called light curve, which is a plot of the light intensity of an object w.r.t. time.

3.1.1 Radiation detected in the optical Observations

Optical observations detect the visible and the near-infrared wavelengths. Figure 3.2 shows the Solar radiation spectrum in the optical wavelength at top of the atmosphere of the Earth. Its radiation is as would be expected from a 5525 K black body, which is approximately the surface temperature of the Sun. For an asteroid, the detected radiation, brightness, in optical observations is the reflected sunlight. The reflected brightness can be calculated as [35]:

$$Reflected\_brightness = relative\_reflectance \cdot solar\_flux \cdot 10^{\frac{-(V_{ast}+V_{sun})}{2.5}} \tag{3.1}$$

where V_{ast} and V_{sun} are the apparent visual magnitude of an asteroid and the apparent magnitude of the Sun respectively.

The relative reflectance expresses the ability of the surface of an asteroid to reflect radiant energy, which is wavelength dependent. The apparent magnitude is the measure of the brightness of an object in the space as seen by an observer on the Earth. The apparent magnitude of the Sun is -26.75 according to [36]. The apparent magnitude can be used to determine the absolute magnitude (H) of the asteroid. Which is the apparent magnitude a fully illuminated asteroid would have 1 AU away from both the instrument (observer) and the Sun.

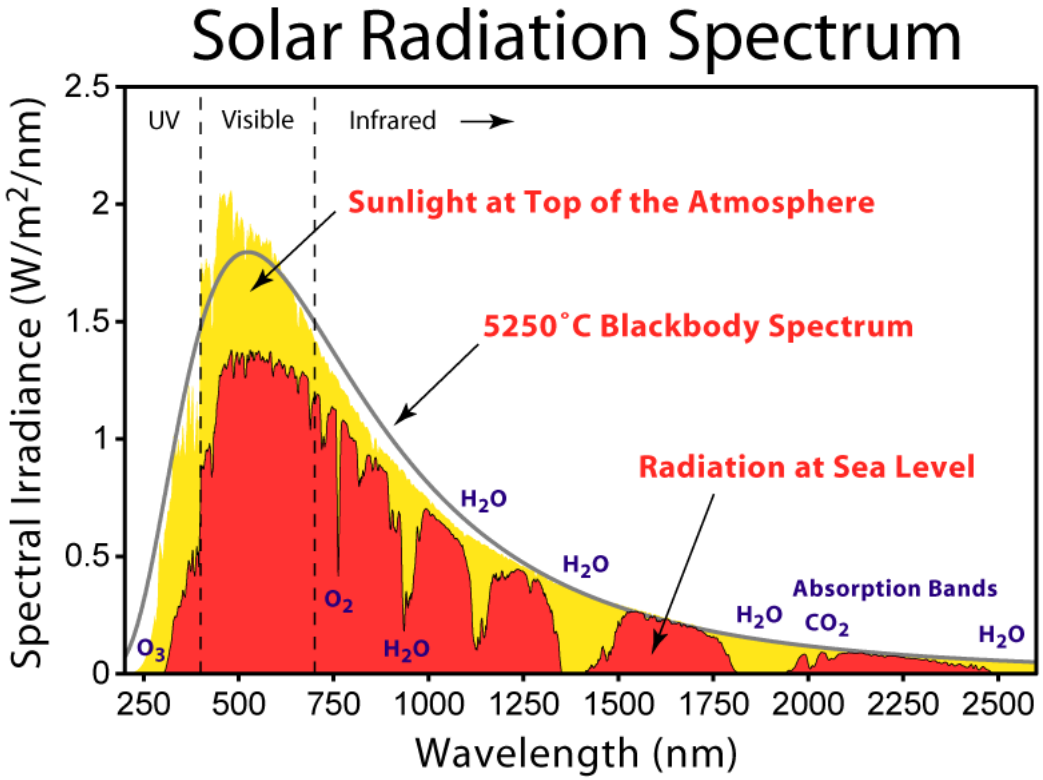

Figure 3.2: The solar radiation spectrum. Shows the radiation at top of the atmosphere (yellow) as well as at the sea level (red). The radiation is similar to a black body of 5525 K, which is approximately the Sun's surface temperature. The radiation at the sea level is different, as some of the radiation is absorbed by the atmosphere at specific absorption bands, it is also not relevant for this thesis as the focus is on a space telescope, nevertheless, this plot shows both. Ultraviolet, visible and infrared regions are shown [19].

The apparent magnitude depends on the size and the albedo of the asteroid. A bigger size means bigger reflection area therefore brighter. A higher albedo means more reflected light, therefore brighter. As can be seen in Figure 3.6, an asteroid of small size but high albedo can emit the same brightness as a big asteroid with a low albedo. Therefore, the brightness received in optical wavelength depends both on the size and the albedo of the asteroid and only a value expressing a combination of both can be properly measured.

3.1.2 Determination of the Size of an Asteroid from its absolute Magnitude

A system to predict the magnitude of an asteroid, depending on its phase angle, where a phase angle is the Sun-Asteroid-observer(Earth) angle, is the H/G magnitude system. H is the absolute magnitude of an asteroid, given as the apparent magnitude of the object if it were 1 AU from the Earth (the observer) and 1 AU from the Sun and fully illuminated, which means a zero phase angle. G is the slope parameter, related to the opposition effect, which is the brightening of a surface when illuminated from behind the observer. This depends on the roughness of the surface and its known only for few asteroids, hence for the rest, the value of 0.15 is assumed [20]. For both H and G, their value is an average over several approximations, because it is affected by the position of the object's rotational axis and the shape [20].

In Figure 3.3, the magnitude of the brightness of an asteroid can be seen plotted as a function of the phase angle. The absolute magnitude is 7.35 at 0 degrees phase angle. The red line is the reduced magnitude, which is the brightness only as a function of phase angle, the distance is assumed to be 1 AU from the Sun and the Earth. The apparent visual magnitude is much higher (which means less bright), and this is due to its distance from the Earth and the Sun not being the desired 1 AU. The distance between the Earth, the Sun and the asteroid is, in reality, bigger than 1 AU. This means that the bigger the distance between the asteroid, the Sun and the observer, the higher the apparent magnitude= the fainter the asteroid. The absolute magnitude should, however, be the approximately same for an asteroid observed at different positions.

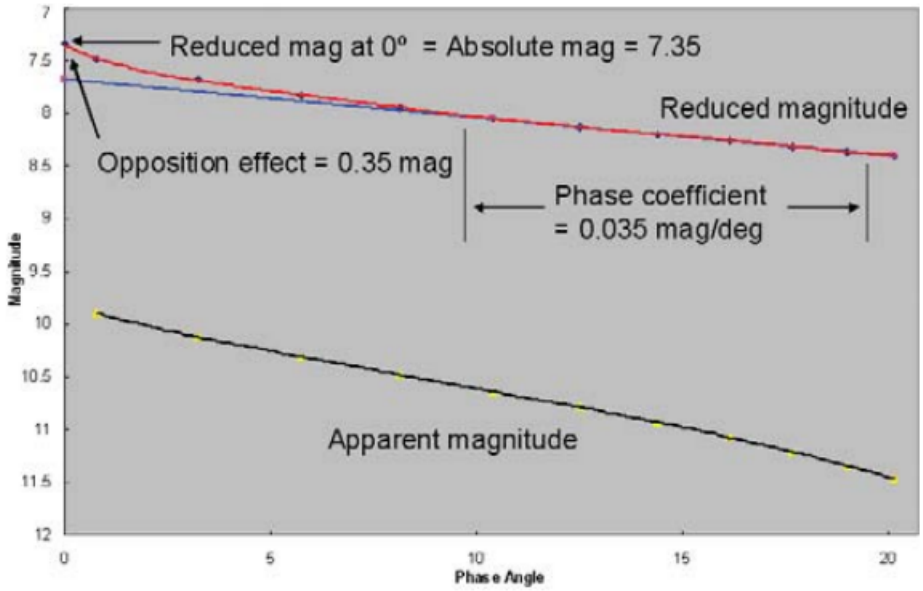

Figure 3.3: Effect of phase angle on magnitudes. The black line is the apparent visual magnitude, which assumes the actual Sun-Earth distance. The red line is the reduced magnitude, where the Sun-Earth distance is assumed to be 1 AU and the blue line is the reduced magnitude without the opposition effect, which is a surge in brightness at 0 degrees phase angle due to the light getting scattered by the particles on the asteroid's surface [20].

This can be used to determine the size of an asteroid. In the optical spectrum, the brightness of the

object is measured, however, as already mentioned, the brightness of an asteroid does not depend only on the size, but also the albedo and distance. This leads to errors in the size and albedo estimations. Optical observations detect the bright asteroids, passing close at the moment when they reflect the most light, which makes small and dark objects harder to detect. Nevertheless, when the position of the asteroid is known at the time of the observation, the distance between the Earth and the Sun can be calculated. With these distances, the H and G can be estimated from the apparent magnitude [20], or the other way around, they can be used to determine the visual (apparent) magnitude of the body at any time. Using this H and an albedo (usually in the range of few percent), the diameter [km] can be calculated using Equation 3.2 [37].

$$D = 10^{-H/5} \frac{1329}{\sqrt{p_v}} \tag{3.2}$$

where pv is geometrical albedo. However, this kind of estimation can lead to big uncertainties, as the albedo and diameter are dependent on each other in the visible light and the albedo range for asteroids is usually between 0.02-0.6, as discussed previously. This could lead to errors bigger than 100%. If the size could be determined from mid-infrared observations, as shown in the next section, the albedo could be found from this equation.

3.2 The Advantages of mid-infrared Observations

Mid-infrared observations are done at longer wavelengths, as can be seen in Figure 3.1. Infrared radiation is emitted by almost every object in space. Many astrophysical phenomena, such as planets or interstellar dust or asteroids are relatively cold and therefore radiate primarily at infrared wavelengths. Dust absorbs and re-radiates optical and ultraviolet light, therefore a lot of the radiant energy is in the infrared. However, the infrared cannot properly penetrate the Earth's atmosphere, and therefore the use of space telescopes which can detect the radiation leads to better observations. Infrared observations also include imaging, spectroscopy and others. Infrared imaging has been done with IRAS [3] or WISE [4] for surveys of asteroids. Spectroscopy has been realized mostly by the Spitzer Space Telescope's Infrared Spectrograph instrument [38].

3.2.1 Radiation detected in the mid-infrared Observations

Infrared observations are also advantageous when observing asteroids, as infrared is the part of the spectrum where their radiation is most intense, as can be seen in Figure 3.4. It can be seen that the reflected brightness is much lower than the thermal brightness, less than 0.2 mJy and the highest brightness is around 20 micron. Therefore, detecting an asteroid in mid-infrared is more likely than in optical. Also, small and dark asteroid have a higher chance of detection. The reflected brightness follows a similar curve to that of the Sun, as it is only the reflected radiation. It scales with the albedo, apparent magnitude and distance to the Sun.

For an asteroid, the detected radiation in mid-infrared wavelengths is mostly the thermal radiation. This can be seen in Figure 3.1 as well as in Figure 3.5, where the temperature range of asteroids in the Main belt and the NEOs is 150 - 350 K, as previously explained in Section 2.2.3. This also means that stars are not as bright in the infrared, as their temperature is much higher and they peak at shorter wavelengths. As the heat of an asteroid is not dependent on its reflected brightness, but the size and its internal temperature, also asteroids previously not seen, could be detected, and the estimation of the known asteroid properties could be much improved.

The thermal radiation depends on the temperature of the asteroid as well as the distances between the Sun, the asteroid and the observer. The distribution of the surface temperature of an asteroid is determined by the thermal inertia of the asteroid. Thermal inertia measures the resistance of a material to a temperature change and it depends on the surface composition and shape (e.g. particle size) of the asteroid.

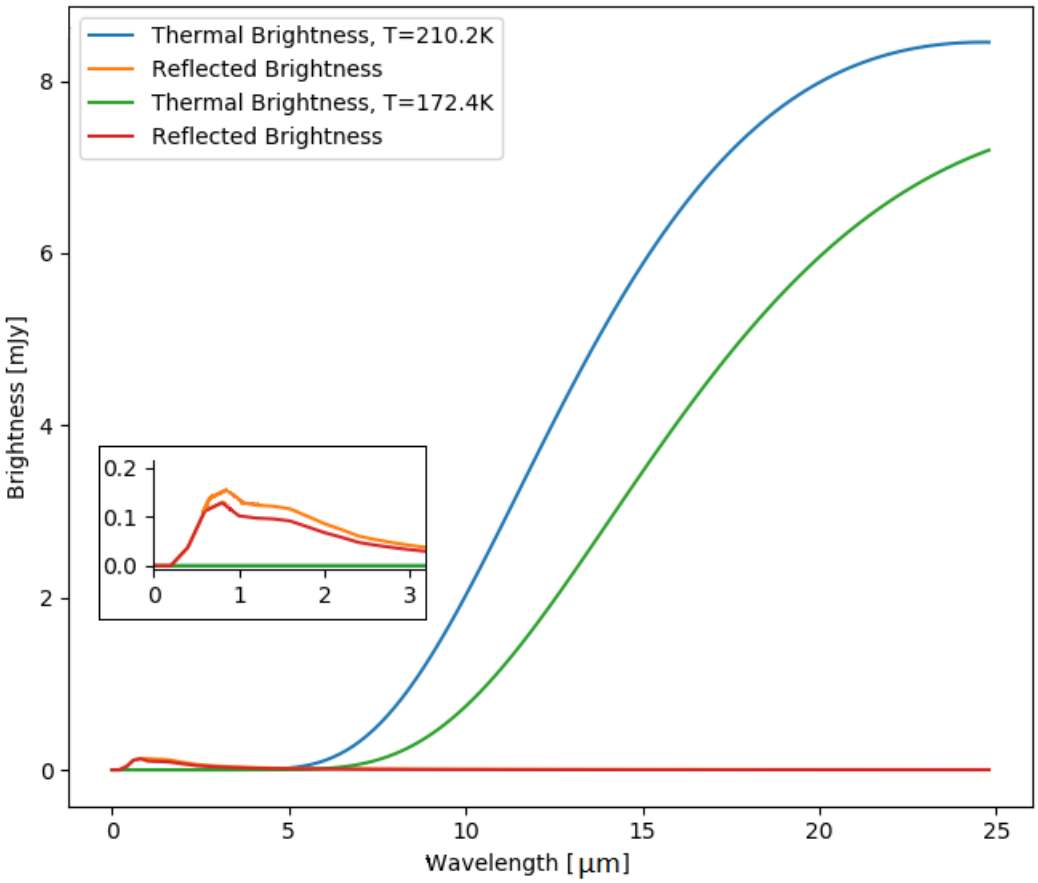

Figure 3.4: Plot showing the brightness received by James Webb Space Telescope, discussed in Chapter 4, from 2 asteroids depending on the wavelength. The blue and orange line shows the thermal brightness and the reflected brightness for the first, warmer asteroid, which means a higher thermal brightness. The green and red show the thermal brightness and the reflected brightness for the second colder asteroid. The reflected brightness is very similar, as the albedo used for both of them was 0.2, only their apparent magnitudes are different. This graph was made using the tool created during this thesis, which is explained in Chapter 5.

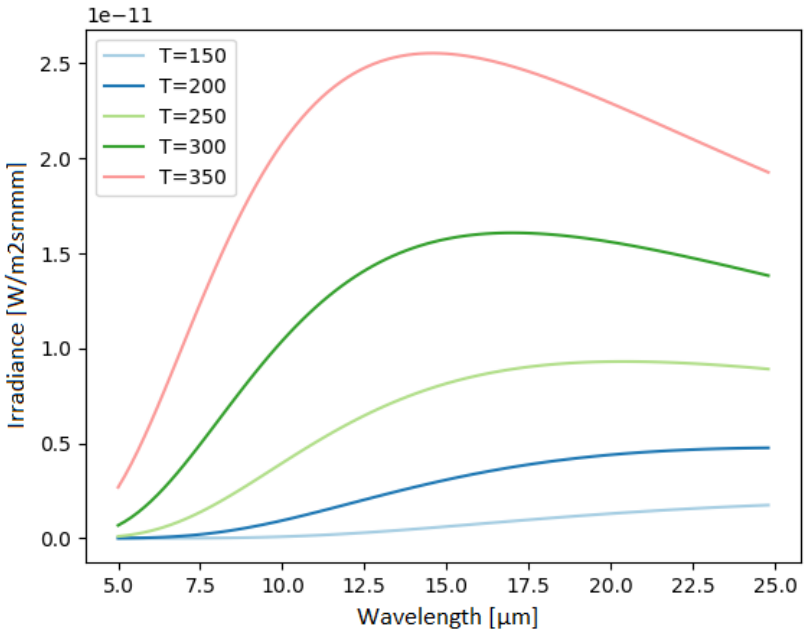

Figure 3.5: Irradiance, calculated using the Planck's law, w.r.t. the wavelength at different temperatures of an object. Higher the temperature, shorter the wavelength at which the irradiance peaks. Therefore asteroids, temperature between 150 - 350 K, peak in the mid-infrared wavelength.

3.2.2 Determination of the Size of an Asteroid from its thermal Brightness

A big advantage of infrared, as seen in Figure 3.6 is that the brightness of an asteroid depends on its size. As mentioned before, the brightness of the object in optical depends on the size, albedo and distance. However, when using infrared observations, the heat is detected and that is more directly related to the size. A larger asteroid appears brighter, as has a bigger area to emit its heat from. The asteroid absorbs and reflects light received from the Sun, and then emits the absorbed light in the infrared spectrum, as heat. This means that the brightness received by the observer is mostly thermal radiation, which is independent of albedo.

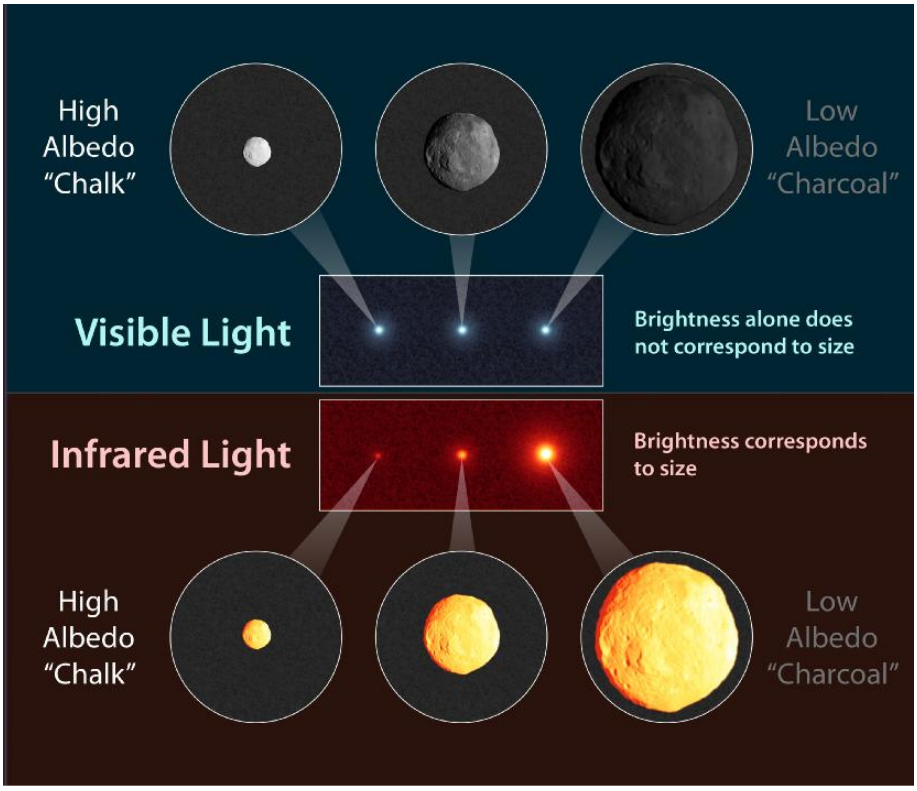

Figure 3.6: Determination of asteroid size in optical light and in the infrared [21]. In optical observations, the brightness of an asteroid depends on its size and albedo. In the infrared, the brightness of an asteroid depends on its size.

As explained in [4], if the object has a known orbit, phase angle and distances between the observer and the Sun, the observed thermal flux can be used to determine the total emitted flux at the surface. At longer wavelengths, the thermal radiation becomes the dominant flux seen by the instrument, as seen in Figure 3.4 and therefore the albedo of the asteroid and the reflected brightness become negligible. Then, with assumptions for some physical properties, such as the beaming parameter or the absolute magnitude of the asteroid, the diameter can be determined from a single band detection. If more simultaneous infrared measurements at multiple wavelengths are taken, a beaming parameter, discussed in more detail in the next Subsection, can be estimated. Together with the optical observation, the albedo can be fit using these two datasets.

When infrared and optical are combined the size and albedo can be determined, using the fact that the infrared radiation emitted and the solar radiation absorbed must balance each other. For this, thermal models, describing how the body emits heat, are used. The most used one is the Near-Earth Asteroid Thermal Model (NEATM) [39].

However, the uncertainties in the physical data can lead to wrong approximations of diameter in the

infrared spectrum as well. A rough surface can lead to different reflectance than a smooth surface, as mountain slopes might seem warmer or colder. In extreme cases, the infrared diameter can be measured to be 35% larger than in reality, as the asteroid might emit as a flat disk. However, usually, the error in the estimation is up to 10% [4]. Rotation also has an impact, because as an asteroid spins, it emits thermal radiation also on the night side of the body, which reduces the signal received by the observer. Wrongly estimated albedo has also the slight effect on the asteroid's diameter [40]. Nevertheless, the estimates made with the help of infrared are much better than the ones determined only with the optical observations. The ideal case is the use of data from multiple observations, both in optical and in the infrared. At the moment, most of the observation data are from optical, therefore infrared observations of asteroids could lead to a great contribution to the estimation of asteroid properties. Mid-Infrared Instrument (MIRI) is a scientific instrument with capabilities in the infrared spectrum. This new instrument will be launched in near future and therefore the possibility of its use for this cause is in more detail explained in next Chapter 4.

3.2.3 Near-Earth Asteroid thermal Model

The thermal emission of an asteroid can be estimated with the Near-Earth Asteroid Thermal Model [41]. This thermal model is nowadays commonly used for almost all the asteroids, not just the Near-Earth ones.

NEATM is a modified standard thermal model (STM). The STM is based on an asteroid of spherical shape, where observations are assumed to take place at opposition (the sunlight comes from behind the observer) and thermal inertia, the resistance to changes in surface temperature related to thermal conductivity, is neglected. This determines the temperature distribution on the surface, as zero thermal inertia means that the temperature would drop to zero right after the sunset. The STM produces generally good approximations for large, bright main belt asteroids.

NEATM uses a basic principle that the incoming solar radiation is assumed to be in instantaneous equilibrium with the thermal emission of the surface of the asteroid. This balance is as [41]:

$$\eta\epsilon\sigma_B T^4 = \frac{S_0(1-A)}{r^2} cos\theta_i \tag{3.3}$$

where η is the beaming parameter, ϵ is the emissivity, σ_B is the Stefan-Boltzmann constant, T is the temperature, S_0 is the solar constant (1367 W/m^2), A is the bolometric bond albedo, r is the asteroid's heliocentric distance in AU and θ_i is the solar incidence angle.

The beaming parameter describes the effective surface temperature. This estimates the effects of the enhanced sunward thermal emission due to the surface roughness and the thermal emission of the asteroids on the night side, due to the fact that asteroids rotate. This can be explained as the difference between the actual dayside temperature distribution compared to perfectly smooth, nonrotating sphere. It also estimates temperature distribution of the shape of an asteroid, comparing to a smooth non-rotating one. In NEATM, the beaming parameter is used as a normalization or calibration factor.

The modifications made to STM to create the NEATM are explained in [41] and shortly summarized here:

- The beaming parameter is used as a calibration parameter to best fit the data and to compensate for the terms that are neglected by NEATM.
- The infrared phase coefficient is not taken as a fixed value. The actual thermal flux an observer would detect is calculated numerically by taking the solar phase angle into account.

NEATM neglects terms such as thermal inertia, heat conduction, rotation effects, thermal differences due to the roughness of the asteroid surface, the asteroid's actual shape and the orientation of the spin pole.

To calculate the thermal flux expected by the observer, the Planck equation as a function of temperature is integrated [41]:

$$F_v = \pi B_v \tag{3.4}$$

where F_v is the thermal flux at a specified frequency and B_v is the spectral radiance of the body, determined by equation [42]:

$$B_v(v,T) = \frac{2hv^3}{c^2}\frac{1}{e^{\frac{hv}{k_B T}} - 1} \tag{3.5}$$

where v is the frequency, h is Planck constant, c is the speed of light in the medium, and k_B is the Boltzmann constant.

Therefore, it can be seen that the thermal flux is a function of the temperature of the body. If the flux is known, using the shown equations, the diameter can be estimated. As the luminosity (L) of an asteroid can be approximated by [27], which comes by integrating the Equation 3.4:

$$L = 4\pi R^2 \sigma_B T^4 \tag{3.6}$$

where R is the radius of an asteroid. It should be mentioned that an error in the measured flux leads to errors in diameter and albedo estimations.

4. Mid-Infrared Instrument (MIRI) on Board of James Webb Space Telescope (JWST)

MIRI, Figure 4.1, is one of the scientific instruments on board of James Webb Space Telescope (JWST). JWST is a space telescope, a successor to the Hubble Space Telescope and Spitzer Space Telescope and is shown in Figure 4.2. It is named after James E. Webb, the 2nd NASA administrator, who played an important role in the Apollo program. JWST is scheduled to launch at the end of March 2021 and it is the most sensitive facility to go into space. The mission objective of JWST is to study the origin and evolution of galaxies, stars and planetary systems. The primary aim is to examine the first light of the universe. It is designed for a 5-year mission, with a 10-year long goal. Its orbit will be the halo orbit at the Earth-Sun Lagrangian point L2, 1.5 million km from the Earth [43], also shown in Figure 1.1. JWST has on board four pioneering science instruments with performance in the infrared part of the spectrum [44] [45]. These are:

- Near-Infrared Camera (NIRCam)
- Near-Infrared Spectrograph (NIRSpec)
- Mid-Infrared Instrument (MIRI)
- Fine Guidance Sensor/ Near InfraRed Imager and Slitless Spectrograph (FGS/NIRISS)

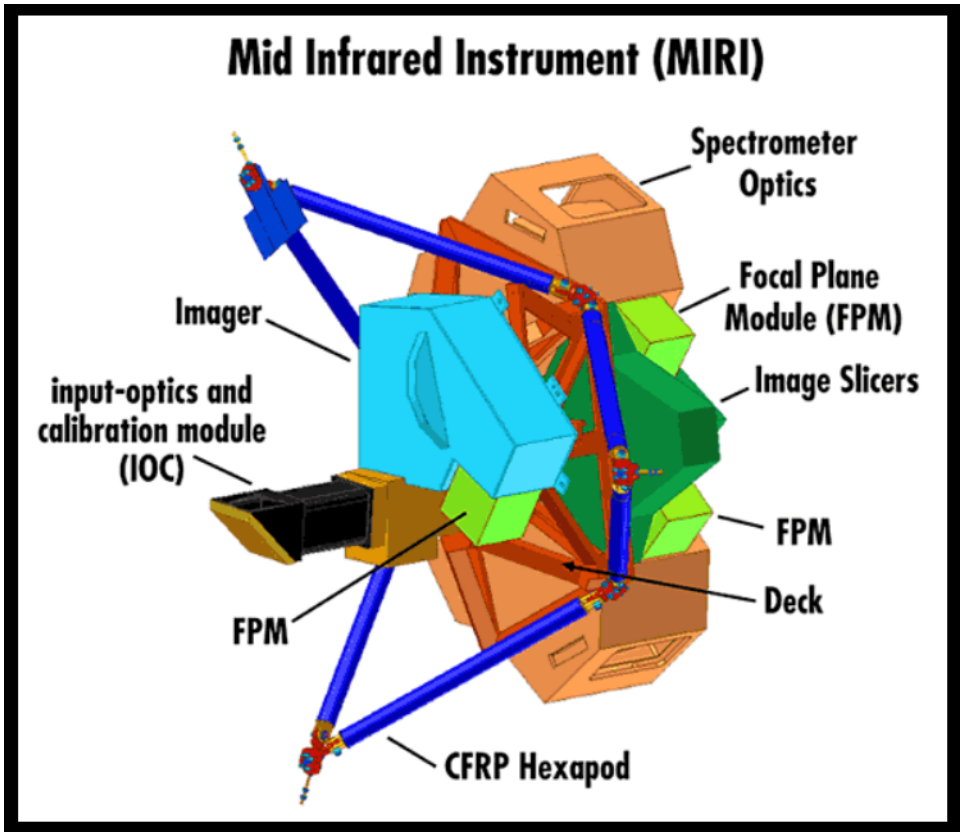

Figure 4.1: Mid-Infrared Instrument without cryocooler. A colorcoded diagram of the instrument is shown. The position of the imager, in blue, is depicted as well [12].

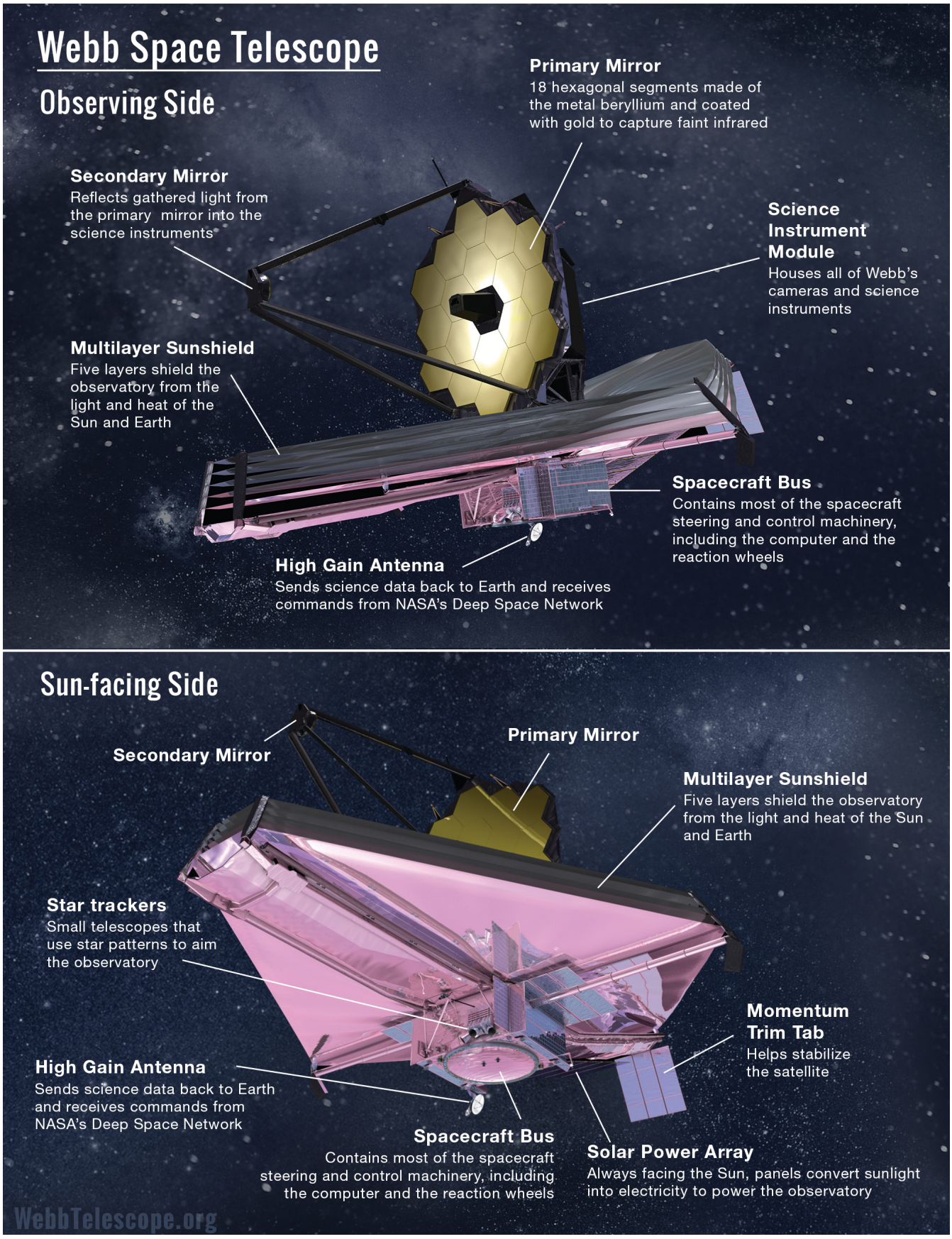

Figure 4.2: James Webb Space Telescope from observing and sun-facing side, showing the position of the mirrors, sunshield, solar panels, spacecraft bus, antenna and the scientific instruments [22].

4.1 MIRI Specifications

MIRI is provided by the European Consortium with the European Space Agency (ESA) and by the NASA Jet Propulsion Laboratory (JPL) and has unprecedented infrared sensitivity. It can provide imaging and spectroscopy observing, covering wavelengths between 5-28 micron [46][47]. MIRI is very sensitive to the thermal background and therefore needs to be actively cooled to less than 7 K by a cryocooler. Three arsenic-doped silicon detector arrays, each with 1024 x 1024 active pixels make up the MIRI instrumentation. A single pick-off mirror feeds the imager (MIRIM) and medium resolution spectrometer (MRS). For both MIRIM and MRS the slow and fast array readout is available. Usually, for the imager, the fast mode is selected, as the slow one is reserved for spectroscopy.

The observation time of MRS and MIRIM is specified by a number of parameters. First, the frame (group) is the time it takes to read out a value for each of the pixels within the image. The integration time for one frame in the fast mode, to cycle through all the pixels is 2.775 s [47]. Second, the integration is a number of frames co-added together, which is also called sampling up the ramp. This is done to improve the signal to noise ratio, which is the signal received from an object on the picture divided by the noise of the picture. This number represents how visible an object is, the higher the number, the stronger the brightness of the object. The strength of the signal received by the MRS or the imager also depends on the sensitivity of the instrument. The third is the exposure time, which is a number of integrations needed to reach the desired depth of the image. The exposure time needed to reach the target depth is determined by how many frames and integrations are required. This can be calculated as follows [12]:

$$t_{exp} = t_{int} n_{int} = n_{group} t_1 n_{int} \tag{4.1}$$

where t_1 is the time between frames, n_{group} is the number of frames, n_{int} is the number of integrations during an exposure, where integration is defined as the time between resets and t_{int} is the integration time calculated from the number of frames and time between them. The total observation time is then the number of exposures multiplied by the time it takes to create one exposure.

The data from the instrument are automatically processed by the JWST Data Reduction Pipeline [48]. The pipeline processes data from all the JWST instruments. This software removes the instrumental signatures, errors, from the data so that they are ready to be used by the user. One such correction is done for transient events, such as cosmic rays. In sampling up the ramp, the value for each pixel should linearly increase with the time. That means the subsequent frames should have linearly increasing values for each pixel. This is the result of illumination, such as celestial source or a background light. However, if a value of a pixel from one frame to another changes significantly, it could indicate a cosmic ray hit or a moving object, such as an asteroid. The pipeline checks these pixels and averages out the values of significantly different pixels.

MIRI's field of view in the telescope focal plane with respect to other scientific instruments is shown in Figure 4.3. The instrument is divided into four modes:

- Imaging
- Low-resolution spectroscopy (LRS)
- Medium resolution spectroscopy (MRS)
- Coronagraphy

In Figure 4.4 a closer look at MIRI's field of view, specifically for each mode can be taken. It can be seen that the imager's field of view is 2 arcminutes offset from the MRS field of view.

The sensitivity of MIRI's imager is shown in Table 4.1. Each imager filter is specified for working wavelength, bandwidth, point source detection limit, extended source detection limit and point source saturation limit. A point source is a point like an unmoving source of brightness and point source detection limit specifies the lowest estimated brightness of the source, which can be detected by the

specified filter. The extended source is a source with an angular size bigger than the resolution of the instrument observing it, e.g. a galaxy. A moving asteroid would be something in between.

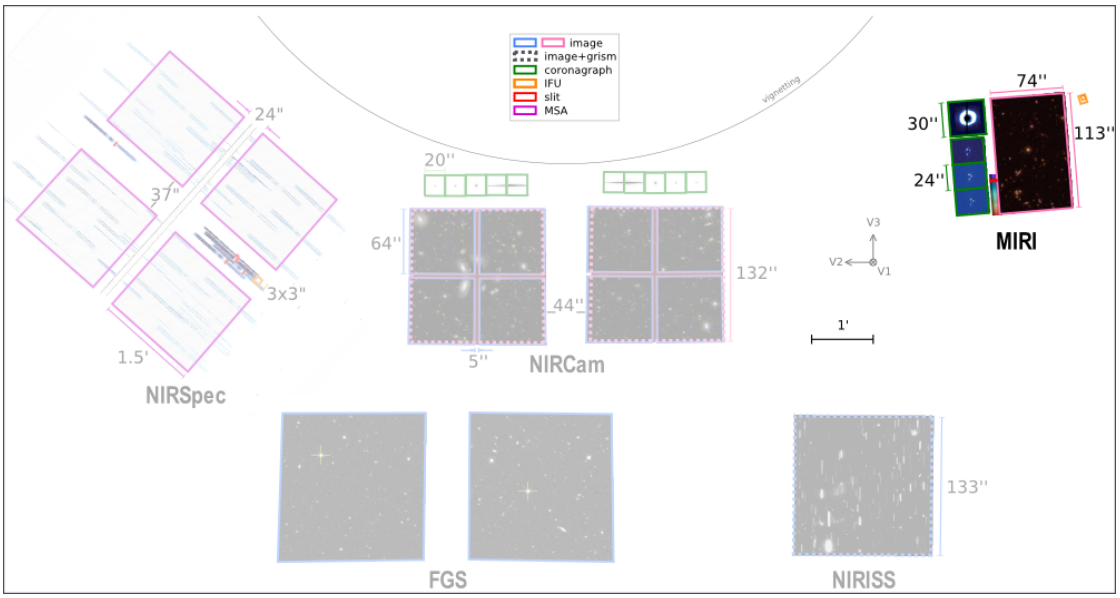

Figure 4.3: JWST MIRI's field of view in the telescope's focal plane with respect to other instruments with a coordinate system V1 (pointing forward from the primary mirror), V2, V3 (anti spacecraft direction) [23].

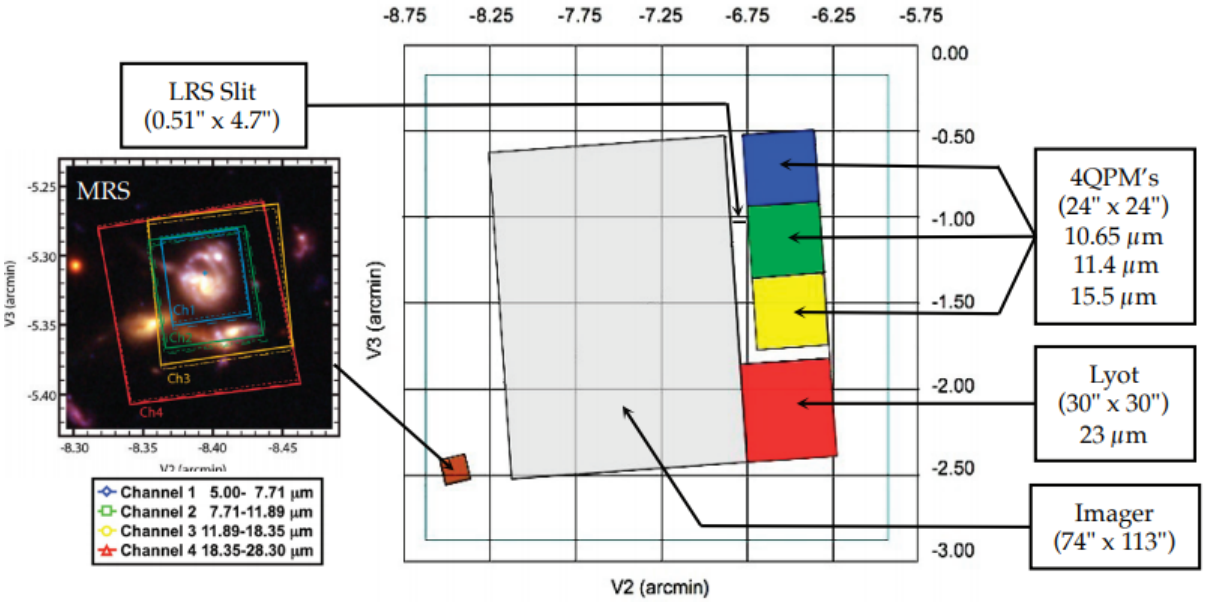

Figure 4.4: JWST MIRI's field of view showing each mode respectively. The slit is for LRS, the orange square for MRS, the grey rectangle for imaging and the colorful squares for coronagraphy. Also showing the vertical and horizontal position in arcmin with respect to V3 and V2, the spacecraft's coordinate system (see Figure 4.3) [23].

Point source detection limit and extended source detection limit are estimated for long-duration observations of faint sources of 10 000 s with signal to noise ratio of 10 and saturation is based on 13% flux falling within the brightest pixel for wavelength of less than 8 μm and 13% x $(8\mu m/\lambda)^2$ for wavelength

Table 4.1: MIRI's imager filter properties: wavelength, bandwidth, full width at half maximum (FWHM), point source detection limit, extended source detection limit and point source saturation limit [12].
[1] Signal/noise = 10 for 10^4 s on-source integration time
[2] Saturation based on 13% of flux falling within the brightest pixel for $\lambda \leq 8\mu m$ and 13% x $(8\mu m/\lambda)^2$ for $\lambda < 8$.

Filter name	λ_0 (μm)	$\Delta\lambda$ (μm)	**Point source detection limit** (μJy)	**Extended source detection limit**[1] $(\mu Jy$ **arcsec**$^{-2})$	**Point source saturation limit**[2] (mJy)
F560W	5.6	1.2	0.182	0.22	7
F770W	7.7	2.2	0.276	0.26	3
F1000W	10	2	0.592	0.53	8
F1130W	11.3	0.7	1.465	1.2	35
F1280W	12.8	2.4	0.945	0.83	15
F1500W	15	3	1.618	0.93	18
F1800W	18	3	3.881	1.9	34
F2100W	21	5	7.55	3.3	50
F2550W	25.5	4	26.959	9.1	105

of more than 8 μm. Saturation by bright sources is undesirable because when saturated, the detector is disturbed and the calibration might be affected and it also reduces sensitivity [12]. However, it is highly unlikely for an asteroid to be bright enough to saturate the instrument. Even for asteroids, which have high brightness (>15 mJy), the signal gets redistributed over the moving streak, as the asteroids have apparent motion w.r.t. the instrument. It is also clear from Table 4.1, that different filters have different detection limits, degrading with longer wavelengths, which could be explained by the conversion efficiency of the filters, as shown in Figure 4.5.

4.2 Advantages of using MIRI

MIRI had a special feature that the imager and the MRS run simultaneously. This means that the user can receive data from both. As the proposals for MIRI's MRS are many, as seen in the proposals for the JWST instruments [13], it means there will be many images taken by the imager as well, but the user of MRS might not be interested in them. However, this images at infrared wavelengths can be used to observe asteroids serendipitously and consequently to determine more properties about asteroids without taking a lot of time from the instrument, as these pictures will be taken while other scientific missions are taking place. This is a really big advantage because there are many science missions which are achievable with JWST's MIRI, more even, than there is available observable time.

MIRI's imager can be used to measure the emitted flux from the object at different wavelengths, depending on the filter chosen. When this flux is received, the asteroid diameter can be estimated. This is done with the help of a thermal model, usually NEATM and some asteroid properties, such as its orbital position with respect to the Sun and the observer. With this diameter and available optical observations, the albedo can be estimated as well. The orbit of the asteroids can be improved as well if the uncertainty has been too high.

There are nine filters, shown in Table 4.1 and Figure 4.5, where the bandwidth and the proton-to-electron efficiency of each of the filters are shown. Depending on the filter chosen, different asteroids can be observed. This depends on the flux emitted from the asteroid, which in turn depends on the size and temperature of the asteroid. Comparing the values in Table 4.1 and Figure 3.4 in the previous Chapter, it stands to reason that the instrument should be able to detect the asteroids in the field of view. Even though the highest brightness is at longer wavelengths (> 20 microns), the sensitivity and conversion efficiency is lower. Therefore, the preferred filter will probably be at the lower wavelengths than 20 microns. The chance of asteroids saturating the imager is not very likely, as the asteroid is brightest at the longer wavelengths, and the filters at longer wavelengths also have higher saturation limits. Also,

the fact that the asteroid moves will decrease the received flux per pixel. Nevertheless, this needs to be simulated and that is the purpose of this thesis.

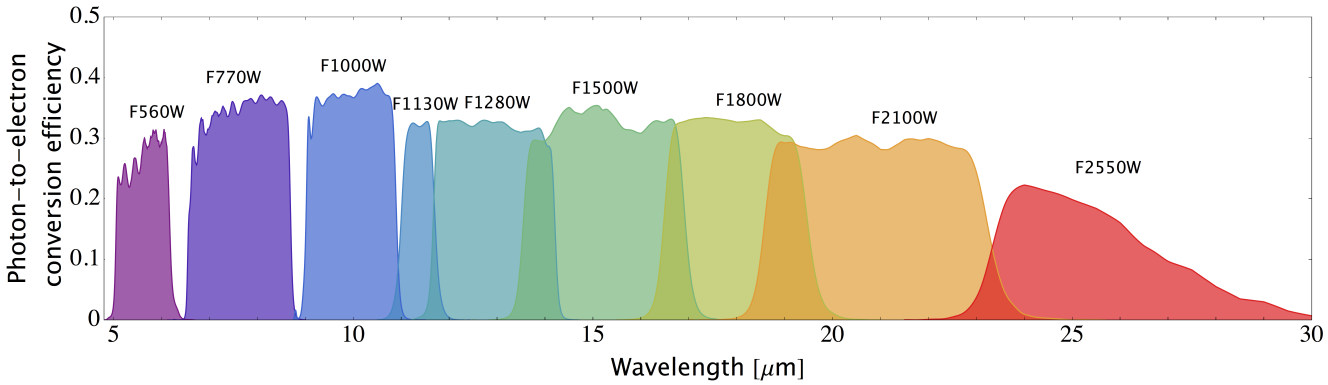

Figure 4.5: MIRI imaging filter bandpasses and their efficiency at different wavelengths [12].

4.3 MIRI Simulator (MIRISim)

MIRISim is a simulator that simulates the data produced by MIRI. This tool is used during this thesis and therefore it is shortly explained here. It can be used for determining the feasibility of observation studies as it simulates the data received by the user. This consists of the observed data, which are modified by the JWST Pipeline. JWST Pipeline is a data reduction software that is used to automatically process the data from the instruments on board of JWST, such as MIRI, to remove instrumental signatures from the observed data. MIRISim is still under development and is created by the MIRI European Consortium, with significant contributors from other scientific institutes [8][9]. A second release of the tool has been recently made available [8]. It should be mentioned that MIRISim is not a sensitivity calculator and for such purposes the JWST Exposure Time Calculator (ETC) [49] should be used.

MIRISim is available for 3 modes of MIRI; the imager, low-resolution spectroscopy (LRS) and medium resolution spectroscopy (MRS). The simulator can output realistic images which can be used to test the performance of the instrument or data for the science team to demonstrate the possible use of the instrument. MIRISim takes the input from a user, which specifies the objects in the field of view and simulates their signature in the instrument. An image FITS file with all the data is created, where each pixel has a value simulated according to the inputs, e.g. the time of the observation, as well as the brightness of the objects. Each image is created from a number of frames, therefore the linear increase in the pixel values can be seen. The data are simulated also according to the number of integrations and exposures.

MIRISim is a python package, which can simulate different instrumental effects of MIRI. It is developed on a best-effort basis to imitate the performance of MIRI in orbit. As explained in [9], some effects of MIRI are still being studied and once they are characterised and quantified, they will be added in the simulator. Therefore, MIRISim represents the current understanding of MIRI. The outputs of MIRISim have been verified with the JWST exposure time calculator (ETC), as well as the MIRI sensitivity model [50].

The user guide for MIRISim is available at [9]. The use of MIRISim is not overly complicated and the general workflow, from [9], can be explained as follows:

- Astronomical scene is created.
- Flux from instrument optics, background and electronics is added.
- Image slicer (MRS or LRS) is simulated.
- Geometric deformations are simulated.

- The image slices are dissipated.
- Random cosmic ray hits, read noise and photon noise are added.
- The simulated observations are created.

The user specifies the details of the desired observation scene and the instrument specifications in multiple input files. In this thesis, the imager mode of MIRISim is used and the inputs for the MIRISim will be discussed in more detail in Chapter 5, where the step by step process of simulating the asteroids is explained.

4.4 Astronomer's Proposal Tool (APT)

Astronomer's Proposal Tool is used to write, submit and validate proposals for the JWST. A proposal from this tool is used during this thesis and therefore a short overview of the tool is given here. It is a stand-alone software, where astronomers can submit their proposals for observations [24]. For each proposal, the user specifies the object or objects to be observed and the science objective. All the proposals go through a selection process to receive the desired time, as there are more proposals than the available time. In Figure 4.6, the front page of the JWST APT is depicted.

There are multiple categories in which users can apply for a time at a specified instrument. Most of the observing time will go to General Observer (GO) programs, which is for everyone. The proposal used for this thesis is from a Guaranteed Time Observation (GTO) category, which is for the scientists who helped with the design of JWST. In GTO, there are 2100 observations for numerous objectives and their summaries can be found in [13].

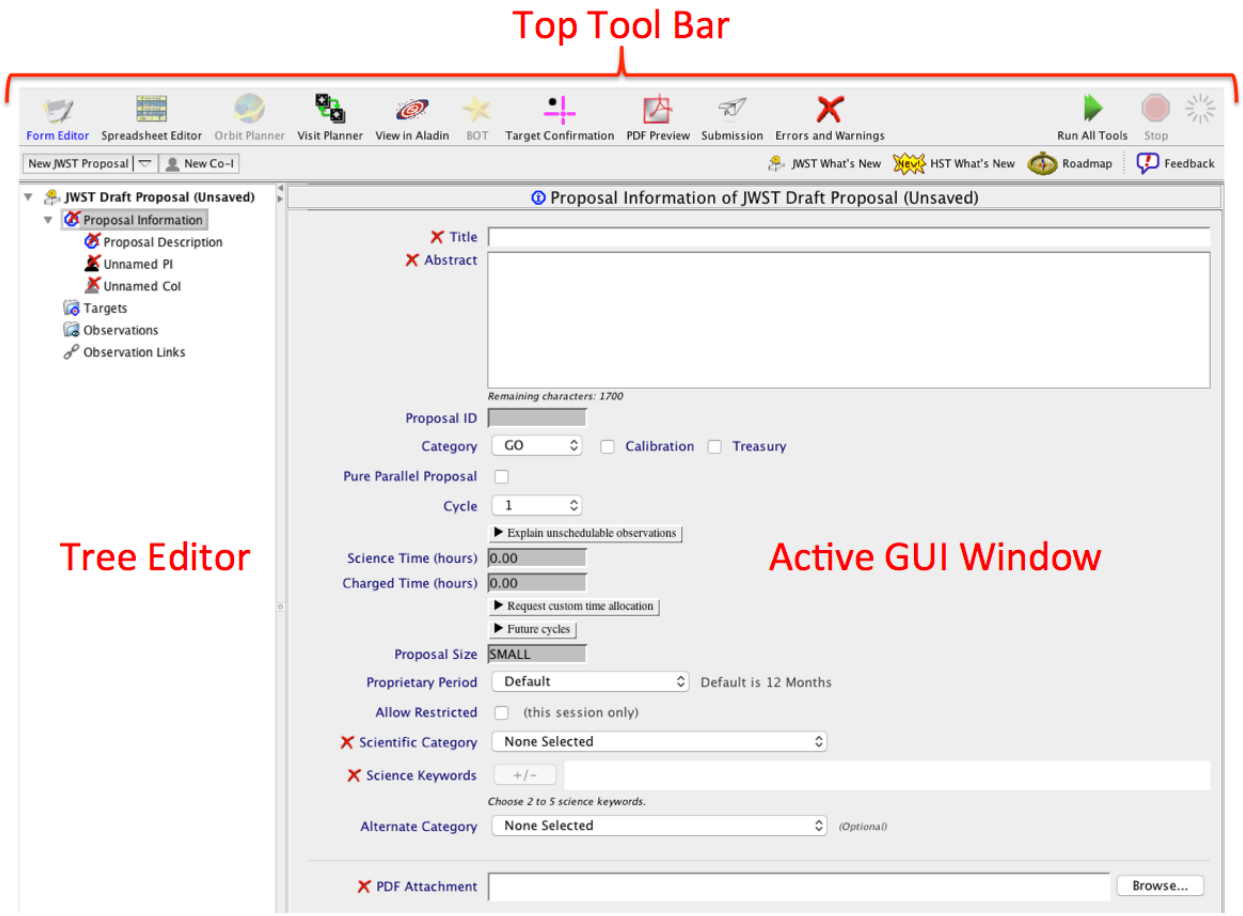

Figure 4.6: The annotated front page of a new JWST APT proposal [24].

The users can perform a number of functions in APT to specify their desired mission purpose and instrument settings [24]:

- Enter the general information about the proposal, such as the title or abstract.
- Define the targets to be observed.
- Specify the observation specifications in more details such as the instrument observing modes and special requirements.
- Visualize how the field of view will look in the sky for the planned JWST observations.
- Check the availability of desired observation times using the APT visit planner.
- Determine the total science time and total allocation time including overheads, which is extra time for instrument pointing adjustments and such.
- Check whether another user is proposing the same observations.
- Submit the proposals for review by STScI.

More about the tool and how to use it can be found in [24], as explaining the use of the tool is not the purpose of this thesis. The use of this tool in this master thesis is to provide realistic inputs, i.e. the direction of the field of view, date and time and instrument specifications, for the simulation of asteroids seen by the MIRI's imager. Using the proposed observations from an existing proposal can simulate more sensible results. Simulations using these inputs can provide reasoning why or why not, would the use of MIRI's imager for the serendipitous observations of asteroids be advantageous. Using cases proposed in APT instead of a randomly chosen inputs creates a better argument to answer the question of this thesis, as can be seen later on in the results Chapter 6.

5. Simulation of asteroids' Signatures in the MIRI's Imager's Field of View

This thesis is focused on determining whether the use of MIRI's imager for serendipitous observation of asteroids is feasible and therefore a simulation proving or disproving this idea has been created during this thesis. In the following subsections this simulation, its use, its theory and its restrictions, are described.

5.1 Introduction to the simulation Tool

The simulation tool has to be able to help answer the questions about the visibility of asteroids from MIRI on board of JWST. This means that the tool needs to be able to take an input, consisting of information about the observation and use this input to determine whether there are any asteroids passing in the field of view. Then simulate how these asteroids ought to be seen by MIRI and evaluate whether they appear visible.

This desired function could be divided into multiple steps, also referred to as smaller functions:

1. **Read an input:** The tool acquires information about the specific observation from an APT file.
2. **Create an input table:** The tool uses the input data and creates a table in MySQL.
3. **Determine the asteroids in the field of view:** Using Serendipitous asteroid detection tool, more closely explained in Appendix A [5], the input table data are used to determine which of the known asteroids are in the field of view of MIRI. This is saved in a new MySQL table with some of their physical characteristics. This detection tool also uses NEATM and estimates the brightness of the asteroid as would be detected by MIRI at different wavelengths.
4. **Determine the temperature of the asteroid:** Using the data from the newly created tables with asteroid data, the temperature for each is determined.
5. **Simulate the asteroids as detected by MIRI:** Using MIRISim, the data, containing the asteroids in the field of view and their characteristics, are used to create a simulated image of the sky.
6. **Calculate the Signal to Noise ratio of the asteroids:** Evaluating the simulated data, the visibility of the asteroids is determined by calculating the signal to noise ratio (SN) of each of them.

The simulated image can then be evaluated to determine if the asteroids are indeed visible. This is done in Chapter 6, where many different questions about the usefulness of this possible use of MIRI are discussed.

A flowchart of the tool is shown in Figure A.1. The flowchart shows the steps as the pink boxes, the data which flow from one function to another in the yellow circles and the output of the simulation in the blue box. The outputs of this simulation are the simulated images, which are used to determine the ratio of the asteroids visible by MIRI w.r.t the asteroids expected to be in the FOV of the MIRI's imager. This is done by determining the SN and hence answering the main thesis question.

5.2 Development of the Tool

Each of the steps has been developed and then connected together to create a working tool. This tool is created using Python 2 because MIRISim at the date of starting this thesis was only available for Python 2. At the beginning of this thesis, the launch date of the JWST was 2020, therefore many simulations are done for dates in the year 2020, as these were the potential dates specified in the APT file. This does not have an impact on the reliability of the results, as choosing this random period of time is as good as any other.

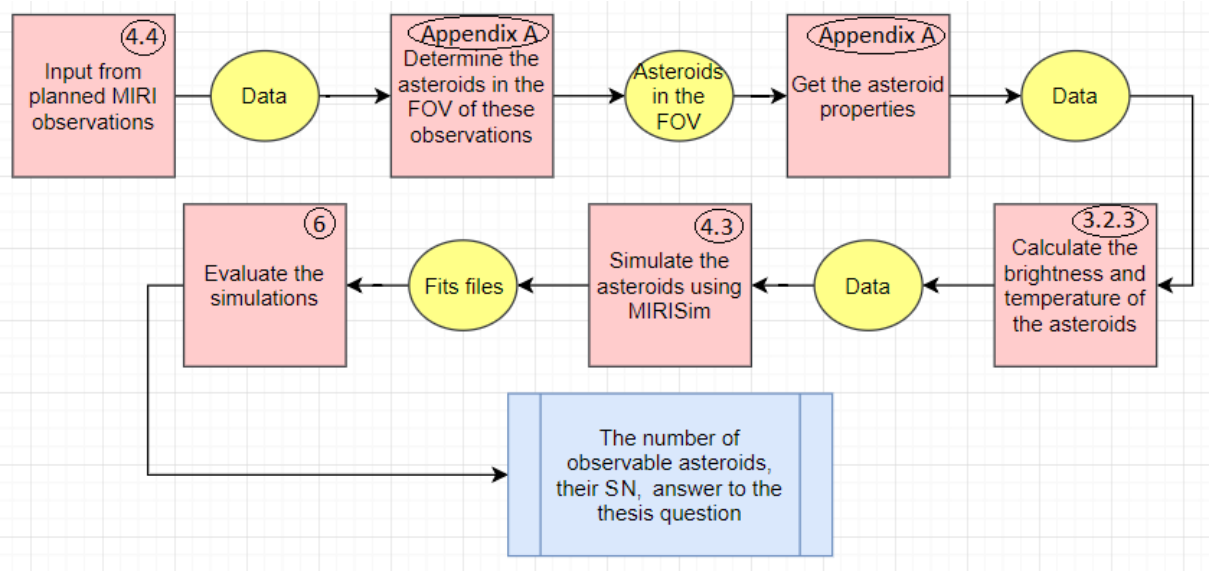

Figure 5.1: Flowchart of the simulation tool. The pink boxes are conceptual steps of the simulation process and each of them has Chapter number discussing them in more detail. The yellow circles represent the flow of the data between different steps and the blue box shows the desired output of this simulation, which is ultimately the answer to the thesis question; whether the use of MIRI's imager for serendipitous observation of asteroids would be useful.

5.2.1 Read an Input

First, to be able to use this tool, an input is needed. As mentioned in Chapter 4.4, an APT is used to be able to create realistic cases. The APT file, with real proposed observations, can be chosen from [13]. Each proposed observation consists of the date and time of the observation, the instrument and filter used, the specified direction (pointing) of the FOV in RA, DEC and the observation time, which consist of the number of frames, integrations and exposures. A python script which can read these data from the APT file is created.

5.2.2 Construction of an input Table

When the data are obtained from the APT file a python script which can create a MySQL table with these data is created. An example of an input table is shown in Figure 5.2.

```
+------------------+---------------------------+------------+--------+----------
-+-----------+-----------+-----------+-----------+-----------+-----------+------
-----+---------+---------------------------+-------------------------+
| OBS_id           | Observation_date          | Instrument | Mode   | Vertex1_1
 | Vertex1_2 | Vertex2_1 | Vertex2_2 | Vertex3_1 | Vertex3_2 | Vertex4_1 | Verte
x4_2 | Status  | Number_of_Asteroids_Detected | Time_Updated_UTC        |
+------------------+---------------------------+------------+--------+----------
-+-----------+-----------+-----------+-----------+-----------+-----------+------
-----+---------+---------------------------+-------------------------+
| 200624_000000_M  | 2020/06/24 00:00:00 UTC   | MIRI       | F1130W | 0 deg
 | 0.02 deg  | 52 arcsec | NULL      | NULL      | NULL      | NULL      | NULL
     | UPDATED |                           1 | 2018-07-22 16:22:36 UTC |
+------------------+---------------------------+------------+--------+----------
-+-----------+-----------+-----------+-----------+-----------+-----------+------
-----+---------+---------------------------+-------------------------+
```

Figure 5.2: Example of an input table with one proposed observation on the 24.6.2020. One asteroid has been found in this field of view.

The data which are saved are the observation date, instrument, mode, also called filter, and the FOV. The status and the number of asteroids detected are updated after the next function of this tool, Serendipitous asteroid detection tool, is run. In this observation, one known asteroid is expected to be in the FOV at this date and time.

Using the observation time, another input table is created, which consists of the same data, except the time. The time is as in the first table + observation time. This is useful to determine whether any other asteroids might appear in the FOV at the end of the observation time. This is not done for every second of the observation time, as this would only increase the time for running one simulation, and most of the asteroids are not fast enough to cross the whole FOV during the observation time, as can be seen in next Chapter.

5.2.3 Determination of the Asteroids in the Field of View

Having the input table(s), the next step of the tool can be taken. This uses the Serendipitous asteroid detection tool, more closely explained in Appendix A [5]. Basically, this opens the input table and uses the date and time and FOV to determine which currently known asteroids pass through. It takes the advantage of the Horizons database of asteroids [6] as well as the Asteroid & Comet Field-of-View Search Request [7], both are explained in Appendix A.

For the purpose of this thesis, the tool has been adjusted from Python 3 to Python 2. Also, one python package (callhorizons) is not maintained any more and therefore a new package (JPL Horizons Queries) has been used.

This Serendipitous asteroid detection tool creates a new MySQL table, which consists of all the asteroids in the FOV and their physical characteristics, such as their sky position (RA, DEC), the uncertainty in this position or their absolute magnitude. An example of this table can be seen in Figure 5.3.

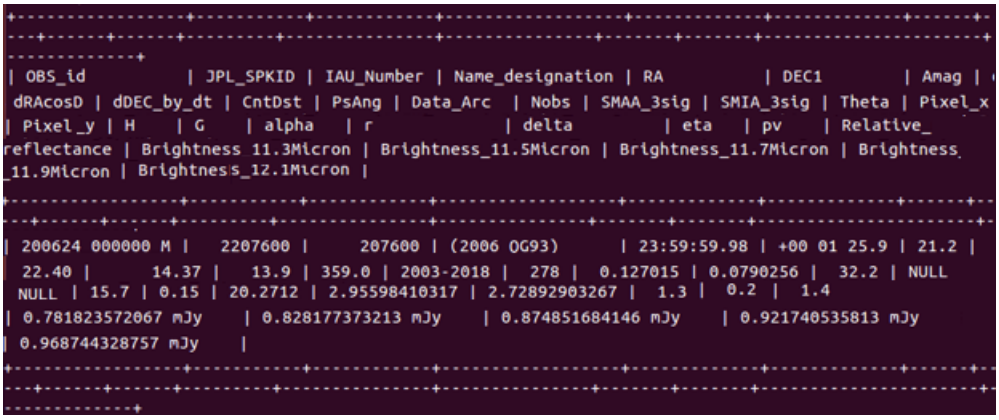

Figure 5.3: Example of an output table from one proposed observation on the 24.6.2020. One asteroid, found in this field of view, and its physical characteristics are inscribed in this table.

The brightness of the asteroid at different wavelengths can be also seen in Figure 5.3. This is the irradiance of the asteroid as received by MIRI. It consists both of the reflected brightness and the thermal brightness. For this calculation, the physical properties in the output table are used. Some extra parameters need to be specified for this estimation and they can be changed in one of the input files for the Serendipitous asteroid detection tool.

To calculate the reflected brightness, the relative reflectance of the asteroid is necessary, as it quantifies the ability of the surface of the asteroid to reflect radiant energy at different wavelengths. For this thesis a value of 1.5 is assumed and taken from an article estimating diameter for 100 000 Main Belt asteroids, shown in Figure 2.7 [4]. As it is expected that mostly NEOs and Main Belt asteroids will be detected

using the proposed method.

For the thermal brightness, the NEATM discussed in chapter 3.2.3 is used. To estimate the brightness, a beaming parameter is needed. This parameter expresses the effective surface temperature, however, in the case of NEATM, it is used as a calibration parameter. According to [41], a value of 1.2 would be the best fit for NEOs, however, for this tool, a value of 1 is used as the best assumption, due to the fact that the Main Belt asteroids are taken into account as well [4]. Another parameter needed for the estimation is albedo. This, as previously mentioned in chapter 3.2.3, has a very wide range of values and therefore a best and worst case scenarios should be taken into account. A starting point will be the value 0.2 for bright asteroids and 0.06 for dark asteroids [4].

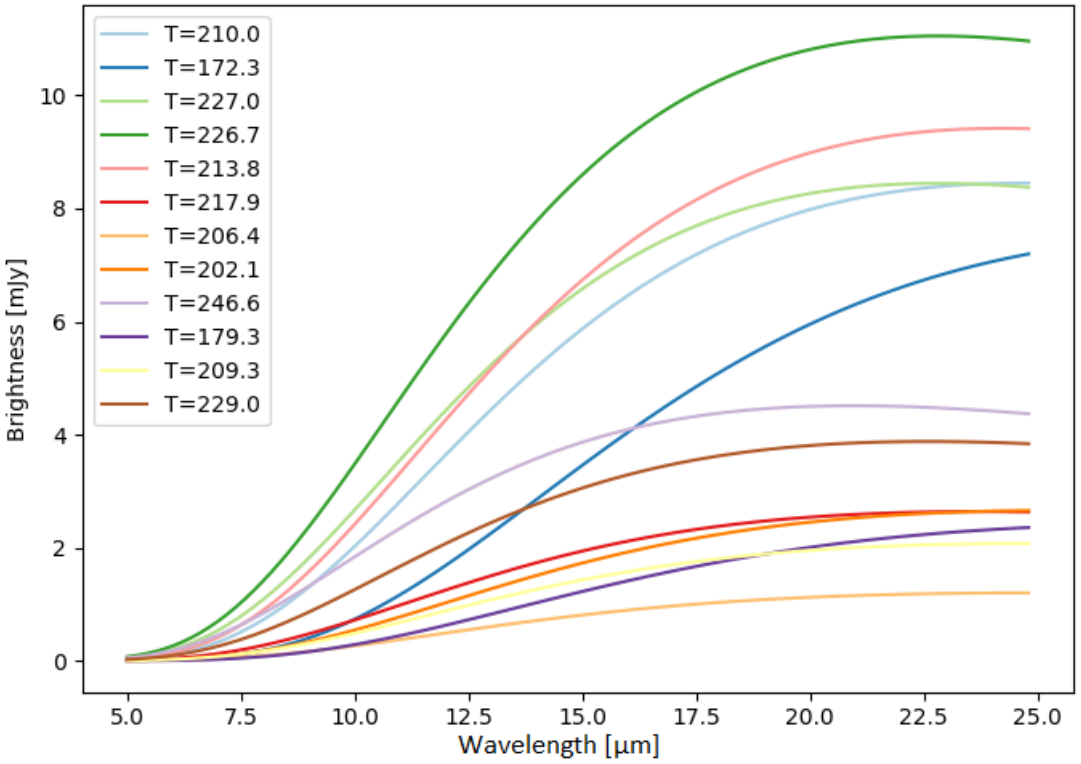

Figure 5.4: Brightness of 12 asteroids, as would be seen by MIRI, at different wavelengths calculated using the NEATM model. The difference in slopes is due to different temperatures as well as the distances from the Sun and the telescope respectively. For example, the two green lines peak at around the same wavelength (22.8 micron) due to the similar temperatures, however, they have different brightness values due to their different absolute magnitudes. On the other hand, the dark blue line (172.3 K) peaks at much longer wavelength due to its lower temperature, but still has a quite high brightness due to its brighter absolute magnitude.

Using this NEATM model, brightness, as would be detected from MIRI when in orbit, for a sample of 79 asteroids, which appear in the field of view of the MIRI's imager at different times, has been evaluated and both the thermal and the reflected brightness, has been plotted in Figure 5.4 for chosen 12. The estimated temperature for each of them, as explained in the next step, is specified. The highest flux does not necessarily mean the warmest asteroid, as in this also the absolute magnitude of the asteroid and the distance between the asteroid and the Sun and the instrument are taken into account. This means that for the same temperature the peak of the curve is at the same wavelength, but the brightness can be lower or higher due to the absolute magnitude or the distances between the objects.

5.2.4 Estimation of the Temperature of the Asteroid

To be able to simulate an asteroid, its temperature has to be determined. This can be done using the earlier calculated brightnesses at different wavelengths from the previous step. An asteroid can be approximated as a black body, as it gives reasonably good estimates, and therefore the Planck's law can be used.

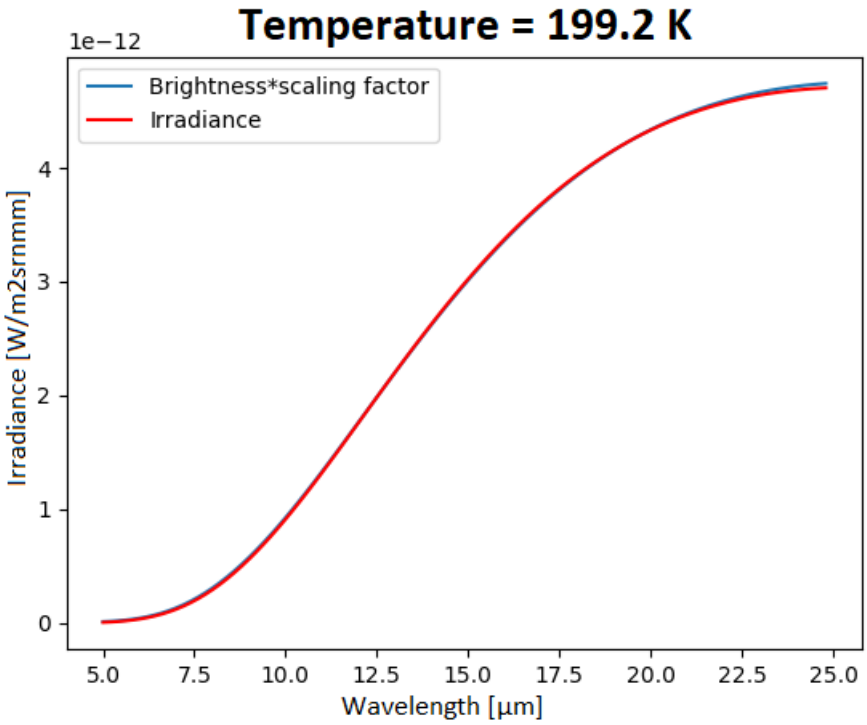

Figure 5.5: An example of the best temperature fit. It is 199.2 K for asteroid (2006 QG93), the red line is the irradiance calculated by the Planck's law and the blue line is the estimated brightness*scaling factor. This asteroid is at a distance of 2.96 AU from the Sun and 2.73 AU from the telescope and has an albedo of 0.2 and H of 15.7.

This law describes the thermal equilibrium of an body at a temperature T by this equation [42]:

$$B_v(v,T) = \frac{2hv^3}{c^2}\frac{1}{e^{\frac{hv}{k_B T}} - 1} \tag{5.1}$$

where B_v is the spectral radiance of the body, v is the frequency, T is temperature of the body, h is Planck constant, c is the speed of light in the medium, and k_B is the Boltzmann constant.

The spectral radiance expresses the amount of energy emitted as radiation at different frequencies. As the radiation of the asteroid at different frequencies is known a chi-square fitting [51] is used to determine the best temperature fit.

$$\chi^2(a) = \sum_{i=1}^{N}(\frac{y_i - ax_i}{\sigma^2})^2 \tag{5.2}$$

where χ^2 needs to be minimized to approximate the best fit temperature of the asteroid, N is the number of data points, y is the calculated spectral radiance from the Planck's law, a is the scaling factor and x is the estimated brightness at different frequencies. Differentiating the equation w.r.t. the best scaling factor, the best temperature fit can be found, as shown in Figure 5.5.

5.2.5 Simulation of the Asteroids as detected by MIRI

Simulation of the asteroids is the last step of the tool. It uses all the data from the previous functions and the imager mode of MIRISim, Chapter 4.3. MIRISim can simulate the data produced by the MIRI's imager. It can create a FITS file image showing the sky and the asteroids in the view.

To be able to use MIRISim, multiple input files need to be specified to create the simulation. There are three input files in total, however, only two of them will be adjusted, as the third file is used for testing and not general use.

The first file is the scene.ini, where the scene has to be specified. A scene can consist of three components; the background emission, a point source or a galaxy. For the purpose of this thesis, only the background emission and the point source are specified. The background emission is chosen as high to establish the worst case scenario for the asteroid visibility.

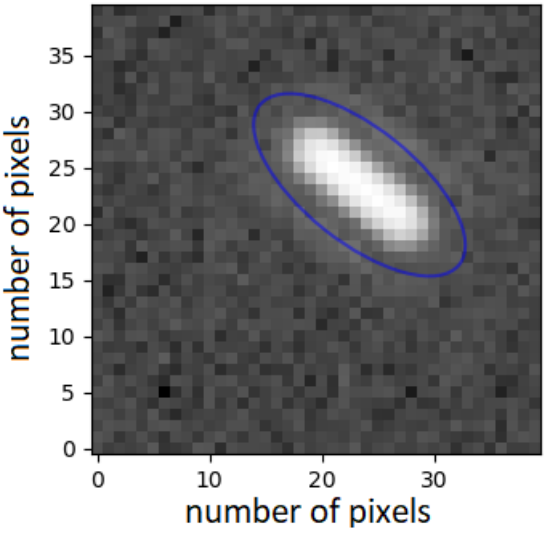

Figure 5.6: Example of a simulated asteroid (2006 QG93) moving through the FOV. Zoomed in view on the asteroid streak, in the blue oval. Estimated temperature of 199.2 K, with distances of 2.96 AU from the Sun and 2.73 AU from the telescope, and albedo of 0.2 on the 24.06.2020 at 00:00:00 UTC for an integration time of 155.4 s.

The point source of an asteroid is estimated as a black body [8], with its temperature and reference brightness and wavelength. From the output table, all the asteroids in the FOV are specified in this file. Using the velocity and direction of the asteroid's trajectory, the asteroid's movement through the FOV can be estimated. Then, the asteroid can be simulated as a streak of light by simulating multiple point sources next to each other, each with the brightness equal to the brightness of the asteroid divided by the total number of point sources to account for the movement. Zoomed in simulated image of such a streak of light can be seen in Figure 5.6. It can be seen that in this case, the asteroid is visible by MIRI's imager.

5.2.6 Calculation of the Signal to Noise Ratio of the Asteroids

To quantify how visible an asteroid is in the field of view of the instrument, signal to noise ratio (SN) is calculated. This is the ratio of the brightness emitted by the asteroid w.r.t the noise of the image. The calculation of the SN is done as follows [52], Figure 5.7:

1. The signal sum of the asteroid streak and the number of pixels is noted.
2. The average value of a pixel in this streak is calculated. $Signal_{sum}/N_{pixels} = S_{pixel}$

3. The background signal over the number of pixels is measured. An object free place close to the asteroid is chosen.
4. The average background signal value is calculated. $Signal_{Bsum}/N_{pixels} = S_{Bpixel}$
5. Signal of an asteroid pixel. $S_{Apixel} = S_{pixel} - S_{Bpixel}$
6. The background noise is the standard deviation (stddev) over the number of pixels over the background chosen in step 3.
7. The SN per pixel is $S_{Apixel}/stddev = SN_{pixel}$
8. The SN for the whole asteroid streak is $SN = SN_{pixel}\sqrt{N_{pixel}}$

If the value of SN is bigger than 50, the asteroid is clearly visible. Values smaller than 10 are very weak and smaller than 3 are uncertain. The area chosen for the background signal should be close to the asteroid streak, as to get the closest value to the background noise at the streak. However, checking the area around the asteroid streak shows different values for the background signal. Therefore an error bar for the SN, representing the smallest and highest possible value for a specified filter, is introduced.

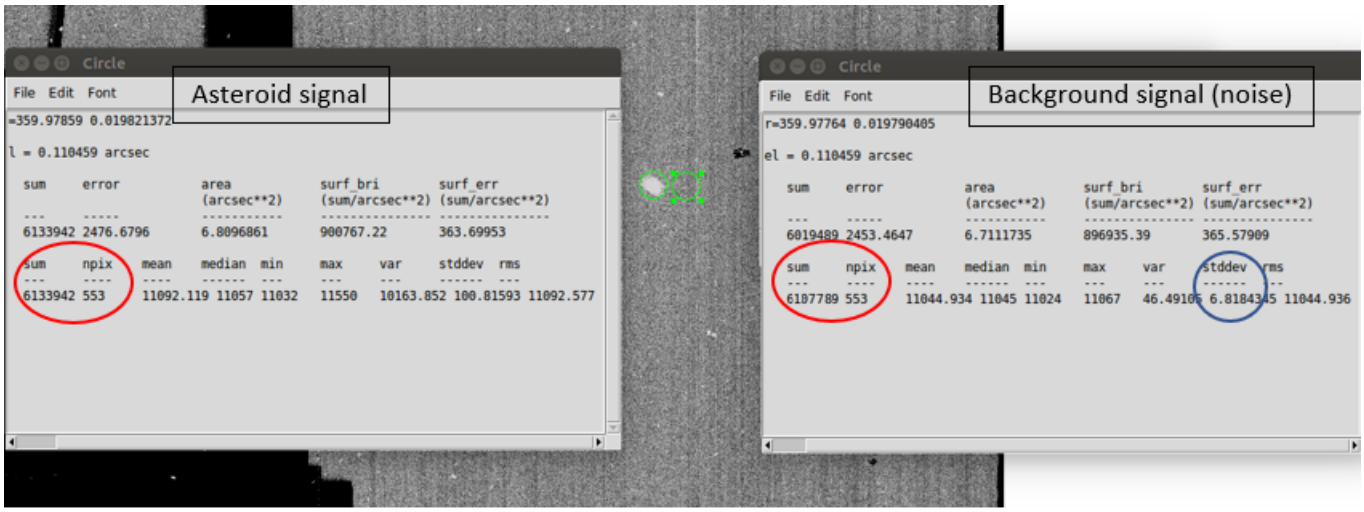

Figure 5.7: Example of a simulated asteroid and the signal and noise of the pixels. Asteroid streak of 553 pixels and signal of 6133942, has the average value of a pixel 11092.12. The background signal sum for 553 pixels is 6107789 and the average value for a pixel is 11044.82. The signal of an asteroid pixel is 47.29. The background noise, standard deviation (stddev), is 6.81. So SN is 6.94. The SN of the whole asteroid streak is 163.11. This would mean a clearly visible asteroid, as can be seen.

5.3 Tool Limitations

To be able to simulate the asteroids in a realistic way, and yet not overly complicated, some simplifications have been made. These simplifications and assumptions are summarized and explained in the list below:

- The FOV is specified as a circle 10 arcsec bigger than would be the smallest circle overlapping the FOV of the MIRI's imager. This is to catch also the asteroids which might come in the FOV of the imager during the observation time.
- The actual position of an asteroid might be different from what is expected in this tool. This is because of the uncertainties in the asteroid orbits. Also, many new, yet undetected, asteroids might appear in the field of view.
- The FOV pointing taken from the APT file (GTO 1282) is actually for the MRS and not the imager, which is an offset of a couple of arcseconds, Chapter 4. However, as the launch date of the JWST still might change, the exact position of the JWST at a specified date and time is also not

known. Therefore the actual pointing at that date might still be different than the one given in the APT file. Therefore simplifying the code by not taking the offset into account does not make the case less realistic, it would only make it more complicated.

- The roll angle of the instrument is not taken into account. Reasoning as above.
- The values for relative reflectance, 1.5, beaming parameter, 1, emissivity, 0.9, and albedo, 0.2 and 0.06, are assumed as explained in the previous chapters.
- Stars and galaxies or other bright bodies which would overshadow the asteroids are neglected.
- Background emission is taken as high in MIRISim input file.
- Asteroid is approximated as a black body because in MIRISim it is convenient to use black body approximation [8] and it gives a reasonably good estimate.
- If the asteroid does not appear in the FOV at the beginning of the observation time or at the end it is neglected, as the check for asteroids in the FOV is not done for each second of the observation. This means that the Serendipitous observation tool only determines if there are any asteroids in the field of view at the beginning of the observation time and at the end. This is not a problem as most of the asteroids do not move fast enough to pass the whole field of view during the observation time (as can be also seen in the next chapter, the same asteroid is found at the beginning and at the end of an observation).
- MIRISim is consistent with the sensitivity model of MIRI, however, it should not replace the JWST exposure time calculator. Nevertheless, for the purpose of this thesis, this kind of simulator is good enough, as the MIRISim has been verified by the JWST exposure time calculator [50].

5.4 Tool Verification

Every tool needs to be verified, and this one is no exception. Each part of the code is verified by itself and then the whole tool is run and verified as well. The different tests are done for the tool:

- Determine whether the data from the APT file are inputted properly. Compare the data in the APT file with the data saved by Python.
- Determine whether the created table in MySQL contains all the data from the APT file.
- Determine whether the Serendipitous asteroid detection tool works as expected, i.e. if proper tables are created, if all the data are saved as expected and the brightness is properly estimated.
- Check, whether the Serendipitous asteroid tool is properly integrated with the table created in MySQL, i.e. if it can open the table without problems and use the data to create tables with the detectable asteroids.
- Check whether the tables created by the Serendipitous asteroid tool can be used without a problem.
- Determine if the estimation of the asteroid temperature works for each asteroid, even if there are more asteroids in the FOV, and if the temperature is realistic.
- Determine if these data are properly inputted into the MIRISim.
- Determine whether the simulated output is as expected, i.e. if the asteroid appears as bright as expected and at the expected part of the simulated picture. Also, the header of the simulated file is checked for the consistency.
- Determine whether the signal to noise ratio of a point source asteroid is consistent with the signal to noise ratio of an asteroid modelled as a streak of light.
- Determine whether the calculated brightness of the asteroid is consistent with the sensitivity of the MIRI.
- Check whether the whole tool runs and if the final output is as expected.

Overall the verification was deemed successful.

6. The Simulation of the Observability of the known Asteroids

To be able to answer the main question of this thesis, the possibility of using MIRI to serendipitously observe asteroids, a simulation is performed. In this simulation, the currently known asteroids and their estimated characteristics and positions are used to determine whether they are bright enough to be detected by the MIRI's imager. In this chapter, this simulation and its results are shown.

6.1 Input Parameters for the Simulation

To simulate realistic images, proposed observations from [13] for JWST are used. The proposal chosen for this thesis is GTO 1282. This is a proposal from scientists, who worked on the instrument. The title of this proposal is: "MIRI EC Protoplanetary and Debris Disks Survey" and it focuses on the study of proplanetary disks. The allocated time for this proposal is 112.6 hours, but the actual science time is only 44.64 hours. This difference is the time used for other things the instrument needs to do, such as detector readout, detector resets, turning filter wheels or moving the telescope between positions. This proposal targets 50 different objects, e.g. stars, brown dwarfs and young debris disks with the use of MIRI and NIRCam. These are relatively bright sources for MIRI standards and the exposure times for these observations are relatively short. This is acceptable for the purpose of this thesis as the signal to noise increases for longer exposure times, i.e. it scales with the $\sqrt{t}$ [52].

The input for this simulation is taken from this APT file, as mentioned before. This consists of multiple observations focusing at different parts of the sky, as well as different exposure times and possible observation dates, as can be seen in Table 6.1. A total of 55 different proposed observations are given in this file, where 5 of them are not using MIRI, but NIRCam. All the simulations are done with the same filter, i.e. F1280W. As this is the filter chosen in the APT file.

Table 6.1: Different observations taken from the GTO 1282 [13] file of proposed observations. RA and DEC are given in J2000 Coordinates and the possible dates are the earliest dates when the observation could take place (launch was scheduled in 2020) according to the planner in the APT tool. Obs. N stands for observation number within the proposal.

Obs. N	RA	DEC	Exposure time [s]	Possible dates
1	04 34 55.4240	+24 28 53.16	488.4	17.1.2020 - 1.3.2020
17	16 48 45.6380	-14 16 35.90	488.4	26.2.2020 - 17.4.2020
20	11 01 54.100	-34 41 56.50	183.153	19.12.2019 - 23.2.2020
24	13 00 55.3200	-77 10 22.20	1098.916	13.2.2020 - 6.9.2020
54	15 15 48.4400	-37 09 16.00	610.509	10.2.2020 - 3.4.2020

From these files, the integration number, number of frames and number of exposures is taken as well. The observation date and time is taken to be every half a day for the possible observation dates. This random choice can be taken due to the fact that the actual time of these proposed observations is not yet known, likewise, the date of the launch of the JWST might still change.

6.2 Assumptions and Simplifications

To simulate the known asteroids using the previously explained simulation tool, the assumptions and simplifications should be mentioned. These are the simplifications taken with input values and parameters and not the assumptions used in the tool itself.

1. It is assumed that the asteroids taken from JPL HORIZONS System [6] and their properties are accurate. This means that the error in them, such as the error in their position or their absolute magnitude, is not added in the overall error of this simulation. This means that the asteroids, which are simulated here might not actually be in the field of view of the imager at the given time, or their brightness might be different.
2. The values 1.5 for relative reflectance, 1 for beaming parameter and 0.9 for the emissivity of the asteroids are assumed as discussed in the previous chapters.

3. The value for albedo is taken to be 0.2, to simulate bright asteroids and 0.06 to simulate dark asteroids, as shown in Figure 2.5. This means that each observation is simulated twice, once for bright and once for dark asteroids.

4. The observations used in this thesis are taken from the APT file (GTO 1282) from [13]. These proposed observations are representable of the possible observations performed by MIRI. This file consists of observations into different parts of the sky as well as different observation times. This makes this research more realistic.

5. The launch date of JWST in the GTO 1282 at the time of this thesis was 2020, therefore the possible observations dates are in the year 2020.

6. The launch date of JWST, to determine the position and pointing of the instrument at a specified time in the Asteroid & Comet Field-of-View Search Request, is assumed to be October 2018

7. The simulations have different background noise at different positions of the image. Nevertheless, this difference has been evaluated and the biggest error of 15% has been found. This means that the sensitivity of the imager is approximately the same everywhere in the FOV. To calculate the signal to noise ratio, explained in Section 5.2.6, a local value (close to the asteroid) is taken to determine the most precise estimation.

6.3 Results

Using these inputs the simulation of asteroids' signatures in the MIRI's imager FOV is performed. The results of this simulation are shown here.

6.3.1 The Probability of finding Asteroids in the FOV

The simulation specifies the pointing of the instrument and then checks for the asteroids in this FOV at that specified time and date. As mentioned the time for the observations has been chosen within the possible observation period as shown in Table 6.1. The tool checks the FOV every half a day for a few days for each of the directions. As checking every second would be redundant.

From the total of 1153 checks, only 87 resulted in possible currently known asteroids in the FOV. The highest number of asteroids in a given FOV was 2. For most of the cases, only one known asteroid appeared in the view. This gives a 7% chance that there is an asteroid in the FOV at any given time. Overall the chance of detecting an asteroid for different proposed observations is more less the same, with some directions more favourable than others, such as the ones pointing toward the ecliptic. As most of asteroids orbit close to the ecliptic, it is reasonable that looking towards the ecliptic plane would result in more of them in the FOV than looking in other directions.

6.3.2 Number of Asteroids detected

These 87 cases with possible known asteroids in the FOV are simulated by MIRISim. Each is simulated two times, for a different albedo, a bright (0.2) and a dark one (0.06). For some of these cases, the asteroid is not actually in the FOV of the imager, as the FOV given to determine whether there are any asteroids is bigger than the real FOV of the MIRI's imager. Therefore from this 87 cases, only 47 resulted in actual asteroids in the FOV of the imager. This gives only 4.1% chance of an asteroid appearing in the FOV at a specified moment.

Evaluating the simulated images, as shown in the next section, shows that the total number of visible asteroids in the FOV w.r.t the number of asteroids expected to be there is very high. The number of simulated asteroids was 48, as only one FOV has more than one asteroid appearing in it. From these 48 asteroids, only 1 was not bright enough for MIRI's imager's sensitivity neither with the albedo of 0.2 or 0.06. Another asteroid was bright enough with an albedo of 0.06 but too dim with an albedo of 0.2. This means that the ratio of visible w.r.t expected asteroids is 96.9%. The undetected asteroid has the absolute magnitude of 24.8, which is the highest of all the simulated asteroids. Only 4700 currently known asteroids have higher absolute magnitude than that, as this are very small asteroid between 30-60 m in diameter. This is only a 0.6% of the total number of 790 150 detected asteroids so far [6]. The asteroid with the second highest absolute magnitude, 20.2, is visible in the FOV. The other

undetected asteroid is just leaving the FOV, and this fact could have made its visibility more problematic.

To estimate the number of known asteroids, which can be detected during the lifetime of JWST, following assumptions are taken [13] [53]:

- A 5-year mission life (42750 hours).
- Science hours, the time when the instrument is observing, are 65% of the total time. As there are times when the instruments are not taking data, e.g. setup of the instrument, pointing, downlink.
- MIRI is working 25% of the science time. The other instruments are working the rest of the time.
- MIRIM is working and gaining data, which could be used for asteroid detection, 75% of MIRI's working time.
- There is a 4.1% chance of an asteroid being in the FOV of the instrument.
- There is 96.9% chance of detection of the asteroid in the FOV.
- 75% of the asteroids will appear more than once and 1.6% will appear more than twice [6].

The estimated number of the known detected asteroids during the JWST life is then 183 314. This number of detected asteroids could be much higher when the telescope is pointing towards the parts of the skies highly populated with asteroids. The number of yet undetected asteroids is also unknown but could increase the value of the detected asteroids.

6.3.3 Limits on the Detection of an Asteroid

As seen from the simulations, some asteroids might be too dim to be detected by the MIRI's imager. There are multiple possibilities for such a result. The elements, which could have an impact on the visibility of the asteroid are:

- The size of the asteroid.
- The albedo of the asteroid.
- The distance between the Sun and the asteroid.
- The distance between the instrument and the asteroid.
- The absolute magnitude of the asteroid.
- The temperature of the asteroid.
- The velocity of the asteroid.
- The observation time of the observation.
- The position of the asteroid within the FOV, i.e. when the asteroid is on the border of the FOV the detection might be lower.

According to this, some limits on the detection of asteroids had been determined. This is done by running the simulation multiple times for similar cases, with changing some of the input values consistently. Figure 6.1 shows a plot of SN w.r.t. the Sun-asteroid distance. Eight different lines are shown on the plot, and for each of them, one value is altered compared to the rest. The different variables are the instrument-asteroid distance (d), the albedo (pv) and the absolute magnitude of the asteroid (H).

It is clear from Figure 6.1 that, as expected, the closer the asteroid is to the instrument and the Sun, the higher the SN. Also, the lower the albedo, the higher the SN, which is as expected in infrared observations as well. The absolute magnitude of 22 is too dim to be detected if the asteroid is further than 3 AU from the Sun and the instrument. The absolute magnitude of 22 would be an asteroid of size between 100-250 km in diameter. Therefore it can be concluded that all the asteroids bigger than 250 km should be detectable by MIRIM if the distances between the Sun, the asteroid and the instrument are less than

3 AU. Depending on these distances, smaller asteroids might be detected as well.

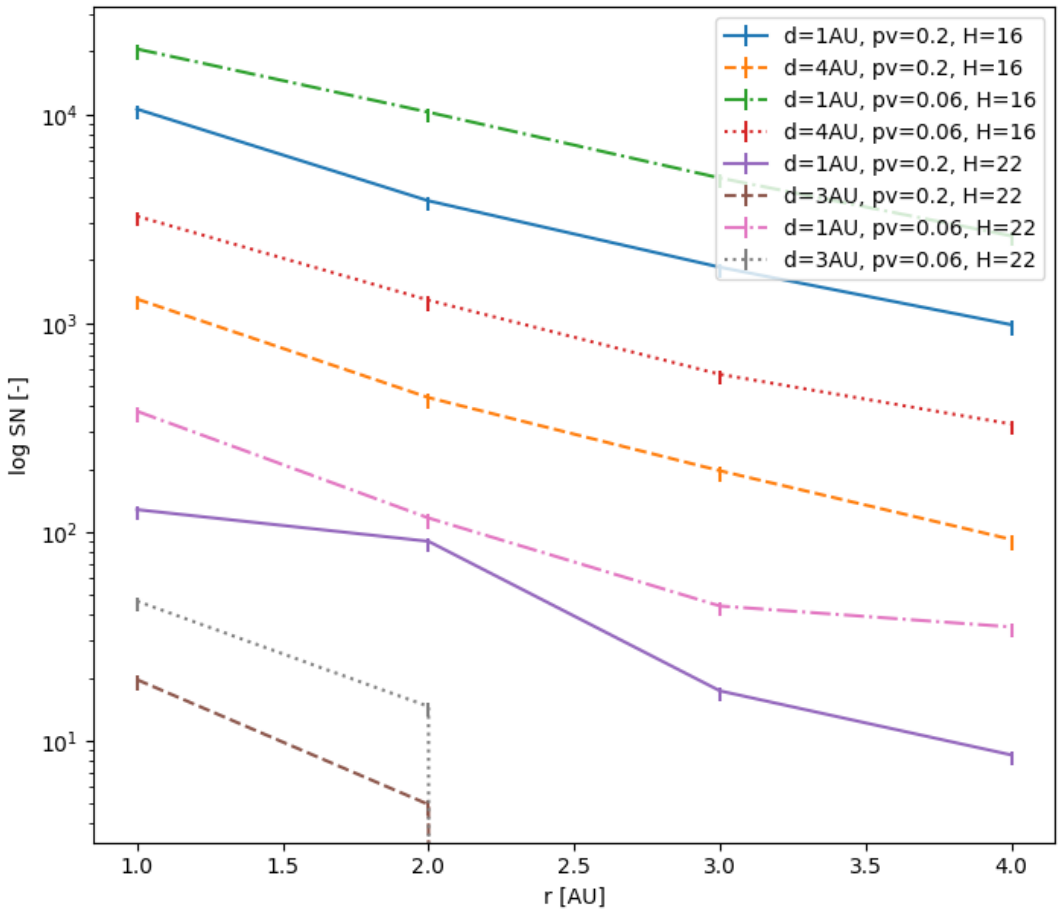

Figure 6.1: Signal to noise (SN) ratio estimations for different consistent inputs and exposure time of 488.4 s. Four variables are changed, the Sun-asteroid distance (r), the telescope-asteroid distance (d), the albedo (pv) and the absolute magnitude (H).

Knowing the minimum size of an asteroid detectable by the imager, an estimate for the number of yet undetected asteroids could be made. Previous assumptions, plus a few new ones, are taken to calculate this value:

- According to Table 2.1, there are 4 000 000 asteroids bigger than 300 m in diameter.
- Ratio of asteroids w.r.t known asteroids is 0.20.
- The probability of an asteroid being in the FOV increases with this ratio to 20.6%

This gives an estimate of 916 570 asteroids to be detected by the MIRI's imager. From which 733 256 are yet unknown asteroids.

6.3.4 Simulated Images

The simulations created using the simulation tool are evaluated. This consists of reviewing the images, the FITS files created by MIRISim, and determining whether an asteroid signature is present at the expected pixel position. The expected pixel position within the simulation is determined from the input position of the asteroid (RA, DEC). However, in reality, the asteroid position has an uncertainty and therefore, the position of an asteroid, when actually using MIRI, could be different. From this, the signal to noise ratio for each asteroid is calculated. Each simulation has a random noise added by the simulator,

as well as some cosmic ray hits and this can show up on the images as very small bright sources (dots), as can be seen in the Figures below. It is also important to assess the last integration and frame of the FITS file, as this is the image after the whole observation.

Depending on the properties of the asteroid, as well as the specifications for the observation, different kinds of asteroid streaks are possible. These depend on the apparent motion of the asteroid w.r.t the instrument. Faster apparent motion leads to longer streaks, the same as longer exposure time. The apparent motion is the movement of the asteroid the instrument sees as it moves in its orbit. Different cases, which could be present:

- The apparent motion of the asteroid is too small for the pixel resolution of the instrument to detect a movement, and the asteroid appears as a point source.
- Asteroid moves inside the FOV.
- Asteroid moves out of the FOV.
- The whole streak of the asteroid is in the FOV.

Saturation of the instrument would be undesirable. Nevertheless, it is highly unlikely for an asteroid to be bright enough to saturate the instrument. Comparing with Table 4.1, for filter F1280W, used in these simulations, the brightness would have to be higher than 15 mJy. Even for asteroids, which have brightness more than 15 mJy, the signal will get redistributed over the moving streak, as the asteroids have apparent motion w.r.t. the instrument. Also, none of the asteroids simulated has saturated the instrument.

Table 6.2 shows the data of the asteroids detected in the simulated images presented in this report. Their characteristics, e.g. name, albedo, H, exposure time of the observation, estimated temperature, apparent motion, SN and estimated diameter, are shown. It can be seen that the asteroid with the highest apparent motion is also the one with the longest streak, Figure 6.5. The asteroid, which looks like it has not moved at all, Figure 6.2, has an apparent motion of 0.0054 arc/s. However, its exposure time is short (49.95 s) and the asteroid moves only 0.27 arcsec, which results in the only one-pixel source. So even though the asteroid does move w.r.t. the instrument, the resolution is not high enough to see this small move. The last asteroid, simulated for two albedo values, has a bigger diameter for the higher temperature. This is as expected from Figure 6.7 as well, where the asteroid simulated with the lower albedo is brighter than the other one. The biggest diameter out of these, 4.49 km, has the asteroid (2001 UY107), which is also one of the brightest ones, as seen in Figure 6.6.

Table 6.2: Some of the simulated asteroids, shown in Figures below, and some of their characteristics are shown here. Diameter (D) is calculated using Equation 3.6. Albedo is the value used in the simulation and apparent motion is calculated from the position (RA,DEC) at the beginning and end of the exposure.

Name or designation	**Albedo [-]**	**H [-]**	**Exposure time [s]**	**Estimated T [K]**	**Apparent motion [arcsec/s]**	**SN ± 11% [-]**	**Estimated D ± 15% [km]**
2008 UN310	0.06	15.7	49.95	204.7	0.0054	1602.75	2.85
2004 TC367	0.06	18.3	488.4	216.8	0.0122	218.43	1.72
2014 QR309	0.2	16.9	488.4	204	0.0098	203.20	1.56
2009 FK26	0.2	17.7	1098.9	234.2	0.0172	238.90	2.24
2006 TF32	0.06	16.8	1098.9	191.1	0.0080	325.20	1.676
2001 UY107	0.06	15.1	1098.9	200.4	0.0095	1419.77	4.89
2009 SW261	0.06	16.6	427.35	201	0.0046	805.62	2.84
2009 SW261	0.2	16.6	427.35	198.3	0.0046	448.59	1.79

Each of the shown simulated images shows the rectangular field of view of the imager on the right side of the image. On the left, the black part (black structure) is another mode of MIRI, coronagraphy, as seen in Figure 4.4, which functionality is not simulated by MIRISim, yet its part of the simulated image from MIRISim. Nevertheless, one part of the coronagraphy is simulated and shows asteroids in the squared field of view on the top left.

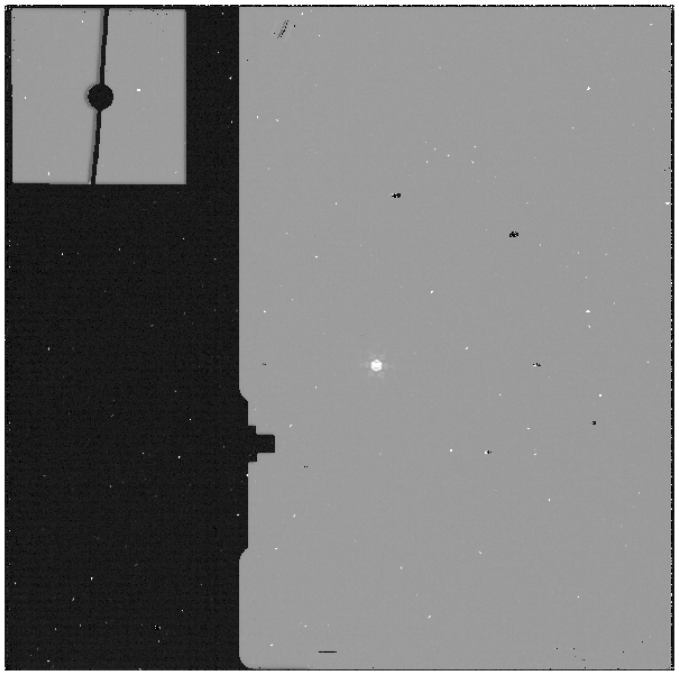

Figure 6.2: Asteroid (2008 UN310), the white circle, is shown in the FOV of the MIRI's imager on the 16.02.2020 at 00:00:00 UTC. The apparent motion of the asteroid is 0.0054 arc/s. The estimated temperature of this asteroid is 204.7 K, the albedo is 0.06 and the exposure time is 49.95 seconds. The black part (structure) of the image is the coronagraphy, as can be seen in Figure 4.4.

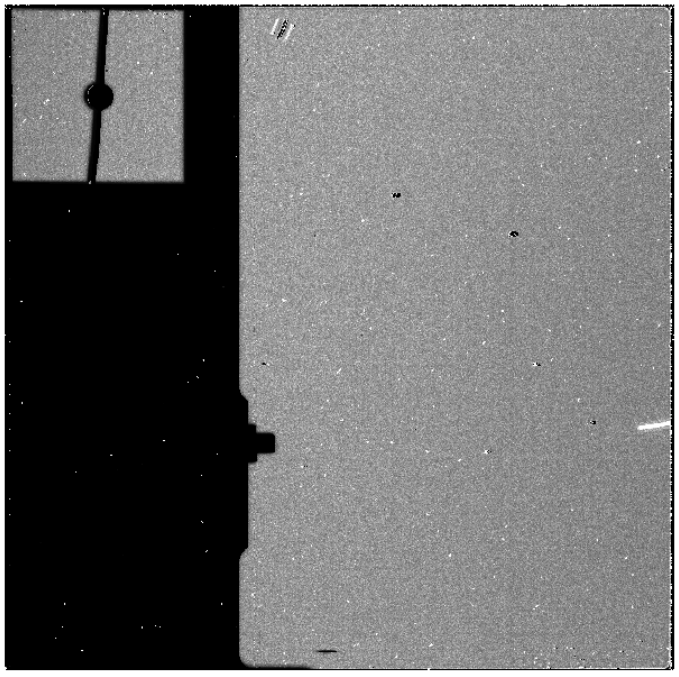

Figure 6.3: Asteroid (2004 TC367), the streak on the left of the image, is shown in the FOV of the MIRI's imager on the 13.02.2020 at 00:00:00 UTC. The estimated temperature of this asteroid is 216.8 K, the albedo is 0.06 and the exposure time is 488.4 seconds. The black part (structure) of the image is the coronagraphy, as can be seen in Figure 4.4.

The first kind of streak, shown in Figure 6.2, is not very frequent, as the apparent motion of the asteroid w.r.t. the instrument would have to be zero or very small. Nevertheless, for very short exposure times (<50 seconds), this could be achieved, as for a short exposure time, the asteroid could move so little, that the resolution of the instrument will not be able to see it as more than a point source. This kind of signature has a high signal, however, could be confused with a star, as it is not moving. In this Figure 6.2, the exposure was just 49.95 seconds and the signal to noise ratio was calculated to be 1602.75 ± 11%. This is a strong signal, as can be also seen from the image.

The second and third kind looks the same on a simulated image, the streak trails off outside of the FOV, as shown in Figure 6.3. The fact that the asteroid is at the rim of the FOV has an impact on the detectability of the asteroid, as the sensitivity and the noise at the edge can be different from the rest. The calculated signal to noise ratio of this asteroid is 218.43 ± 11%. Overall 10 such asteroids (coming inside of or leaving the FOV) have been detected during this thesis.

The last kind, shown in Figure 6.4 and 6.5, is the most frequent in the results of these simulations. It is also the preferred kind, as seeing the whole streak can give the most information, i.e. the velocity of the asteroid. From the length of the streak, the apparent motion of the asteroid can be calculated and therefore the velocity. Two simulations are shown, for this kind of streak and the signal to noise ratio calculated for both asteroids, Figure 6.4 and 6.5, is 203.20 ± 11% and 238.90 ± 11% respectively.

The difference between Figure 6.4 and 6.5 is that the second Figure 6.5 has a much longer streak, the longest from all the simulations. This is due to its high apparent motion, as well as longer exposure time. A longer streak means an asteroid with higher apparent motion and a higher chance that the asteroid might be too dim to detect. In the extreme cases, the asteroid could pass the whole FOV during the exposure time. In such a case, there would be a high chance that the asteroid is not bright enough to be detected by the imager.

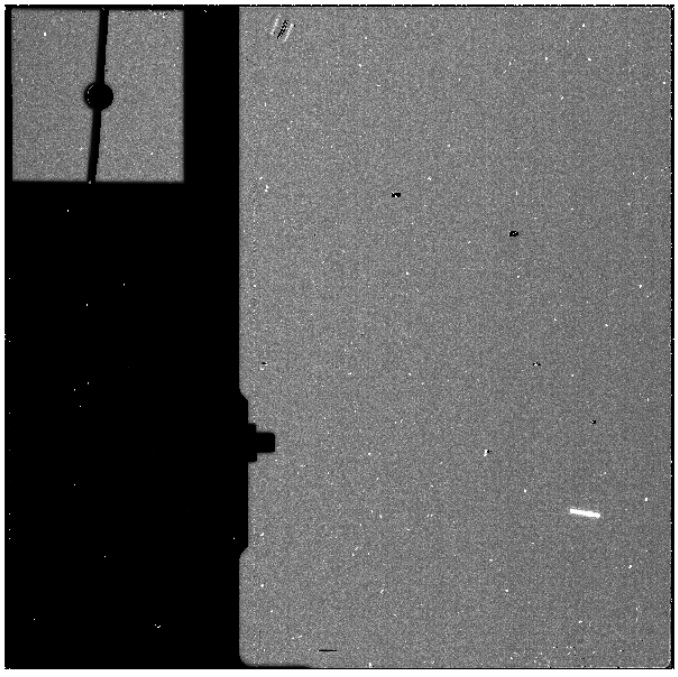

Figure 6.4: Asteroid (2014 QR309), the asteroid streak on the left side, is shown in the FOV of the MIRI's imager on the 08.03.2020 at 00:00:00 UTC. The estimated temperature of this asteroid is 204 K, the albedo is 0.2, the exposure time is 488.4 seconds. The black part (structure) of the image is the coronagraphy, as can be seen in Figure 4.4.

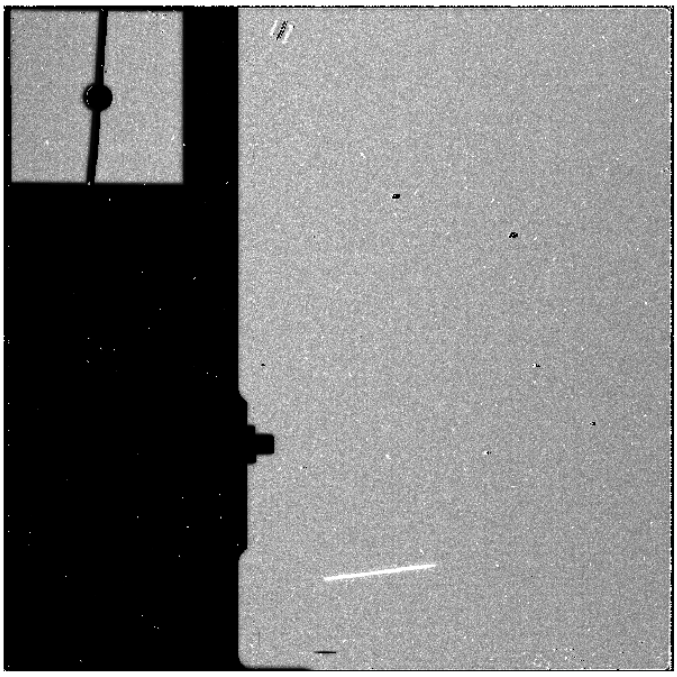

Figure 6.5: Asteroid (2009 FK26), the asteroid streak at the bottom, is shown in the FOV of the MIRI's imager on the 12.02.2020 at 12:00:00 UTC. The estimated temperature of this asteroid is 234.2 K, the albedo is 0.2, the exposure time is 1098.9 seconds. The black part (structure) of the image is the coronagraphy, as can be seen in Figure 4.4.

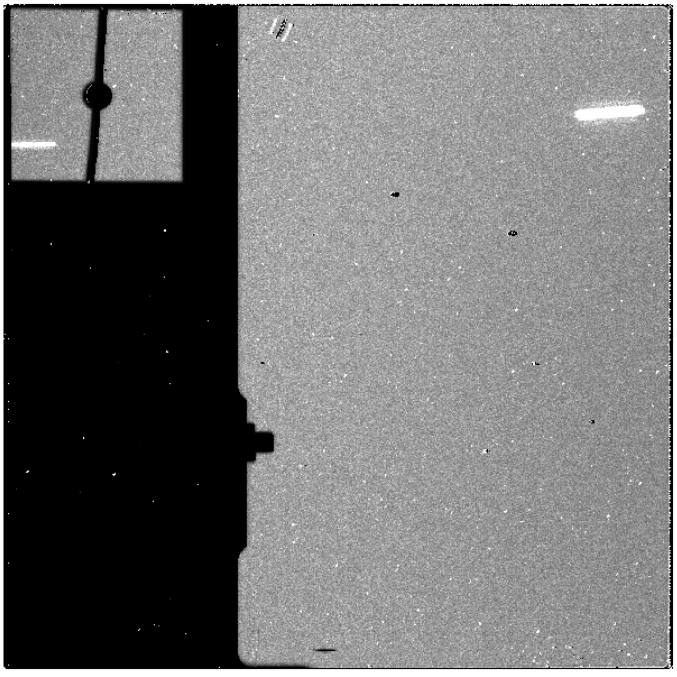

Figure 6.6: The only FOV with two asteroids, asteroid (2006 TF32), on the left, and asteroid (2001 UY107) on the right of the simulated image on the 16.02.2020 at 00:00:00 UTC. The estimated temperature of 2006 TF32 is 191.1 K and for 2001 UY107, the temperature is 200.4. The albedo is 0.06 for both of them and the exposure time is 1098.9 seconds. The black part (structure) of the image is the coronagraphy, as can be seen in Figure 4.4.

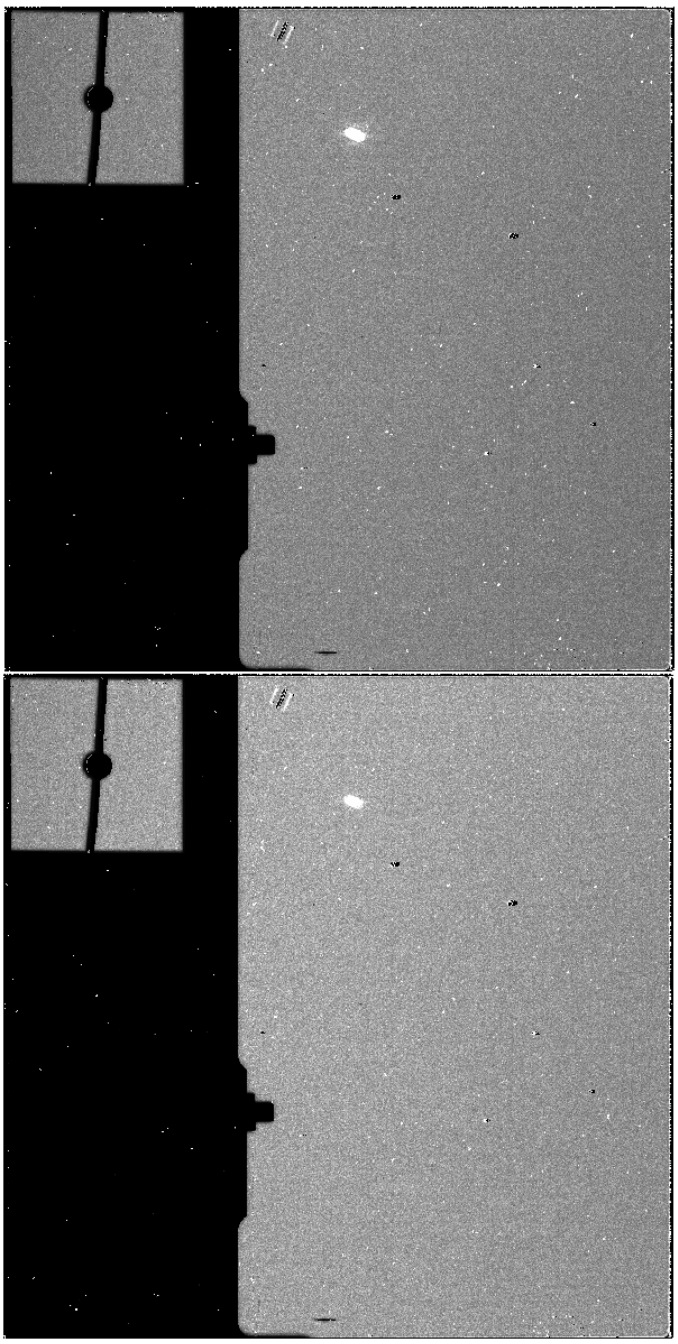

Figure 6.7: Asteroid (2009 SW261) is shown in the FOV of the MIRI's imager on the 15.02.2020 at 12:00:00 UTC for the albedo of 0.06 (top) and 0.2 (bottom). The estimated temperature of this asteroid for the albedo of 0.2 is 198.3 K and for the albedo of 0.06 is 201 K. The exposure time is 427.35 seconds. The black part (structure) of the image is the coronagraphy, as can be seen in Figure 4.4.

Figure 6.6 shows the only FOV with two detected asteroids, even though one is not technically in the field of view of the imager, just in the field of view of the whole MIRI instrument. In this case, each asteroid is at a different side of the image. It can be seen that the one on the left is leaving the FOV. The signal to noise ratio for the left and the right asteroid is 325.2 $\pm$ 11% and 1419.77 $\pm$ 11% respectively. The asteroid on the right has a much higher signal to noise ratio, as would be expected from the higher temperature. It can also be seen that this asteroid is much brighter than the asteroids on the other shown simulated images. This asteroid also has the highest H of all the shown simulated asteroids.

Figure 6.7 shows the difference in the detectability for the same asteroid at the same time, but with a different value for albedo. The top is the albedo of 0.06 and the bottom is the albedo of 0.2. From the calculations for the temperature and size of an asteroid, it is clear that a lower albedo leads to higher temperature and size. This means that the asteroid with lower albedo should have a higher brightness in the infrared spectrum (as it is bigger and warmer). It is clear from Figure 6.7 that that is the case, as is for other asteroids as shown in Figure 6.8. The signal to noise ratio estimated for the asteroid with an albedo of 0.06 is 805.62 ± 11% and with an albedo of 0.2 is 448.56 ± 11%.

6.4 Discussion of the simulated Images

From these simulated images it has been determined, that 96.9% of the asteroids passing through the FOV of the MIRI's imager are detectable by the just mentioned imager. However, it should be mentioned that to determine whether the asteroid is visible or not, the position within the simulated image was known beforehand. This greatly increased the chance of finding the asteroid. Searching for the asteroid by comparing its signal to the background noise in its neighbourhood leads to better results, than comparing its signal to the background noise of the whole picture. Even though most of the asteroids were bright enough to be seen when compared to the overall image background. Nevertheless, the asteroids can be found by methodically searching smaller parts of the image for distinct signatures.

6.4.1 Estimated Signal to Noise Ratios

The MIRISim [9], as explained in Chapter 4, should not replace the JWST Exposure Time Calculator (ETC), even though it is consistent with the sensitivity model of MIRI. This means that the signal to noise ratios calculated should be reviewed with the ETC. Nevertheless, their high values, as well as their evident presence in the simulated images, speaks for itself. In Figure 6.8, a plot shows the signal to noise ratios calculated for all the asteroids. The lowest value is 64, but most of the asteroids have SN higher than 150, which can be considered a very good (high) signal to noise ratio [52].

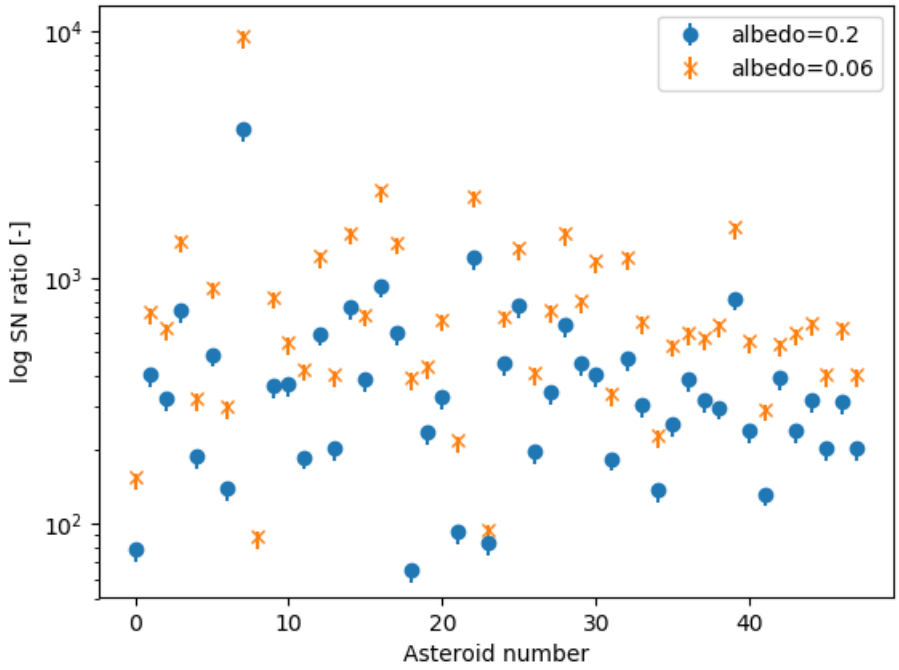

Figure 6.8: Signal to noise ratio (SN) estimations with their respective error bars for infrared observations simulated by MIRISim. The orange crosses are for the asteroids with an albedo of 0.06 and the blue circles are for the asteroids with an albedo of 0.2. They same asteroids are plotted on top of each other. All of the 47 detected asteroids are shown.

Evaluating the Figure 6.8, it can be seen that the ratio of SN for the albedo of 0.06 to SN for the albedo of 0.2 for the same asteroid is on average $SN_{0.06}/SN_{0.2}$ ~2. The one clear outliner is an asteroid with a similar SN for both albedos. This could be due to the fact that in the simulation, this asteroid is leaving the FOV. The ratio of the estimated brightnesses for the albedo of 0.06 and 0.2 for the same asteroid, i.e. same H, has been found to be on average approximately 3.6. This could be written in an equation form, such as for an asteroid with the same absolute magnitude, the fluxes for different albedos are related as:

$$\frac{Flux_{0.06}}{Flux_{0.2}} \sim \frac{0.2}{0.06} + 0.3 \tag{6.1}$$

The SN is proportional to the flux, however, the simulator takes into account some noise terms, which are neglected in these ratios and therefore, the ratios are not the same.

6.4.2 The preferred Filter

Even though the choice of the filter for the MIRI's imager is specified in the proposed observations, the preferred filter is suggested according to the properties of asteroids. As shown in Chapter 3, the brightness of asteroids peaks after 10 microns and increases until 20 microns or more, as can be seen in Figure 3.4. Therefore, the filter should be able to detect at wavelengths longer than 10 microns. When looking at Figure 4.5, it is visible that at wavelengths longer than 20 microns, the proton to electron conversion efficiency starts to decrease, as well as the detection limit in Table 4.1. This would leave five possible filters. These filters are used in the simulations and the results are shown in Table 6.3. It can be seen that filter F1280W has the highest signal to noise ratio estimates for all the asteroids in this table, which would make it the preferred choice.

Table 6.3: Comparison of MIRI's imager's five filters. Each filter is used for five asteroids, shown in the previous Figures, and their signal to noise ratios are compared. The properties of the asteroids are as follows: two asteroids have albedo of 0.06, three of 0.2, with varied exposure times and absolute magnitudes.

	F1000W	**F1130W**	**F1280W**	**F1500W**	**F1800W**
Asteroid name	*SN ± 15%*	*SN ± 18%*	*SN ± 11%*	*SN ± 8%*	*SN ± 18%*
2008 UN310	1585.1	1250.7	2115.9	1949.9	1479.9
2004 TC367	209.5	123.7	253.5	207.1	74.1
2014 QR309	184.3	113.7	260.5	227.6	101.4
2009 FK26	196.4	112.5	238.9	188.3	73.4
2009 SW261	373.9	263.6	539.1	530.6	387.7

6.5 Validation of the Results

Even though a verification of the whole tool has been done, it is still important to review whether the results of this simulation are realistic. This is done by inspecting the consistency of the results w.r.t the input data.

Possible errors, which have been considered:

- The position of the asteroid in the simulated image.
- The length of the asteroid streak.
- The agreement in the length of the asteroid streak for low w.r.t dark albedo.
- The brightness of different asteroids compared to each other.
- The exposure time, e.g. number of frames and integrations.
- The filter.

For determining the accuracy of the results, the FITS files and their headers have been analysed and a satisfactory result has been found. The results have been deemed consistent with the inputs.

The validation is also done by comparing the sensitivity of the imager given in Table 4.1 to the SN estimated from the output of the simulation tool. This is shown in Table 6.4. The SN ratio is proportional

to the flux of the asteroid and it increases with the square root of total time [52]. The SN can be calculated as:

$$SN_{calculated} = \frac{F}{Det_l} SN_{det} \frac{\sqrt{t_{new}}}{\sqrt{t_{det}}} \tag{6.2}$$

where F is the flux at the filter wavelength, Det_l is taken from Table 4.1 and its the point source detection limit at the chosen filter (F1280W), the SN_{det} is the SN of the point source detection limit and t_{new} and t_{det} is the exposure time of the simulation and of the point source detection limit in Table 4.1 respectively.

It can be seen from Table 6.4, that the calculated values for SN are much higher than that of the estimated ones. This is due to the fact that some noise terms are present in the simulation, e.g. dark current, but are not taken into account in Equation 6.2. Also the values in Table 4.1 are estimated using the low background setting, therefore lower noise, but the images are simulated using high background noise. Another reason is that asteroids are not point sources, but moving objects. Therefore the SN for moving asteroids is lower than for point sources, as the signal spreads over more pixels. All the SN estimated from the simulated images are lower than the calculated ones, which is as expected. Also, the slower moving asteroids should match the calculated SN more closely. Determining the ratios of calculated SN/estimated SN, it is clear that the longer the streak of the asteroid during the exposure, the bigger the ratio. However, this is not consistent for different albedo values, as the SN ratio for different albedos from the simulator is 2, but the ratio of SN for different albedo values in the calculation is 3.6, as expected from the flux. This is as discussed in Figure 6.8, due to the noise terms neglected in the calculation.

Table 6.4: Comparison of the SN estimated from the simulated images and SN calculated using the sensitivity of MIRI, Equation 6.2. The calculated values are much higher than that of the estimated ones. This is due to the some noise terms, which are neglected in the calculation, but present in the simulation and the fact that the asteroids are not point sources, but moving objects.

Name or designation	**Streak length [arcsec]**	**SN ± 11% [-]**	**Calculated SN [-]**	**Calculated SN/SN [-]**
2008 UN310	0.27	1602.75	3951.91	2.47
2004 TC367	5.96	218.43	1360.43	6.23
2014 QR309	4.79	203.20	978.85	4.82
2009 FK26	18.90	238.9	2508.03	10.50
2006 TF32	8.79	325.2	2666.97	8.20
2001 UY107	10.44	1419.77	20498.84	14.44
2009 SW261	1.97	805.62	4279.28	5.31
2009 SW261	1.97	448.591	1183.79	2.64

7. Conclusion and Recommendations

The purpose of this thesis was to determine whether the use of Mid-Infrared Instrument's (MIRI) imager on board of James Webb Space Telescope (JWST), scheduled to launch in 2021, for the serendipitous observation of asteroids and their characterization would be feasible. The knowledge about asteroids and their characteristics, such as their orbital elements, their size or their albedo, is limited and their estimates can have an error up to 100%. The possibility of decreasing the inaccuracy in these estimates is the main purpose of this research, as knowing more about asteroids can be useful for mankind. Additional knowledge about asteroids can bring more insight about the Solar System, its beginnings, the Earth and also the life on the Earth, as asteroids collided with the Earth since the beginning and shaped the globe and the biosphere. The distribution of asteroids in space could provide more information about the protosolar nebula, such as the pressures or chemistry. Asteroids also pose a threat to the life on the Earth. The collision of an asteroid with the Earth could be deadly and therefore, should be avoided. Therefore, more knowledge about asteroids, such as knowing their albedo, the composition of the asteroids can be estimated, which could help to hinder such a catastrophe. As knowing the composition can help to decide if launching a rocket into an asteroid would indeed help, or just bring a shower of smaller rocks down on the Earth. A mission trying to find out more about this has been launched by NASA [54], to go and reach asteroid Bennu and bring a sample back. Asteroids are also assumed to be full of minerals and other valuable materials, which could bring many mining possibilities or potential for future missions into the deeper space.

Detecting the asteroids at the infrared wavelengths by Mid-Infrared Instrument's imager (MIRI) can help to estimate the size and the albedo of the asteroids with an error of 35% in extreme cases and 10% on average. Therefore, this thesis tries to determine if and to what extent can MIRI shed more light on asteroids. This is done by creating a simulation tool, which can mimic the functioning of the MIRI's imager, with a help of other already existing tools, such as APT (proposal tool, from where the proposal GTO 1282 is chosen), MIRISim (software simulating the capabilities of MIRI) and Serendipitous asteroid tool (python tool, which determines the position of asteroids w.r.t the instrument and their characteristics). A realistic case study is then presented, where proposed observations for MIRI's future are used to obtain the answer to the thesis question. These proposals are used as typical observations for MIRI and their specifications are used in the simulations. This is done by inputting these data into the Serendipitous asteroid tool, which will determine whether there are any asteroids in the field of view, and if so, their characteristics, such as absolute magnitude. The output of this tool is then used in MIRISim to simulate the asteroids as would be seen by the imager. This is then evaluated by estimating the signal to noise ratio of the asteroids to determine their 'visibility'. Running the tool for 1153 different specified observation inputs resulted in 47 observations with at least one asteroid in the field of view (FOV) of the imager. This is a 4.1% success rate. From these 47 observations, only one had 2 asteroids in the FOV, which means 48 known asteroids to be detected. Each of these asteroids has been simulated twice, once for an albedo of 0.2 and once for an albedo of 0.06. The result is 93 visible out of 96 expected asteroids, which means a 96.9% success. One of the asteroids, which is not visible for neither the albedo of 0.2 and neither 0.6, has an absolute magnitude of 24.8, which is the faintest of all the simulated cases with an estimated diameter of 30-60 m. The other asteroid is visible for the albedo of 0.06, but can not be detected for the albedo of 0.2. However, this asteroid, with H of 20.2 and estimated diameter of 250-500 m, is just leaving the FOV, and this could have made its detectability harder, as the sensitivity on the border of the FOV can be lower. Overall the signal to noise ratio for most of the detected asteroids is quite high, over 150, with the lowest value of 64.

Therefore, the conclusion of this thesis is that the asteroid characterization through serendipitous detection by the Mid-Infrared Instrument's imager on the James Webb Space Telescope is feasible and worthwhile. Even though the rate of asteroids in the FOV is not very high (4.1%), as the asteroids are sparse within the waste space of the Solar System, once the asteroid is there, its detection is almost always successful. In a typical MIRI observation, exposure time of 488.4 s, the filter of F1280W, the imager can detect asteroids with a size bigger than 250 m in diameter, when r (Sun-asteroid distance) and d (asteroid-instrument distance) are less than 3 AU. It has been estimated that for a 5-year mission

life, 183 314 currently known asteroids could be detected, assuming the imager is working 25% time during the science hours. Assuming that the instrument can detect asteroids bigger than 250 m, 916 570 asteroids could be detected for "free", due to the simultaneous use of MRS and imager, by MIRIM during its lifetime, from which 733 256 are yet unknown asteroids. Meaning that the use of the imager will not cost anything while the MRS is running for another user. The sensitivity of MIRIM is higher than other infrared missions (WISE detects asteroids with D $>$ 6 km [4]) and therefore observing asteroids with MIRIM could enable detection of many smaller asteroids (D $>$ 250 m), as well as the estimation of their sizes and henceforth albedos.

To be able to use the MIRI's imager for asteroid characterizations, some future actions are recommended to the users of the telescope. These recommendations follow from the conclusions and are suggested on the best-effort basis.

1. It is important that the data from the imager are being downloaded and made available, even though the observer has requested the use of the MRS only. A tool, which can automatically search for asteroids in these data should be developed.

2. If possible, the user is suggested to use the filter F1280W, as this filter shows the most promising results.

3. The JWST Data Reduction Pipeline needs to be adjusted to make sure that the asteroid signatures do not get overwritten by a correcting algorithm, as this would lead to losing the infrared data about asteroids. The adjustment should change the algorithm, which removes the cosmic ray hits and asteroids so that it checks if the significant change in the pixel values could be due to an asteroid, and if so, it does not remove it. This could be done by evaluating the close pixels at different frames to the pixel, which has a significantly higher value. This could lead to finding a number of significantly higher pixel values creating a streak over the period of the whole integration time.

Bibliography

[1] E. Howel, "Nasa's james webb space telescope: Hubble's cosmic successor," July 2017, visited on: October 2018. [Online]. Available: https://www.space.com/21925-james-webb-space-telescope-jwst.html

[2] JPL and NASA, "The probability of collisions with earth," September 2018, visited on: October 2018. [Online]. Available: https://www2.jpl.nasa.gov/sl9/back2.html

[3] A. Cellino, V. Zappalà, and P. Farinella, "The size distribution of main-belt asteroids from iras data," *Monthly Notices of the Royal Astronomical Society*, vol. 253, no. 4, pp. 561–574, 1991. [Online]. Available: http://dx.doi.org/10.1093/mnras/253.4.561

[4] J. R. Masiero, A. K. Mainzer, T. Grav, J. M. Bauer, R. M. Cutri, and et.al., "Main belt asteroids with wise/neowise. i. preliminary albedos and diameters," *The Astrophysical Journal*, vol. 741, pp. 68–88, November 2011.

[5] L. Husarova, "Serendipitous asteroid observation," February 2018, visited on: August 2018. [Online]. Available: https://github.com/lenkaaaa49/Serendipitous-asteroid-observation/releases

[6] NASA, "Jpl small-body database search engine," September 2017, visited on: September 2017. [Online]. Available: https://ssd.jpl.nasa.gov/sbdb_query.cgi

[7] JPL Solar System Dynamics Group, "Asteroid & comet field-of-view search request," February 2018, visited on: February 2018. [Online]. Available: https://ssd.jpl.nasa.gov/x/ispy.html

[8] Pamela Klaassen, "Mirisim," April 2018, visited on: April 2018. [Online]. Available: http://miri.ster.kuleuven.be/bin/view/Public/MIRISim_Public#Installation_Instructions

[9] *MIRISim Documentation Release 1.0.0*, 1st ed., MIRI European Consortium, March 2018, http://miri.ster.kuleuven.be/bin/view/Public/MIRISim_Public#User_Guide.

[10] Wikipedia, "Asteroid," October 2017, visited on: September 2017. [Online]. Available: https://en.wikipedia.org/wiki/Asteroid

[11] E. F. Tedesco, "Asteroid," August 2017, encyclopaedia Britannica, Inc., Visited on: September 2017. [Online]. Available: https://www.britannica.com/topic/asteroid

[12] Space Telescope Science Institute, "Mid-infrared instrument (miri)," August 2017, visited on: Ocotber 2017. [Online]. Available: https://jwst.stsci.edu/instrumentation/miri

[13] ——, "Jwst data reduction pipeline," August 2018, visited on: October 2018. [Online]. Available: https://jwst-docs.stsci.edu/display/JSP/JWST+GTO+Observation+Specifications

[14] 8planets.co.uk, "Facts about asteroid belts," 2016, visited on: September 2017. [Online]. Available: http://www.8planets.co.uk/facts-about-asteroid-belts

[15] W. R. Johnston, "Asteroid albedos: graphs of data," March 2017, visited on: September 2017. [Online]. Available: http://www.johnstonsarchive.net/astro/astalbedo.html

[16] M. Delbo, G. Libourel, J. Wilkerson, N. Murdoch, P. Michel, and K. Ramesh, "Thermal fatigue as the origin of regolith on small asteroids," *Nature*, vol. 508, pp. 233–236, April 2014.

[17] M. L. Nelson, D. T. Britt, and L. A. Lebofsky, *Review of asteroid compositions.* The University of Arizona Press, 1993, pp. 493–522. [Online]. Available: http://adsabs.harvard.edu/abs/1993rnes.book..493N

[18] Wikipedia, "Electromagnetic spectrum," September 2017, visited on: September 2017. [Online]. Available: https://en.wikipedia.org/wiki/Electromagnetic_spectrum\#/media/File:EM_Spectrum_Properties_edit.svg

[19] R. A. Rohde, "Solar spectrum," August 2016, visited on: October 2018. [Online]. Available: https://commons.wikimedia.org/wiki/File:Solar_Spectrum.png

[20] R. Dymock, "The h and g magnitude system for asteroids," *Journal of the British Astronomical Association*, vol. 117, no. 6, pp. 342–343, 2007. [Online]. Available: https://www.britastro.org/asteroids/dymock4.pdf

[21] T. Greicius and NASA, "How to tell the size of an asteroid," September 2011, visited on: September 2017. [Online]. Available: https://www.nasa.gov/mission_pages/WISE/multimedia/gallery/neowise/pia14733.html

[22] NASA and Space Telescope Science Institute, "The incredible expanding telescope," May 2016, visited on: September 2017. [Online]. Available: http://webbtelescope.org/article/Technology_at_the_Extremes/9

[23] NASA, "James webb space telescope," September 2017, visited on: September 2017. [Online]. Available: https://jwst.nasa.gov/orbit.html

[24] Space Telescope Science Institute, "Jwst astronomers proposal tool overview," November 2017, visited on: March 2018. [Online]. Available: https://jwst-docs.stsci.edu/display/JPP/JWST+Astronomers+Proposal+Tool+Overview

[25] ESA, "Russia asteroid impact: Esa update and assessment," February 2013, visited on: September 2017. [Online]. Available: http://www.esa.int/Our_Activities/Operations/Space_Situational_Awareness/Russia_asteroid_impact_ESA_update_and_assessment_-_continuation

[26] NASA, "Asteroid fast facts," March 2014, visited on: September 2017. [Online]. Available: https://www.nasa.gov/mission_pages/asteroids/overview/fastfacts.html

[27] J. J. Lissauer and I. de Pater, *Fundamental Planetary Science*. 32 Avenue of the Americas, New York, NY 10013-2473,USA: Cambridge University Press, 2013.

[28] L. Husarova, "The use of james webb space telescope's mid-infrared instrument for observation and characterization of asteroids," Delft University of Technology, TU Delft University, Netherlands, Literature Study, October 2017.

[29] P. Wolf and NASA, "The outer planets," August 2007, visited on: September 2017. [Online]. Available: http://lasp.colorado.edu/education/outerplanets/spacejunk_asteroids.php

[30] D. R. Davis, D. D. Durda, F. Marzari, A. Bagatin, and R. Gil-Hutton, *Asteroids III*. University of Arizona Press, 2002, ch. Collisional Evolution of Small-Body Populations, pp. 545–558, 2002aste.book..169B.

[31] L. Pullen, "Strange asteroid shapes explained," July 2008, visited on: September 2017. [Online]. Available: https://www.space.com/5587-strange-asteroid-shapes-explained.html

[32] D. B. Henry, "The temperature of an asteroid," *Annales de l'I.H.P. Physique théorique*, vol. 55, pp. 719–750, 1991.

[33] D. J. Tholen, *Asteroid Taxonomic Classifications*, 1st ed., ser. Space Science Series. Tucson, AZ: The University of Arizona Press, February 1989, pp. 1139–1150, 1989aste.conf.1139T.

[34] S. J. Bus, F. Vilas, and M. A. Barucci, *Asteroids III*. University of Arizona Press, 2002, ch. Visible-Wavelength Spectroscopy of Asteroids, pp. 169–182, 2002aste.book..169B.

[35] M. Mueller, M. Delbo, J. L. Hora, D. E. Trilling, and et.al, "Exploreneos. iii. physical characterization of 65 potential spacecraft target asteroids," *The Astronomical Journal*, vol. 141, p. 9pp, April 2011.

[36] Encyclopedia Britannica, "Star," January 2018, visited on: March 2018. [Online]. Available: https://www.britannica.com/science/star-astronomy#ref510299

[37] A. W. Harris and J. S. V. Lagerros, *Asteroids III*. University of Arizona Press, January 2002, ch. Asteroids in the Thermal Infrared, pp. 205–218. [Online]. Available: https://www.lpi.usra.edu/books/AsteroidsIII/pdf/3005.pdf

[38] J. Norwood, H. Hammel, S. Milam, J. Stansberry, J. Lunine, N. Chanover, D. Hines, G. Sonneborn, M. Tiscareno, M. Brown, and P. Ferruit, "Solar system observations with the james webb space telescope," *Publications of the Astronomical Society of the Pacific*, vol. 128, no. 960, p. 025004, February 2016. [Online]. Available: http://stacks.iop.org/1538-3873/128/i=960/a=025004

[39] M. Muller, "Surface properties of asteroids from mid-infrared observations and thermophysical modeling," diploma thesis, Freie Universitat Berlin, July 2007.

[40] D. Allen, "The Method of Determining Infrared Diameters," *NASA Special Publication*, vol. 267, p. 41, 1971.

[41] A. W.Harris, "A thermal model for near-earth asteroids," *Icarus*, vol. 131, no. 2, pp. 291–301, 1998.

[42] D. T. HAAR, "Chapter i - the black body radiation law," in *The Old Quantum Theory*, ser. The Commonwealth and International Library: Selected Readings in Physics, D. T. HAAR, Ed. Pergamon, 1967, pp. 3 – 14. [Online]. Available: http://www.sciencedirect.com/science/article/pii/B978008012102450005X

[43] J. Gardner, J. Mather, M. Clampin, and et al., "The james webb space telescope," *Space Science Reviews*, vol. 123, pp. 458–606, April 2006.

[44] Space Telescope Science Institute, "James webb space telescope design," September 2017, visited on: October 2017. [Online]. Available: http://www.stsci.edu/jwst/overview/design/

[45] B. J. Rauscher, O. Fox, P. Ferruit, R. J. Hill, A. Waczynski, Y. Wen, W. Xia-Serafino, B. Mott, and et al., "Detectors for the james webb space telescope near-infrared spectrograph. i. readout mode, noise model, and calibration considerations," *Publications of the Astronomical Society of the Pacific*, vol. 119, no. 857, p. 768, 2007. [Online]. Available: http://stacks.iop.org/1538-3873/119/i=857/a=768

[46] G. S. Wright, D. Wright, G. B. Goodson, G. H. Rieke, G. Aitink-Kroes, J. Amiaux, A. Aricha-Yanguas, R. Azzollini, K. Banks, and et. al, "The mid-infrared instrument for the james webb space telescope , ii: Design and build," *Publications of the Astronomical Society of the Pacific*, vol. 127, no. 953, p. 595, 2015. [Online]. Available: http://stacks.iop.org/1538-3873/127/i=953/a=595

[47] P. Bouchet, M. García-Marín, P.-O. Lagage, J. Amiaux, J.-L. Auguéres, E. Bauwens, and et. al, "The mid-infrared instrument for the james webb space telescope , iii: Mirim, the miri imager," *Publications of the Astronomical Society of the Pacific*, vol. 127, no. 953, p. 612, 2015. [Online]. Available: http://stacks.iop.org/1538-3873/127/i=953/a=612

[48] Space Telescope Science Institute, "Jwst gto observation specifications," July 2017, visited on: October 2018. [Online]. Available: https://jwst-docs.stsci.edu/display/JDAT/JWST+Data+Reduction+Pipeline

[49] K. M. Pontoppidan, T. E. Pickering, V. G. Laidler, K. Gilbert, C. D. Sontag, C. Slocum, M. J. Sienkiewicz, C. Hanley, N. M. Earl, L. Pueyo, S. Ravindranath, D. M. Karakla, M. Robberto, A. Noriega-Crespo, and E. A. Barker, "Pandeia: a multi-mission exposure time calculator for JWST and WFIRST," in *Observatory Operations: Strategies, Processes, and Systems VI*, vol. 9910, Jul. 2016, p. 991016.

[50] A. Glasse, G. H. Rieke, E. Bauwens, M. Garcıa-Marın, M. E. Ressler, S. Rost, T. V. Tikkanen, B. Vandenbussche, and G. Wright, "The mid-infrared instrument for the james webb space telescope, ix: Predicted sensitivity," *Publications of the Astronomical Society of the Pacific*, vol. 127, August 2015.

[51] W.H.Press, S.A.Teukolsky, W.T.Vetterling, and B.P.Flannery, *Numerical recipes in C, Second edition*. Cambridge University Press, 1992, ch. Modeling of Data. [Online]. Available: http://apps.nrbook.com/c/index.html

[52] O.Hainaut, "Signal, noise and detection," Jun 2015, visited on: October 2018. [Online]. Available: http://www.eso.org/~ohainaut/ccd/sn.html

[53] N. Reid, J. Lee, J. Lotz, J. Kalirai, and R. Osten, "Jwst science policies," TU Delft University, January 2015, presentation slides. [Online]. Available: https://jwst.stsci.edu/files/live/sites/jwst/files/home/events/_documents/NeillReidAASJan2015.pdf

[54] NASA, "Osiris-rex asteroid sample return mission," August 2018, visited on: October 2018. [Online]. Available: https://www.asteroidmission.org/mission/

Appendix A - Serendipitous asteroid detection tool

Serendipitous asteroid detection tool is a tool developed in Python to determine which asteroids are in the field of view (FOV) of the specified instrument at the specified time. A short explanation of this tool is given here, but more details can be found in [5]. This tool has not been developed during this thesis.

The tool has 4 functions:

1. Creates new tables - runs the code for a new FOV, time and instrument
2. Updates tables older than a specified date - runs the code for outdated data
3. Creates new tables and updates all the old tables - runs the code for a new FOV, time and instrument and updates all the outdated data
4. Creates new tables and updates tables older than a specified date - runs the code for a new FOV, time and instrument and updates the outdated data

The workflow of this tool is pretty straightforward. The user starts by selecting the desired function from the 4 options. Then the tool opens an input table, which consists of data about the observation; FOV, observation date and time, instrument and mode. Using these data, the tool determines the known asteroids in the FOV at that time with the help of Asteroid & Comet Field-of-View Search (ISPY) [7]. This identifies the known comets or asteroids that are present in the instrument's field of view. This tool is interested in asteroids and therefore all the asteroids found in the FOV are saved in a table together with their physical characteristics, such as their position in the sky (RA, DEC), as known from JPL HORIZONS System [6]. In the end, the brightness of the asteroid, as would be seen by the instrument, is estimated adding the thermal brightness, calculated by the NEATM model at different wavelengths, and the reflected brightness. This is also saved in the table. A flowchart of this workflow is shown in Figure A.1.

To be able to run the tool, one has to have both Python and MySQL installed. The tables, where all the data are stored, are created in a MySQL database.

The JPL Horizons database [6] consists of data for solar system objects (781736 asteroids, 3535 comets, 190 planetary satellites, 8 planets, the Sun, L1, L2, select spacecraft, and system barycenters) It is provided by the Solar System Dynamics Group of the Jet Propulsion Laboratory and it can be used to generate ephemerides for solar-system bodies. There are three ways to interact with the system, by telnet, email or web-interface and for the purpose of this code, the web interface is used.

Asteroid & Comet Field-of-View Search [7], so-called ISPY, is a program which can identify the known asteroids or comets that are present in an instrument's field of view. This program can be accessed through a web interface or an email. For the purpose of this code, the former, web-interface, is used. The program is based on a high-precision n-body numerical integration, which also includes the perturbations of the planets, and some smaller bodies (Moon, Ceres, Pallas and Vesta). For comet propagations, non-gravitational models are also included. The ISPY program can take from 1 to 20 or more minutes to display the result, depending on the number of objects in the field of view and system load.

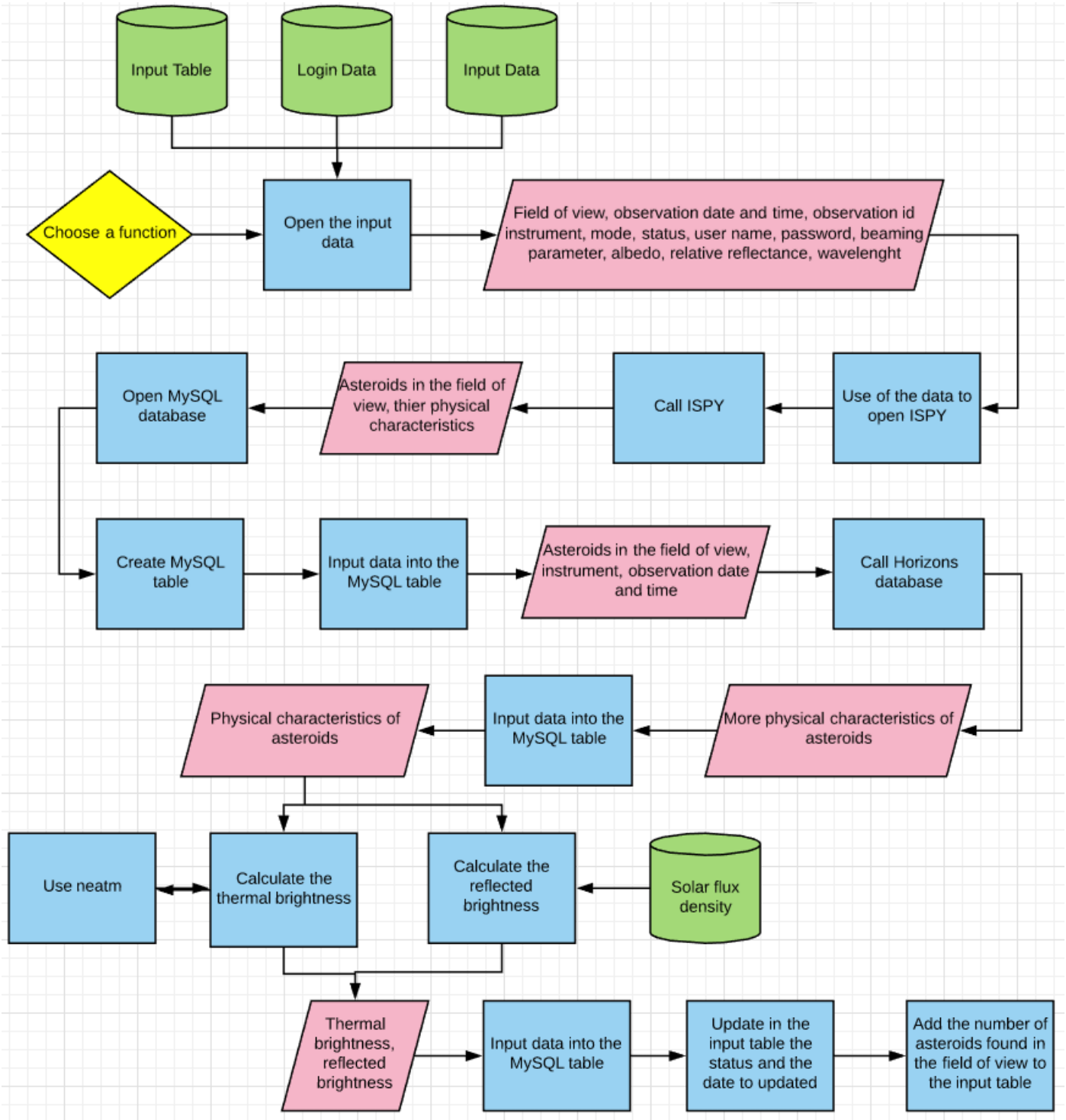

Figure A.1: Flowchart of the Serendipitous asteroid detection tool. The green cylinders are the input data/files, the blue rectangles are the steps-functions and the pink boxes are the data which go from one function to another. [5]